University of Washington
Department of Civil and Environmental Engineering

1861

MODELING OF OROGRAPHIC PRECIPITATION WITH MULTILEVEL COUPLING OF LAND-ATMOSPHERIC INTERACTIONS

Ana P. Barros

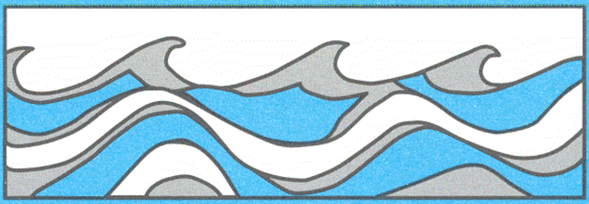

Water Resources Series
Technical Report No.139
August 1993

Seattle, Washington
98195

Department of Civil Engineering
University of Washington
Seattle, Washington 98195

MODELING OF OROGRAPHIC PRECIPITATION WITH MULTILEVEL COUPLING OF LAND-ATMOSPHERIC INTERACTIONS

Ana P. Barros

Water Resources Series
Technical Report No. 139

August 1993

ABSTRACT

A three dimensional model that simulates regional distributions of orographic precipitation was developed. The model consists of two parts: (1) an independent circulation module designed to interpolate synoptic wind fields from the macroscale (100s of kms) to the mesoscale (10s of kms); (2) a Lagrangian transport module to track adiabatically the evolution of moist air masses and the generation of precipitation across the study domain. Total water and moist static energy are treated as conservative tracers but for the scavenging effect of precipitation. The removal of precipitable water from the atmosphere is governed by a spatially varying precipitation efficiency parameter that requires calibration. A new evaporative cooling scheme to account for phase and mass exchanges during the downfall of hydrometeors was also developed. The model was applied to the Olympic and the Sierra Nevada Mountains.

In addition, a new methodology to facilitate adaptive multilevel coupling for the simulation of land-atmosphere interactions is illustrated through three distinct modeling experiments. A first experiment consisted of coupling two simple circulation models solving each separately for the potential and rotational components of atmospheric wind fields. The resulting wind fields improved greatly the ability of the precipitation model to reproduce leewind storms in the Olympic Mountains. In the second experiment, three versions of the precipitation model operating at resolutions of 40, 60 and 80 km were intermittently coupled to establish the path of independent storms across the Sierra Nevada region. Detailed spatial distributions of precipitation at low computational costs were obtained by solving advective transport at the coarser spatial resolution and restricting precipitation processes to the finest resolution. Finally, a third experiment consisted of linking the 40 km implementation of the precipitation model for the Sierra Nevada to a 1D surface energy model to simulate directly runoff, soil moisture and snow cover distributions, and the recycling of moisture between the atmosphere and the land-surface. The two models were coupled by a 2D finite-element mesh with a 10 km grid-spacing. This case-study provides insight into the intra-annual dynamics of the hydrological cycle in mountainous regions, which is impossible to observe directly.

The report concludes by discussing and recommending potential directions for other research in the context of mountain hydrology. The necessity for studies addressing issues related to climate, landscape evolution and water resources management is stressed.

ACKNOWLEDGMENTS

The research described in this report is based on the doctoral dissertation of the author. Thanks are due to my advisor, Dennis Lettenmaier, for recruiting me to the University of Washington, for his guidance in the pursuit of my goals, and for providing an ever challenging, yet supportive, work environment. I wish to thank Stephen Burges for his many words of wisdom during many relished talks on the purpose of science, engineering and hydrology, for his good will to provide me with the means to ease the load of my first teaching appointment, and for his invaluable help and support throughout my research. I wish to thank Professor Conway Leovy (Department of Atmospheric Sciences, University of Washington) for having been generous with his time, for attending to last minute requests, and for his inquisitive comments and pertinent suggestions. I wish to thank Professor John M. Wallace (Department of Atmospheric Sciences, University of Washington) for his patience and support during my attempts to learn the basics of atmospheric dynamics. I wish to thank past and present colleagues in Room 159 Wilcox Hall for so many cherished memories. I wish to thank my parents for always being present when I needed them most, my husband for being my source of serenity and strength. For the last eleven months of this research, my daughter and I have been the closest of companions. Together, we shared late nights, nerve-wrecking program bugs, and the satisfaction of accomplished goals. The promise of her was my joy. Because of her, the future has arrived unexpectedly early.

This research was supported by the National Aeronautics and Space Administration through a Graduate Fellowship in Global Change Research to the author, and through grant NAGW-2556, by Pacific Northwest Laboratory under contract DE-AC06-76RLO 1830 with the U.S. Department of Energy, and by the Junta Nacional de Investigacao Cientifica e Tecnologica of Portugal.

TABLE OF CONTENTS

LIST OF FIGURES

LIST OF TABLES

CHAPTER I - INTRODUCTION

"Somehow the wondrous promise of the earth is that there are things beautiful in it, things wondrous and alluring, and by virtue of your trade you want to understand them."

Mitchell Feigenbaum, cited by Gleick (1988)

1.0 Foreword

Human civilizations depend on the continuous exchange of moisture and energy between the earth and its atmosphere, which determines the genesis of weather patterns, and ultimately the climate. Precipitation, a key element of the exchange of water between the land-surface and the atmosphere (the hydrological cycle), is the focus of this research.

The space-time distribution of global precipitation varies over a wide range of temporal and spatial scales, and encompasses a variety of phenomena ranging from ice ages to flash floods. The dynamic interaction between the general circulation of the atmosphere and the earth's surface is the principal cause of global precipitation variability. Anomalies in the mean global distribution of precipitation occur at a variety of frequencies among which the most important are the interdecadal, the interannual, and the intra-annual (monthly and seasonal) frequencies. These can be traced directly to ocean-atmosphere and land-atmosphere interactions, respectively for the cases of frequencies above and below the annual cycle. The linkages of weather anomalies over great distances, also known as teleconnections, result from ocean-atmosphere interactions which are restricted to the upper ocean layer in the case of the interannual variability, and extend to the deeper ocean layers for larger time scales (Hsu and Wallace 1976, Horel and Wallace 1981, Folland and Owen 1988, Ebbesmayer et al. 1989, Lau and Sheu 1988, Glantz 1991). The influence of regional biogeomorphology (e.g. soils and vegetation diversity) upon the annual cycle and the monthly and seasonal distributions of precipitation is well known (Manabe and Terpstra 1974, Lettau et al. 1979, Shukla and Mintz 1982, Lovelock 1985).

Traditionally, hydrologic research has focused on "too much, or too little, or undesirable amounts of water" (Burges 1986). In general, hydrology has been a specialized field within Civil Engineering, Forestry, or Geology. Although the case for a discipline, in its own right, of hydrological sciences has attained widespread recognition only recently (Dooge 1986, Eagleson 1986 and 1991, Shuttleworth 1991a and 1991b, Wood 1991), precipitation has always been a major research concern from the point of view of engineering hydrology. Examples include rare storm and flood forecasting, design of dams, bridges, and highways, reservoir operation, irrigation, and drought management. For the most part, engineering-oriented investigations of precipitation have been carried out independently, and without much interaction among hydrologists and atmospheric scientists. This fragmentation is at least partly the result of partitioning the hydrological cycle into individual processes, which are conceptualized as operating in separate environments at distinct temporal and spatial scales. Hydrologists thus have limited their investigations to the land surface, and meteorologists and forecasters have concentrated on the atmosphere alone. This partitioning is aggravated by the use of distinct scientific methodologies by each discipline: engineers tend to rely on statistics, empiricism and conceptual modeling, while weather forecasters combine data assimilation and numerical prediction techniques, and other meteorologists remained close to fundamental experimentation (Namias 1980, Dooge 1986, Eagleson 1986).

In recent years, the intensification of the collection and analysis of atmospheric data worldwide has allowed the characterization of the variability of precipitation fields caused by ocean-atmosphere interactions (Lau and Sheu 1991). This has been possible because of the uniformity and extent of the oceans, conditions which impose fewer restrictions on sampling frequencies than when similar data analysis is conducted over land. Across the continents, difficult access to remote regions and ubiquitous heterogeneities in the arrangement of land-surface elements such as soils, vegetation types, and orography combine to make measurement and description of the variability of precipitation and associated land-atmosphere interactions much more difficult.

With the development of general circulation models (GCMs) has come the need for a holistic treatment of the hydrologic cycle. Modeling experiments have revealed the magnitude and persistence of the influence of land-atmosphere interactions upon regional climatology (Delworth and Manabe 1989, Shuttleworth 1991a and 1991b, Wood 1991). This finding was especially far-reaching for surface hydrology as it lead to the general acknowledgement of the importance of multiscale dependence between large-scale and regional climate, and regional climate and field-scale hydrology.

A major problem in the implementation of complex representations of land-atmosphere interactions in climate models is the computational constraints under which GCMs operate. As hydrologic and biogeophysical models have been integrated within GCMs, they have been forced to operate at scales much above their range of applicability. In most instances, however, the real problem stems from poor understanding of the fundamental physical processes. This is particularly important in the case of land-atmosphere interactions, as the refinement of the resolution of GCMs offers no guarantee of significantly improving current skills to describe the spatial and temporal modes of interaction among hydroclimatological variables from the macroscale to the catchment scale (Beven 1989, O'Loughlin 1990, Shuttleworth 1991b).

1.1 Motivation

By conducting an intercomparison study involving the GISS (Goddard Institute for Space Studies), NCAR-CCM (National Center for Atmospheric Research - Community Climate Model), GFDL (Geophysics Fluid Dynamics Laboratory) and OSU (Oregon State University) models, Grotch (1988) showed that current GCMs produce large discrepancies in simulations of the spatial and temporal distribution of precipitation fields (see Fig. 1.1). The disparities found are critical in the sense that they do not reflect intensity nuances, but rather contradictory diagnostics: one model may depict very dry summers in Texas, while another model will describe exactly the opposite climatology. The argument that such critical disparities are at least rooted partially in the parameterization scheme used to incorporate moist convection in GCMs is accepted (Cunnington and Mitchell 1990). This reasoning is convincing in the tropical and subtropical regions because of the close mutual dependency between the large circulation and the latent heat release associated with cloud formation and precipitation. Away from the tropics, the similarity among model simulations increases, while fundamental differences between present-day climate and modeled scenarios remain. These differences correspond generally to the spatial variability of precipitation intensity and correlate well with biases found in the response of synoptic and large-scale components of circulation to terrain forcing. These include the magnitude of the orographic enhancement of precipitation upwind mountain barriers, and the amplification of subsidence in the lee slopes under the influence of large amplitude stationary waves (Broccoli and Manabe 1992). Also, processes such as convective storms and inland-breeze phenomena, which develop at spatial frequencies below the range of resolution of GCMs, are not taken into consideration.

The implications of GCMs' lack of ability to portray the variability of precipitation extend to the entire planetary boundary layer, as water availability at the land surface governs the latent and sensible heat fluxes that in turn constitute lower boundary conditions to such models. The importance of this issue has been documented by Deardorff (1978), Ookouchi et al. (1984), Mahfouf et al. (1987), Avissar and Pielke (1989) and Wood (1991) with respect to soil moisture effects, and the work by Bell (1978), Broccoli and Manabe (1992), Browning (1980), and Gollvick (1984), among others, with respect to orographic precipitation. In addition, the effects of local recycling of moisture on regional climatologies have been investigated by Broccoli and Manabe (1992), Charney (1975), Lettau et al. (1979), Lovelock (1985), Salati and Vose (1984), Sellers and Lockwood (1981), and Xue et al. (1990).

From such an extensive body of research stems the common view of a global environmental system resulting from the coupling of biogeophysical processes in the oceans, on the land surface, and in the atmosphere, and hence the motivation for the World Climate Research Program (WCRP). Components of WCRP are projects such as EOS (Earth Observing System) and GEWEX (Global Energy and Water Cycle Experiment), among others. One of the most visible objectives of these projects is to develop observation techniques, and to implement systems to handle and assimilate both remotely sensed (EOS) and land-based observing systems (GEWEX). Other equally ambitious goals have been set for these programs, which focus on developing models to improve the current understanding of large and small-scale water and energy budgets, and to improve the predictability of weather, hydrology and climate over the continents.

Among the issues central to WCRP, the following, summarized from the Scientific Plan for GEWEX (1992) are of particular interest to the scope of this dissertation: (a) How do water and energy budgets vary in space and time on a continental scale? What are the key controlling factors and how do they vary with topography? (b) How important is the spatial and temporal variability of soil moisture? What is the impact of that variability upon the dynamics of persistent hydrologic anomalies and short-term climate? (c) What role does snow cover play in modulating the temporal availability of water and the spatial variability of albedo? What is the nature of the lag relationship between seasonal snowcover and regional hydrology?

1.2 Hydroclimatology of Mountainous Areas

Mountain hydrology remains a challenge with regard to validation, calibration, prediction, and interpretation of regional and global climate (Shuttleworth 1991b, Klemes 1990). This is well known from GCM results, inasmuch as some of the largest disparities between model results and observations are consistently found in the neighborhood of the Andes, the Himalayas, and the Rockies (Delworth and Manabe 1989).

Precipitation at high elevations contributes disproportionately to the surface hydrological cycle of many areas of the globe in which there is significant topographic variability. About 70 percent of the annual runoff in the Western U.S. is derived from snowmelt from relatively small (less than 25 percent of total land area) headwater catchments (Barros and Lettenmaier 1993a, Kalinin 1971). Further evidence of the role of high-elevation precipitation upon streamflow regimes can be found in the work of Cayan and Peterson (1989), who were able to explain the dependence of the delay between the annual peaks of streamflow and precipitation over the North and Central Pacific regions by relating the observed phase lag to basin elevation and snowpack depth. This effect extends far beyond the mountainous regions and persists for long periods of time, as shown by Ebbesmeyer et al. (1989) who were able to connect the decadal variability of density current patterns in Puget Sound to the hydrology of the Cascade Mountains.

In mountainous areas and at high elevations, where local topography governs the triggering of cloud formation and the enhancement of processes such as condensation, raindrop or ice nucleation, and growth, the water cycle is controlled by the duration and distribution of precipitation. Intense, lengthy precipitation events are typical upwind of the ridge, while the magnitude and duration of precipitation events decreases sharply on the lee side (Sumner 1988, Cotton and Anthes 1989).

Aspect and slope variations related to topographic complexity strongly affect the surface energy balance, as they impose regional heterogeneities upon the distribution of radiative forcing. This is illustrated by Fig. 1.2, which shows how the direct-beam solar radiation varies with slope angle and aspect at latitude 45°N at the times of the equinoxes. Also, as a result of thermal gradients in the landscape, breeze circulations independent of synoptic and large-scale features develop between the valley and neighbor mountain crests (Oke 1978, Pielke 1984).

The geophysical landscape is not a passive recipient in the hydrological cycle, but rather an active component whose feedbacks affect the water budget at the land surface in a variety of ways (Dickinson et al. 1986, Salati and Vose 1984, Sellers and Lockwood 1981, Lovelock 1986). Table 1.1 summarizes results from model simulations of the hydrological balance at the land surface, given four different scenarios of vegetative cover, and using climatological data from a catchment in the United Kingdom (Sellers and Lockwood 1981). The results illustrate the influence of vegetation cover on the partitioning of precipitation among runoff, evaporation and transpiration. Evapotranspiration accounts for 71 percent of the annual precipitation in the case of the pine forest, while that value is reduced to 40 percent in the case of a wheat field. Although these results are specific to the catchment studied, the example demonstrates the effect of vegetation cover upon runoff yields, and hence streamflow patterns (Bosch and Hewlett 1982).

Most of the studies of the dependence of climate on land-atmosphere interactions have concentrated on subtropical and equatorial environments, such as the Amazon river basin and the African deserts. The justification is that analysis of satellite and field data, as well as model results, suggests the weakening of land-atmosphere interactions at higher latitudes. However, Broccoli and Manabe (1992), who have analyzed two GCM simulations of long-term precipitation distributions obtained for a flat representation of the continents in one case (NM), and for a realistic distribution of orography in the second case (M), found this not to be the case for orographic effects. The results of their study substantiate both the importance of the interaction between large-scale circulation and mountains in establishing midlatitude dry climates (Fig. 1.3a), and the effective contribution of soil moisture feedback to precipitation especially during late spring and summer (Fig. 1.3b). The acquisition of field data in the amount and quality required to extend similar studies at spatial scales relevant to regional hydrology is prohibitive economically. Development of numerical models at spatial scales adequate to resolve major topographic features offers an alternative for investigation of land-atmosphere interactions at high and midlatitudes.

1.3 Research Scope and Objectives

The scope of this dissertation is restricted to the study of the sub-grid scale variability of regional distributions of orographically induced precipitation in temperate latitudes, and the investigation of the fingerprints of land-atmosphere interactions in the spatial and temporal evolution of precipitation fields. The impact of orography upon the production of precipitation is examined first, and the dynamics of the feedbacks inherent to moisture recycling in mountainous regions [10^4- 10^6 km^2] are explored subsequently.

The specific objectives of this research are to: 1) develop a three-dimensional model that simulates regional distributions of orographic precipitation, 2) develop a methodology to facilitate multiscale coupling of hydrologic and atmospheric models, and 3) to validate the models proposed and to explore the dynamics of the hydrological cycle in mountainous regions. Chapters II, III, IV, and V of this dissertation provide a thorough account of the descriptive, analytical, and quantitative components of the work completed to fulfill these objectives.

1.4 Thesis Structure

An inventory of the fundamental concepts and state-of-the-art techniques in orographic precipitation modeling is presented in Chapter II. This Chapter is also the core of a paper to appear in *Reviews of Geophysics* (Barros and Lettenmaier 1993d). Chapter III introduces the new orographic precipitation model, and provides discussion of the results for an application to the Olympic Mountains. The contents of the Chapter has been printed in *Monthly Weather Review* (Barros and Lettenmaier 1993a). A new evaporative cooling scheme to account for phase and mass exchanges during the downfall of precipitation is described in Chapter IV. The scheme was developed for direct implementation in the orographic precipitation model, and was tested for a case-study in the Sierra Nevada Mountains. The application was reported in a paper submitted to *Monthly Weather Review* (Barros and Lettenmaier 1993e).

Chapter V introduces the mathematical basis of adaptive multilevel methods and advances arguments in support of the use of such methods to couple models operating at a variety of spatial scales. Parts of Sections 5.1, 5.2, and 5.3 and the entire contents of Section 5.4 compose a separate paper to be published by the International Association of Hydrological Sciences (Barros and Lettenmaier 1993b). Section 5.5 constitutes the major portion of a manuscript for submission to the *Journal of Climate.* This Section describes two experiments conducted for the Sierra Nevada Mountains, where the orographic precipitation model was applied independently on a three-level grid, and subsequently coupled dynamically to a surface energy model. The first experiment was designed to investigate the characteristics and computational costs of solutions obtained through the implementation of adaptive multilevel formulations as compared to those obtained through independent standard simulations. The second experiment was aimed at gaining insight into the intra-annual dynamics of the hydrological cycle in the region, by focusing on the effect of evaporation and transpiration fluxes upon the distribution of atmospheric moisture and the initiation and magnitude of precipitation events.

The dissertation concludes in Chapter VI by providing a summary of the work reported here and pointing to the most pertinent conclusions. Recommendations for further work focus on the need for better discretization and calibration techniques. Further validation of adaptive multilevel methodologies for multiscale coupled hydrologic-atmospheric modeling studies in conjunction with companion field experiments is particularly emphasized.

Table 1.1 Annual totals of simulated runoff, interception and transpiration for four vegetation types (in mm of rainfall equivalent).
(After Sellers and Lockwood 1981)

Vegetation	Runoff	Interception	Transpiration
Wheat	417	158	134
Pine	152	253	309
Oak	279	172	263
Grass	318	62	335

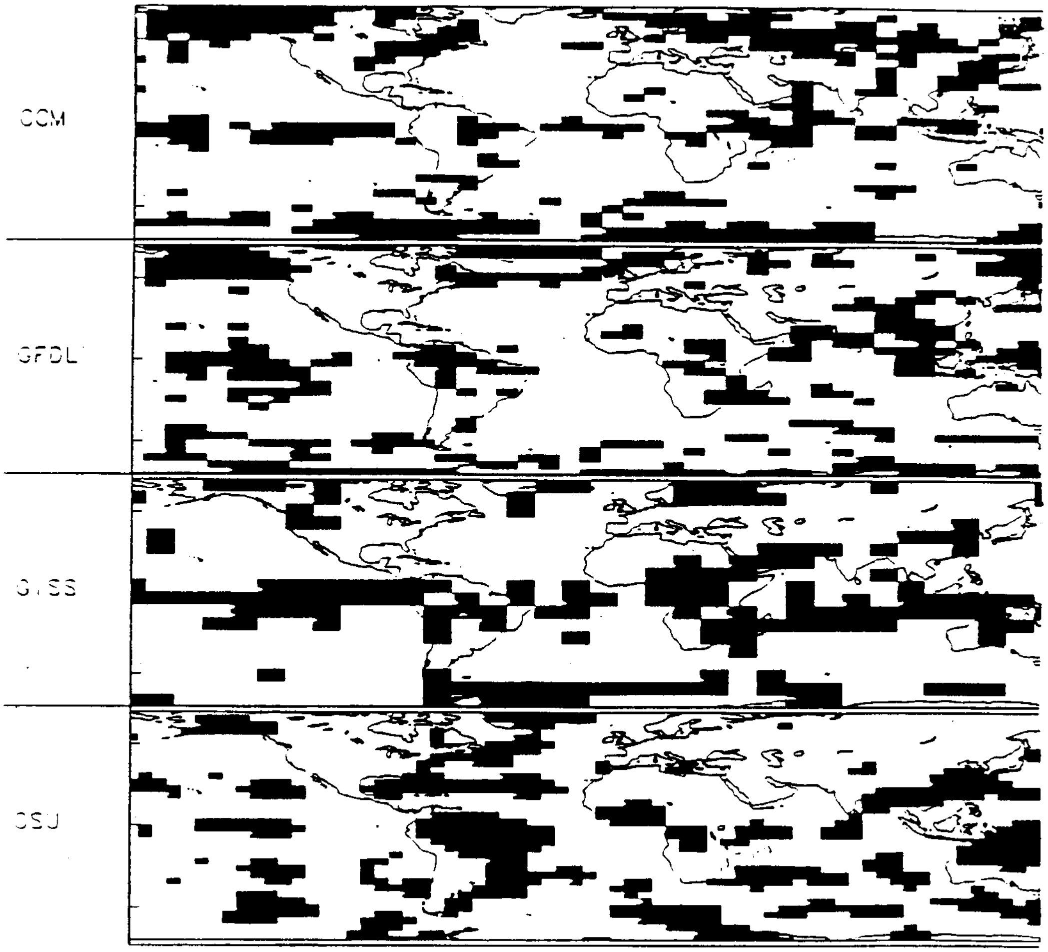

Figure 1.1 Locations of GCM grid points showing a maximum 25% absolute change in annually averaged precipitation (mm/day) predicted by four GCM models (CCM, GFDL, GISS, OSU) for a double CO_2 scenario. (After Grotch 1988)

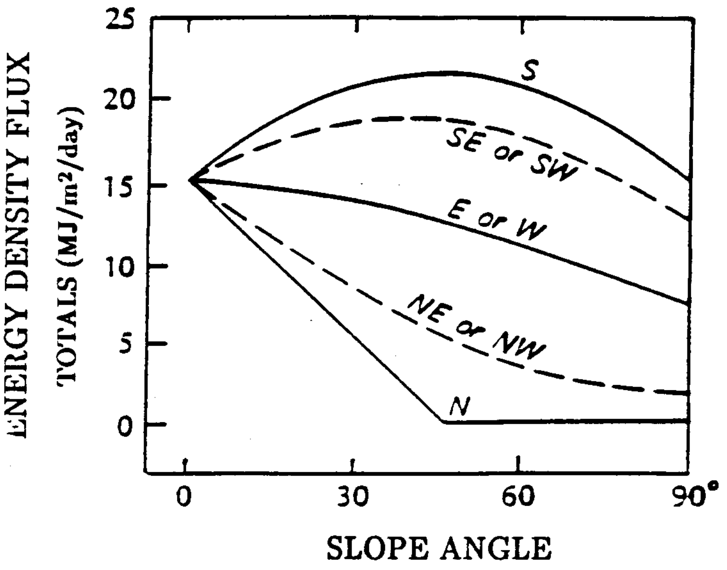

Figure 1.2 Monteith's diagram of total daily direct-beam solar radiation (S), expressed in MJ/m^2/day, incident upon slopes of differing angle and aspect at latitude 45°N at the times of the equinoxes.
(After Oke 1978)

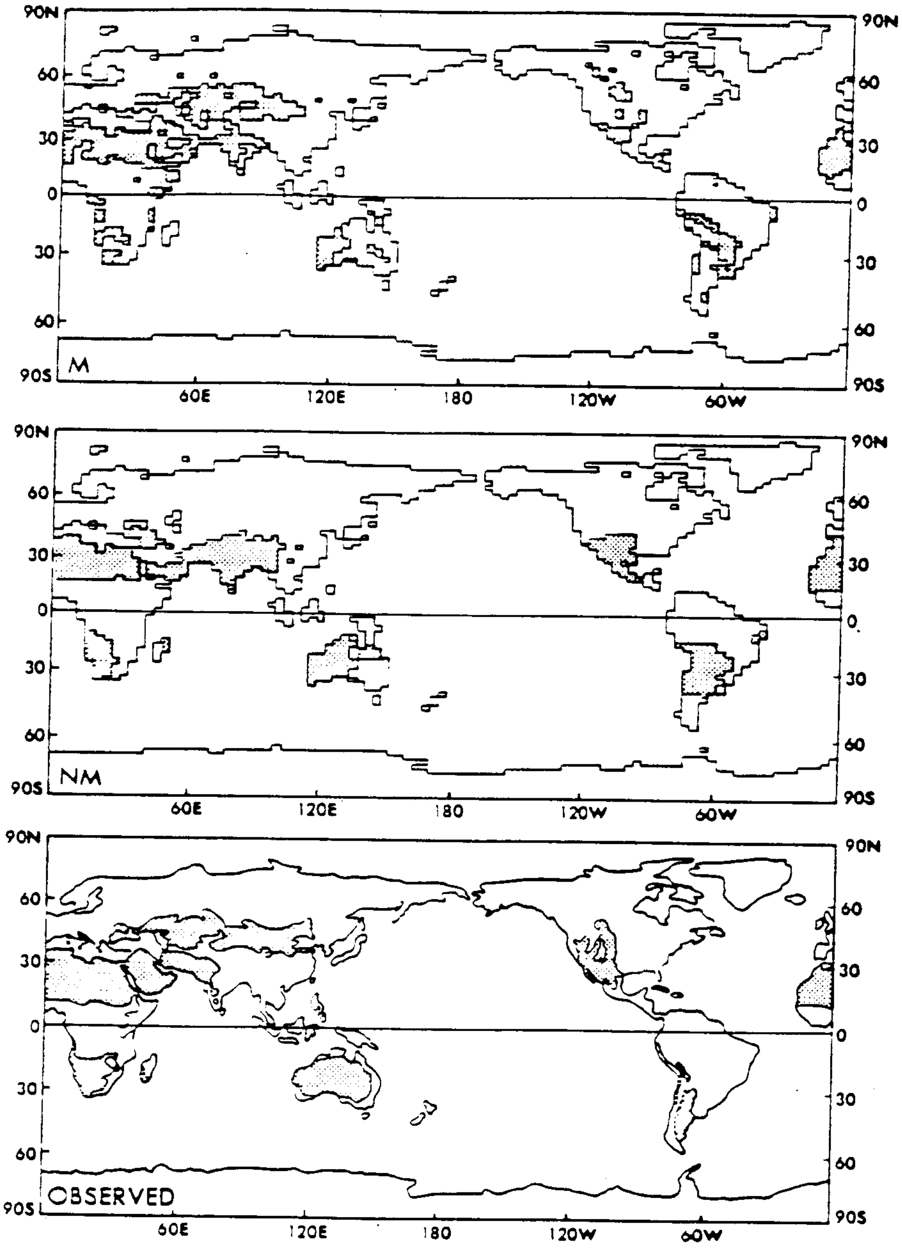

Figure 1.3 a) Global distribution of arid and semi-arid climates (shaded): M - GCM simulation with realistic orography; NM - GCM simulation without mountains (flat earth);
Observed - Kopën classification.

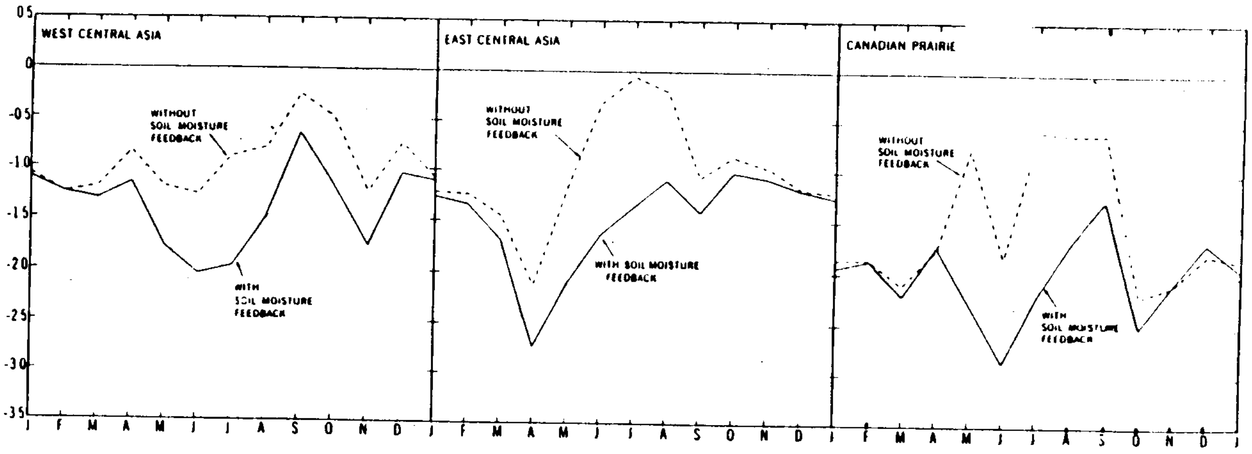

Figure 1.3 b) Seasonal variations of the differences in monthly precipitation between the M and NM GCM simulations, with and without soil moisture feedback. (After Broccoli and Manabe 1992).

CHAPTER II - OROGRAPHIC PRECIPITATION: CONCEPTS AND MODELING

"Under the same sky in which the stars pursue their orbits, as symbols of the unchangeable fullness of Nature, we see the clouds towering, the rain pouring, and the winds changing, as symbols - as it were - of just the opposite extreme, the most capricious of all processes in Nature, impossible to bring inside the fence of its Laws."

H. von Helmholtz 1875, cited by Bergeron (1960a)

2.1 Introduction

Mountains are a complex source of perturbations and deformation of atmospheric flows, the signature of which is detected over a wide range of time-space frequencies extending from the scale of boundary layer motions up to that of planetary waves (Namias 1960, Smith 1979, Kasahara 1980, Wallace 1987). The influence of orography on the long-term spatial distribution of precipitation is readily observable in mountainous areas. For instance, Figs. 2.1a and 2.1b show the distribution of annual precipitation along east-west transects at the Canadian/U.S. border, and through the Coast Range and Sierra Nevada Mountains of California. Differences in mean annual precipitation of several hundred percent between windward and lee side locations are not unusual. Orography explains many spatial features of the global and regional distributions of precipitation, as well as the hydrologic cycles of the atmosphere and land surface. Nonetheless, although the scientific understanding of cloud and precipitation processes has improved substantially since Helmholtz's time, modeling and prediction of orographic precipitation remain elusive (Roads and Maisel 1991, Dunn 1991, Namias 1980).

The influence of topography on precipitation can be attributed primarily to localized disturbances of the state of equilibrium of the vertical structure of the atmosphere. Such disturbances result from orographic formations acting either as obstacles, elevated heat sources and sinks, or concentrated areas of high roughness (Bergeron 1960a, Smith 1979, Banta 1990). In addition to destabilization of the atmosphere's vertical structure, air flow over a topographic barrier leads to the ascent of water-rich, relatively warm air from low elevations. The forced ascent of moist air enhances condensation, the formation and growth of clouds, and ultimately the triggering and duration of precipitation events at high elevations, especially along the windward slopes of topographic barriers.

The concept of an air parcel [an infinitesimal, thermally insulated control volume at the environmental pressure] can be used to illustrate the series of events which lead to the formation of orographic clouds. Figure 2.2a shows schematically how an unsaturated air parcel embedded in the flow field ascends adiabatically in the upwind vicinity of a mountain barrier [SU] until it reaches the cloud base level [UCB]. Above this altitude, the air parcel becomes saturated, and condensation is activated, creating a new cloud or enlarging a pre-existing one [UCB - CT - LCB]. Part of the condensed water is removed by precipitation, mainly in the region which spans from the cloud base [UCB] to the mountain top [H]. As the air parcel moves downward along the lee slopes, it remains saturated until it reaches the lee side cloud base level [LCB]; subsequently, it becomes unsaturated again and its descent proceeds adiabatically (Wallace and Hobbs 1977, Sumner 1988).

Condensation is initiated when an air parcel can no longer hold water in the vapor phase [that is, the parcel's water vapor pressure reaches its saturation value or, in other words, a rising parcel reaches its lifting condensation level LCL]. As a parcel moves up in the atmosphere, the pressure p decreases and the volume expands. Simultaneously, the temperature T and the saturation vapor pressure decrease, due to the verification of the principle of conservation of energy and the proportionality between p and T for an ideal gas. The gradient of temperature per unit height is the lapse rate, Γ_a. Figure 2.2b provides an interpretation of the thermodynamics of forced orographic ascent: a moist parcel moving upward cools and expands at a rate determined by the lapse rate Γ_a until it reaches the LCL. Above this height [UCB], the air parcel is saturated, and thermodynamic changes take place at the saturated adiabatic lapse rate Γ_s [$\Gamma_s = \Gamma_a\ (1+\ \epsilon)$, where ϵ is the ratio of the heat released due to condensation to the corresponding change in internal energy, in a hydrostatic atmosphere and under pseudoadiabatic conditions (Wallace and Hobbs 1977)]. When the air parcel crosses the mountain's crest and descends, the processes are reversed in the absence of precipitation.

Two important differences between the thermodynamics of an air parcel on the windward and lee side of the mountain should be noted: (1) the lifting condensation level is lower on the upwind side of the mountain because the air parcel still retains all its original moisture content, while it has lost water to precipitation when it descends along the lee slopes; (2) this water loss is also responsible for the relative warming of the parcel with respect to its undisturbed upwind temperature. Typically, the net result is the development of a precipitation divide upwind of the orographic divide, which separates the humid upwind slopes from arid ones on the lee side of the ridge (Figs. 2.1a and 2.1b). This is commonly referred to as the rainshadow effect. Wintertime floods of disastrous magnitude have been linked to the interaction between synoptic processes (e.g. cyclones) and lee-wave systems, which lead to strong atmospheric instabilities (Bergeron 1960a, Speranza 1987). However, although short-term enhancement of lee side precipitation does occur due to thunderstorms, precipitating lee wave clouds, or leeward drift of snow and rain, such phenomena rarely obscure the predominance of stable upwind orographic cloud systems on long-term precipitation distributions.

This Chapter is intended to provide an account of the development, and current status of orographic precipitation modeling. Statistical modeling has been instrumental in many aspects of data processing and evaluation of the distribution of precipitation in mountainous areas [Sumner 1988]. Nonetheless, we will focus our attention on the formulation and application of physically-based models aimed at the simulation of atmospheric circulation and cloud dynamics, and their effect on the spatial distribution of precipitation in mountainous areas. We first review briefly the physical processes that control orographic precipitation. We then focus on predictive modeling, including model formulation and parameterization, solution strategies, and validation and calibration. We conclude with an evaluation of the performance of existing models, and a discussion on current trends for further research.

2.2. Descriptive Physics

2.2.1 Dynamics of Atmospheric Flows and the Formation of Orographic Cloud Systems

At the time-scales of atmospheric processes, mountains can be viewed as permanent formations of the landscape. The interaction between mountains and the atmosphere continuously affects local convergence, flow strength, static stability, and atmospheric humidity patterns. The nature of this interaction depends on the relative position of the topographic barrier with respect to the location and characteristics of incoming weather systems. For instance, orographic effects on the spatial structure of rainfall in cold front systems over Northern Italy were investigated by Corradini and Melone (1989), who found the increase of precipitation magnitude with height to vary strongly for pre- and post-frontal storms. Their work suggested orographic enhancement of the order of 50 percent for pre-frontal storms to 150 percent for post-frontal storms. These data corroborate the findings of Parsons and Hobbs (1983), who tracked rainbands as they traveled from the Pacific Coast across western Washington State. They observed that large amounts of precipitation originated in inland areas from post-frontal rainbands, which were either initiated, or enhanced by orography.

Synoptic systems such as fronts and cyclones are characterized by highly convergent low level wind fields, and therefore strong updrafts. Thermally driven mesoscale circulations created by mountain-valley radiative heating differentials enhance convergence locally, and have been linked to the diurnal variability of precipitation (Matveev 1984, Cotton and Anthes 1989). For example, by examining 25 years of data climatological records for the Salt Lake Valley, Utah, and surrounding mountains, Astling (1984) found that the timing of wind convergence and the occurrences of significant precipitation events were related closely. This phenomenon is more important during summer months [strong weather systems, which sweep the continents during winter, dissipate weak diurnal local circulations], and in the tropical regions [convective activity becomes more effective due to very high humidity values]. At scales beyond the area of influence of a given orographic system, the interaction between mountain circulation regimes developed along the slopes of complex, longitudinally extended topographic barriers and large-scale circulations has been linked to the growth of mesoscale convective systems. An example is the intense nocturnal rainfall east of the Rocky Mountains in the central U.S. during summer (Tripoli and Cotton, 1989).

Many of the characteristics of the response of atmospheric circulation to orographic barriers are determined by the strength of the incident synoptic flows. In this context, the major issue is which one of the two possible scenarios will actually evolve: blocking and forcing the flow around a mountain [Fig. 2.3a], or lifting and subsequently spilling of the flow over the leeward slopes [Figs. 2.3b and 2.3c]. The Froude number F_r is an indicator of the tendency of the airflow to go over or around a surface obstacle [$F_r = \frac{U}{\sqrt{Nh}}$, where U is the wind speed, $N = \frac{gT}{(\Gamma_d - \Gamma_e)}$ is the Brunt-Väisälä frequency, g is the acceleration of gravity, T is temperature, Γ_e is the environmental lapse rate, and h is the height of the mountain]. Large F_r values result from strong winds and low static stability; low F_r values result from weak winds and high static stability. Through numerical experimentation, Smolarckiewicz and Rotunno (1989 and 1990) have shown that for $F_r \geq 1$ most of the flow will go over a topographic obstruction, for smaller F_r airflow around the obstruction will be favored. In the latter case, longitudinal flow [barrier wind] is established along the upwind slopes when ridges are significantly longer than wider, and particularly when their length exceeds the Rossby characteristic length $R_o = Nh/f$, where f is the Coriolis parameter (PierreHumbert and Wyman 1986).

Blocking phenomena, which are associated generally with low wind speeds and high atmospheric stability, strongly affect atmospheric dynamics in the vicinity of prominent mountain ranges, especially in the tropical regions. This scenario may become more complex due to differential advection [when upper cold air jets travel faster than lower blocked warm jets], hence creating conditions for embedded convection to occur [cool air on top of warm air] (Smith

1982). However, blocking does not appear to influence long-term precipitation distributions in a significant way. Numerical experiments have been performed using the European Center for Medium Range Weather Forecasts [ECMWF] model for different representations of the world's topography, the simulations of which can be thought of as surrogates for a range of blocking conditions. The results showed essentially no differences in the meridional and zonal distributions of precipitation with the exception of quite modest increases in the tropics and at mid-latitudes when blocking was considered (Jarraud et al. 1987).

Lifting occurs because mountains act as constraints on atmospheric circulation in the lower troposphere, leading to the magnification of the updraft currents, the intensification of transport of moist air from lower, warmer layers to upper, cooler layers, hence triggering and enhancing condensation processes [Figs. 2.2a and 2.2b]. Lifting alone does not initiate the formation of clouds and the occurrence of precipitation: conditions of atmospheric stability must also be considered. Two types of moist atmospheric instability are associated with the formation of orographic clouds: conditional and convective instability.

Conditional, or latent instability refers to atmospheric conditions for which a rising parcel becomes positively buoyant as it reaches and passes its level of free convection [LFC]. Conditionally unstable atmospheric conditions occur when the environmental lapse rate Γ_a is lower than the dry adiabatic lapse rate Γ_d, but higher than the saturated adiabatic lapse rate Γ_s (Wallace and Hobbs 1977).

Convective, or potential instability refers to the lifting of an entire atmospheric layer, as opposed to an individual air parcel. It results from the stratification of the atmospheric column with respect to water vapor contents such that an inversion layer aloft tops moist air underneath (Wallace and Hobbs 1977, Cotton and Anthes 1990, Banta 1990). Forced ascent and atmospheric stability are mutually dependent, and hence the formation of orographic clouds is better understood for conditions in which the updrafts are strong relative to the stability of the atmosphere [that is, conditions under which an air parcel can be driven above its LFC] (Banta 1990).

A weakly stable atmosphere provides conditions for an air parcel to rise above its LFC, either orographically, or by thermally forced ascent [Fig. 2.3c]. In the latter case, transient dynamics inherent to the interaction between orographically and thermally originated gravity waves determine the formation, splitting, and regeneration of unstable clouds [cumulus], and the triggering of thunderstorms (Lin 1986, Cotton and Anthes 1989, Banta 1990). Unstable clouds and thunderstorms are a warm season feature [late spring and summer], during which synoptic conditions are weaker, hence allowing the development of such regional mesoscale circulations as mountain-valley winds and land breezes (Paegal et al. 1990, Pielke 1984).

During fall, winter, and early spring, synoptic motions predominate over local circulations. Under such conditions, stable orographic clouds [stationary upwind midlevel stratus] are formed by condensation of rising air parcels carried by orographic updrafts. A second cloud, whose formation is triggered by thermals which rise from the upwind orographic cloud due to convective activity initiated by the release of latent heat of condensation, may be established aloft and downwind of the primary cloud (Lin 1986). Cloud microphysics are the dominant phenomenon controlling cloud maturing and precipitation occurrence in this case (Banta 1990, Sassen et al. 1992, Rauber 1992).

Strong downward flow, which is characterized by strong advection of horizontal momentum, low pressure, and relatively warm temperatures, is typical in the lee side of mountainous ridges where forced ascent occurs on the windward side (Paegal et al. 1990, Cotton and Anthes 1989, Wallace and Hobbs 1977, Lin 1986). Thermodynamically, the result is to force the dry-adiabatic descent of air parcels in the lee side, and to reduce precipitation drastically. This is the so-called rainshadow effect, which creates a significant discontinuity between the hydrologic and climatic characteristics of the windward and leeward sides of a topographic obstruction [see Fig. 2.1a]. When atmospheric circulation features downwind are characterized by weak winds and relatively strong stability, a train of waves [lee waves] extends from the mountain to the horizon. This is due to the development of upward flow at the lee foot of the orographic ridge where the lee side downward wind reaches a minimum. This pattern is repeated successively in an oscillatory mode until the waves are completely dissipated by friction and/or interaction with large-circulation features (Durran and Klemp 1983). At the ridges of lee waves, clouds form as the result of mechanisms similar to those that contribute to orographic clouds. Upstream depletion of atmospheric moisture may limit the amount of precipitation produced by these clouds. The lack of adequate moisture in the atmosphere can reduce greatly the otherwise strong influence of mountains upon both up- and downwind atmospheric conditions (Robichaud 1988, Corradini and Melone 1989).

2.2.2 Precipitation

As early as the 1940's, the concept of pure orographic precipitation, implied by the forced adiabatic ascent of an air mass encountering a mountainous barrier as shown in Fig. 2.2a, was questioned (Bonacina 1945). The strong observed dependence of precipitation rates on such factors as cyclonic or frontal convergence, mesoscale convergence associated with mountain-valley winds, atmospheric instability and humidity content, suggests that pure orographic rainfall is unlikely to occur (Smith 1987, Astling 1984, Parsons and Hobbs 1983, Storebo 1975, Namias 1960). Sarker (1966) verified that even under the assumption of a fully saturated atmosphere during weak monsoon conditions, precipitation amounts over the Western Ghats in India significantly exceeded the maximum values that could be attributed to pure orographic effects. Hence, it is more correct to refer to the orographic component of precipitation instead of orographic precipitation alone. Nevertheless, the complexity of atmospheric dynamics in the neighborhood of mountains prevents isolation of the orographic component of precipitation from that due to other factors. This is the reason why orographic effects on precipitation distributions are quantified by the absolute increase [orographic enhancement], or decrease [rain-shadowing] of precipitation with elevation.

Topographic obstacles affect precipitation in different ways. In the case of large mountains, the governing mechanism is the forced lifting of incoming air masses well above the lifting condensation level [LCL], hence providing conditions for the formation of deep clouds, which are in turn capable of sustaining continuous precipitation. Small hills, on the other hand, induce only modest lifting. Bergeron (1960a) proposed the feeder-seeder mechanism as a way to explain very high precipitation enhancements induced by small hills. This mechanism consists of the interaction between a non-precipitating stationary cap cloud [feeder] and a precipitating cloud system [seeder] moving with passing fronts or cyclones (Fig. 2.4). Small droplets falling from the higher clouds coalesce with the droplets of the lower cloud, therefore forming bigger drops and maintaining high rainfall rates. In addition, raindrop evaporation is small in this situation, because the atmospheric humidity is near saturation in the areas covered by orographic cap clouds, and because the fall distances between cloud base and the ground are short. A mechanism equivalent to the seeder-feeder mechanism can be established in deep clouds between cloud top [seeder] and cloud base [feeder] (Parsons and Hobbs 1983, Rutledge and Hobbs 1983, Meyers and Cotton 1992).

Storebo (1976) investigated Bergeron's theory by performing numerical experiments with a model which simulated cloud processes from the moment of the activation of cloud condensation nuclei [CCN] up to rain formation, while keeping atmospheric conditions constant. The model was run for flat, smooth, and rough terrain profiles in an attempt to replicate orographic conditions in Western Norway. The results confirmed Bergeron's previous observation that, during the passage of intense rainfall systems aloft, falling raindrops collide with and wash out the low-level orographic clouds topping small hills. This phenomenon was responsible for the increase of precipitation rates up to 10 times, and varied directly with terrain roughness and inversely with wind strength. Bader and Roach (1977) reached the same conclusions for similar experiments aimed at the simulation of nine events of heavy rainfall in South Wales, England.

Gocho (1978) studied the enhancement of rainfall carried by typhoons as they cross the Suzuki Mountains [1210 m elevation] in Japan. This is a region where daily precipitation values can reach 200 to 300 mm. A two-dimensional [2D horizontal-vertical], 2 layer steady state model of airflow based on the assumption of a saturated, neutrally stable atmosphere, was combined with a cloud microphysics model, which included condensation, evaporation and coalescence processes for warm cloud droplets. Computations were performed with and without the existence of an active stratiform cloud located well above the typhoon path. Rainfall rates of the order of those actually measured in the mountains could be approximated only when the seeder-feeder mechanism was activated. Carruthers and Choularton (1983) carried out a similar set of experiments using a model setup in which the atmosphere was divided into three distinct layers of uniform stability, hence allowing the simulation of flow in a stratified fluid. The results obtained also supported the feeder-seeder theory.

Choularton and Perry (1986) combined the potential flow model used by Carruthers and Choularton (1983) with a microphysics model which included the growth of cloud drops by condensation on the one hand, and snowflakes by vapor diffusion and riming [collection of supercooled drops] on the other hand. The model was used to carry out sensitivity studies to investigate the enhancement of snowfall by the seeder-feeder mechanism. From these studies, Choularton and Perry (1986) concluded that this mechanism is much more efficient in the case of snowfall than in the case of rainfall, although quantitative evidence at the ground may be obscured by wind drift effects. Hobbs et al. (1973) investigated the growth of solid precipitation particles in orographic clouds by vapor diffusion, riming and aggregation with other ice particles. They found that, for high enough ice crystal concentrations [e.g. $\geq 100\ l^{-1}$], crystal growth is governed by vapor deposition and by aggregation mechanisms. Because crystals grown this way are less dense than those obtained by riming, the snowfall distribution at the surface is shifted to leeward in the direction of the prevailing winds (Fig. 2.5). This was verified by Rauber (1992) for an experimental case study in the Central Sierra Nevada: strongly rimed particles fell between 25 and 30 km upwind of the crest, while lightly rimed particles fell near or at the mountain crest. The role of ice crystals as seeding agents of orographic precipitation in deep mixed clouds was investigated by Cotton et al. (1986) and Burrows (1992), who reported a strong dependency of high precipitation amounts on the nucleation rate of ice crystals. When this effect was isolated, the dependence of precipitation rates on aggregation or riming rates proved to be weaker.

Orographic cloud systems triggered by high mountains are often characterized by warm bases and cold tops, with cloud depths that may extend for up to 3 or 4 km. (Rutledge and Hobbs 1984, Meyers and Cotton 1992, Rauber 1992). The formation of graupel, which results from the riming of falling ice crystals by supercooled water droplets, has a strong positive influence on the observed maximum amounts of precipitation (Rutledge and Hobbs 1984, Cotton et al. 1986, Burrows 1992). These results were confirmed by Meyers and Cotton (1992), who also found that this effect can be magnified for low graupel densities which lead to an overall larger mass of graupel-snow mixed particles.

Sassen et al. (1990) analyzed data collected by a multiple sensor system consisting of a microwave radiometer, a lidar and a Doppler radar, during a winter mountain storm in Utah. In their study, the authors concluded that low level supercooled [-3°C to -10°C] orographic clouds played an active role on the generation of intense precipitation only when seeded by ice crystals falling from aloft, or when ice splintering occurred during graupel growth.

For wide and tall orographic barriers [more than 40 km wide and with top heights exceeding 1 km], the role of the seeder-feeder mechanism is diminished. Under these conditions, rain development becomes self-contained within the orographic cloud, and the precipitation drift with the prevailing winds becomes a subgrid scale effect (Robichaud and Austin 1988, Gollvik 1984, Browning 1980).

2.3. Model Formulation

Conservation of mass and energy govern atmospheric dynamics, and therefore the development and fate of orographic precipitation systems. In this section, we provide a summary of the relevant descriptive equations, and the assumptions that are used to modify and simplify them. For more detailed discussions, the reader may wish to consult Wallace and Hobbs (1977), Barry (1981), Pielke (1984), Matveev (1984), Rogers and Yau (1988), and Cotton and Anthes (1990).

2.3.1 Fundamental Equations

Five equations describe flow and cloud dynamics: the continuity equation for air, the thermodynamic equation, the state equation, the momentum equation, and the water balance equation. Their specific forms are:

Continuity Equation:

$$-\nabla . \rho_a \overline{V} = \frac{\partial \rho_a}{\partial t} \tag{2.1}$$

where ρ_a is the density of dry air and $\overline{V} =$ (u,v,w) is the three dimensional velocity vector.

Thermodynamic Equation:

$$\frac{\partial \theta}{\partial t} = -\overline{V} . \nabla \theta + S_\theta + \Psi_d \tag{2.2a}$$

where θ is the potential temperature, defined below, S_θ refers to the internal consumption and production of heat in processes such as condensation, evaporation, freezing and melting, and Ψ_d refers to external sources and sinks of diabatic heat (radiative forcing, entrainment).

In a moist atmosphere, the potential temperature can be expressed by

$$\theta = T\ (1 + 0.61\ q_v)\ (\frac{p_r}{p})^{\frac{R_d}{c_p}} \tag{2.2b}$$

where T is the temperature, q_v is the water vapor mixing ratio, p_r is the reference mean sea-level pressure, R_a is the gas constant for dry air, and c_p is the specific heat at constant pressure. When saturation is reached, the equivalent potential temperature θ_e replaces θ in Eq. (2.2a), and

$$\theta_e = \theta \exp\ (\frac{L\ q_s}{c_p T}) \tag{2.2c}$$

where q_s is the water saturation mixing ratio and L is the latent heat of vaporization. Alternatively, in the case when both liquid and ice phases are present, Eq. (2.2c) takes the form

$$\theta_e = \theta \exp \left(\frac{L\, q_l}{c_p T} - \frac{L_i\, q_i}{c_p T} \right) \tag{2.2d}$$

where q_l and q_i are the liquid water and ice mixing ratios, and L_i is the latent heat of sublimation.

State Equation:

$$p = \rho_m R_a T (1+0.61\, q_v) \tag{2.3}$$

where p is total air pressure, ρ_m $[\rho_m = \rho_a + \rho_w]$ is the density of moist air, and ρ_w is the density of water present in vapor, liquid or ice phases.

Momentum Equation:

$$\frac{\partial \overline{V}}{\partial t} = -\overline{V}.\nabla\overline{V} - \frac{1}{\rho} \nabla p - \overline{g} - 2\, \overline{\Omega} \times \overline{V} + \overline{F} \tag{2.4}$$

where $\overline{g}$ is the gravity acceleration vector, $\overline{\Omega}$ is the Coriolis acceleration, and $\overline{F}$ represents friction effects.

Water Balance Equation:

$$\frac{\partial Q_j}{\partial t} = -\, \overline{V}.\nabla Q_j + \nabla\, (D \nabla Q_j) + \Phi_{tv} + S_Q \tag{2.5}$$

where Q_j represents the amount of water in form j [vapor, liquid, ice] per unit mass of air, D is the turbulent diffusion coefficient, Φ_{tv} is the turbulent influx of water vapor by entrainment, and S_Q is the loss of water by precipitation. Q_t, the total water, is the sum of water vapor Q_v, liquid water Q_l, and ice Q_i, where Q_i is the sum of graupel Q_r and snow Q_s:

$$Q = Q_v + Q_l + Q_i \tag{2.6}$$

In active cloud systems, phase changes among Q_v, Q_l and Q_i take place continuously. These changes are carried out by evaporation, sublimation, condensation and melting mechanisms. The time history of hydrometeor concentrations [water droplets in warm clouds, and ice particles in cold clouds] is determined initially by nucleation, and thereafter by growth processes. As discussed earlier, orographic clouds are predominantly of the warm type [no solid phase] in the case of coastal ranges and medium height mountains [h $\leq$ 1.5 km], while they are generally of the mixed type [coexistence of supercooled water drops and ice particles] in the case of tall continental mountains such as the Cascades, Sierra Nevada, or Rocky Mountains. In mixed type clouds, cold and warm microphysical processes compete and interact mutually.

Water drops originate infrequently from random collisions of water molecules [spontaneous nucleation to form an embryonic water droplet]. More frequently, they are formed as the result of direct condensation of water vapor onto the surfaces of CCN [heterogeneous nucleation]. CCN are non-hydrophobic aerosols which act as condensation nuclei when the atmosphere becomes supersaturated. Ice particles originate rarely from homogeneous nucleation, which results from random collisions and subsequent freezing of supercooled water droplets. A much more common mechanism is forced nucleation as supercooled water droplets freeze by the collection of water molecules onto the surface of an ice nucleus dissolved in the droplet solution [heterogeneous nucleation], or present in the environmental air [contact nucleation]. For very cold conditions when the air is supersaturated with respect to ice, direct deposition of water vapor molecules on the surface of aerosols is also possible [deposition nucleation]. Ice multiplication occurs due to the breakup of snowflakes by collision with other snowflakes and falling raindrops, or due to the splintering of an ice particle when thermal stresses become excessive during riming.

The concentration numbers of water droplets and ice particles per unit mass [N_c] are established initially with respect to the concentrations of activated

CCN and ice nuclei [IN]. Their temporal and spatial history is described by

$$\frac{\partial N_c}{\partial t} = -\overline{V} . \nabla N_c + \frac{\partial}{\partial r_d} (N_c G) + B - C \qquad (2.7a)$$

and

$$N_c = N_c (r_d, x, y, z, t) \qquad (2.7b)$$

where r_d is the characteristic size of the hydrometeor concentration, $G = \frac{\partial r_d}{\partial t}$ is the growth rate, B is the multiplication or breakup rate, and C is the loss rate due to aggregation, entrainment, or precipitation scavenging.

Raindrops grow in warm clouds by condensation and by coalescence. In cold clouds, ice particles grow by deposition from the vapor phase, aggregation, and riming. Condensation and deposition into each hydrometeor are directly proportional to the particle's surface area and to the vapor pressure gradient between the particle and its environment. Coalescence and aggregation result from collisions between pairs of hydrometeors in their settling trajectories. For a given control volume, coalescence, aggregation and riming depend on the number and size of hydrometeors, the geometric and kinematic characteristics of the collision, and the chemical activity at the contact surfaces of both particles.

Problems in establishing fundamental equations to describe nucleation and growth processes originate from: 1) the large number of CCN and IN existing in the atmosphere; 2) the difficulty in determining characteristic size and surface area values for the hydrometeor distribution; 3) the impossibility of describing deterministically the randomness of collisions which result from differential settling of large numbers of particles over a wide size range, and; 4) the timing and efficiency of coagulation chemistry leading to effective coalescence and aggregation. Due to the large numbers and randomness of hydrometeor size, surface area, solution chemistry, and other properties, nucleation and growth processes are represented statistically. Empirical coefficients are used to quantify mass-size and fall speed-size relationships, the activation of CCN and IN, and the interactions between the liquid and ice phases. Coalescence and aggregation are described in turn by efficiency coefficients. These parameters are often determined in laboratory experiments, or inferred from field observations forced to fit the conceptual models of choice. In representing the fundamental physics of cloud processes it is necessary to use some empirical parameterizations.

2.3.2 Approximate Equations

Approximations to the fundamental equations can be divided into two groups: the first group consists of those approximations that are used widely in all kinds of atmospheric models, independently of their purpose or operational scale; the second group consists of approximations that are more or less peculiar to models used for the simulation of orographic precipitation. Simplifying assumptions to the continuity and momentum equations belong to the first group; simplifications of the thermodynamic and water balance equations belong to the second group.

In orographic precipitation models, or in mesoscale models used to study orographic precipitation events, the anelastic form of Eq. (2.1) is used frequently, therefore eliminating time-dependence [e.g. sound waves] from the dry air mass conservation requirement. The assumption of incompressibility reduces this equation to the divergence of the velocity vector [$\nabla\overline{V} = 0$], and it implies that the spatial variations of density are negligible. This assumption is more appropriate when vertical displacements occur within shallow atmospheric layers [vertical movements must be limited to layers of depth much smaller than the atmospheric scale height (~ 8 km)].

Approximations to the momentum equation are established with respect to the scales which govern the circulation phenomena to be modeled: the meso-γ scale [1-20 km], the meso-β scale [20-200 km], the meso-α scale [200 - 1000 km], and the synoptic scale [thousands of kms]. Common approximations to the momentum equation include: a) the steady-state assumption between refreshment of boundary conditions [$\partial\overline{V}/\partial t = 0$]; b) the inviscid fluid assumption, which leads to the removal of $\overline{F}$ from Eq. (2.4); c) neglecting Coriolis effects when $R_o \geq 1$ [meso-β and meso-γ scales], and; d) use of the hydrostatic approximation because vertical accelerations generally are much smaller than the vertical pressure gradient force, except when strong convection is present [meso-γ scale], hence reducing the vertical momentum equation to the contribution of potential energy

$$\frac{\partial p}{\partial z} = -\rho\, g \tag{2.8}$$

The most generalized approximation with respect to the thermodynamics of rising air parcels is to neglect radiative or any form of diabatic exchange of heat with the surrounding environment [Ψ_d=0 in Eq.(2.2a)]. The next most generalized approximation, and the most important, results from the assumption of adiabatic expansion or compression, as a parcel moves up and down respectively

$$\frac{d\theta}{dz} = 0 \tag{2.9a}$$

or, for a hydrostatic atmosphere

$$c_p\, dT + g\, dz = 0 \tag{2.9b}$$

However, when condensation is triggered after air parcels become saturated, and water is released subsequently from the air parcel [precipitation], the assumption of adiabatic motion is not valid. To preserve consistency between the actual physical processes and their quantification, this assumption is replaced by the assumption of pseudo-adiabatic motions, which implies the release of all condensed water at the same rate at which it is formed. The difference between saturated adiabatic or pseudo-adiabatic lapse rates is not significant at the atmospheric heights of interest for orographic precipitation. This results from the reduced dependence of saturated humidity with pressure at low temperatures, and that only small amounts of water per unit mass of air are exchanged in these processes.

The exchange of latent heat between liquid and ice phases [e.g. freezing and melting] frequently is neglected in view of the complexity of quantifying such heat fluxes given the myriad of forms and densities of raindrops, ice crystals, snowflakes, and graupel which may coexist in a mixed cloud. If this simplification is introduced, Eq. (2.9b) becomes the equation for the conservation of moist static energy h_M

$$dh_M = c_p\, dT + g\, dz + L\, dq = 0 \tag{2.10}$$

where q is the water vapor content [q=0 for dry adiabatic processes, $q = q_v$ for moist processes].

Diffusive terms can be neglected in the water conservation equation, Eq. (2.5), as they are typically at least one order of magnitude smaller than the other terms in the equation. Entrainment fluxes, when accounted for, are assumed to be forced linearly by temperature and moisture gradients between the air parcel and the surrounding environment. Precipitation fluxes are the subject of extended and diverse parameterization schemes, and are addressed in the next section.

2.3.3 Parameterization Schemes

Parameterization schemes are used to represent complex processes through simplified equations. Their main purpose is to provide accurate estimates of the patterns of interaction between physical mechanisms over the spatial and temporal ranges of interest. Parameterization schemes are aggregation operators, which may be used in one of the following ways:

(a) to lump together the activity of repetitive mechanisms [that is replication of one mechanism a "large-number" of times: for example, cloud drop coalescence];

(b) to lump together distinct mechanisms for which only empirical knowledge is available [e.g. multiplication of hydrometeors by ice splintering or simple breakup], or;

(c) to introduce the effect of subgrid scale processes on the balance equations of the governing scales [e.g. entrainment is a subgrid scale mechanism with respect to mesoscale wind fields].

The representation of source and sink terms in conservation equations such as Eqs. (2.5) and (2.7) is a major parameterization issue.

The first two methodologies (a) and (b) are used in experimentation and sensitivity studies focused on the testing and improvement of models of conceptual physics [M1 models] (Hobbs et al. 1973, Nickerson et al. 1986, Cotton et al. 1986, Burrows 1992). These models can be complex [apart from thermodynamic constants, Rutledge and Hobbs (1984) used 24 empirical coefficients in a diagnostic model of precipitation development in narrow cold-frontal rainbands, while Burrows (1992) used 15 parameters in his study of a Central Sierra Nevada orographic cloud system], and simulations are limited to one event at a time. Examples of the use of empirical coefficients in the parameterization of cloud microphysics are:

o mass-size and fall speed-size laws of the form $F=a\phi^b$, where F is mass or fall velocity, and ϕ is the diameter of the hydrometeor;

o deposition, condensation, evaporation and melting mechanisms described by flux laws of the form $C = B_t(\Delta T)$ or, alternatively, $C = B_q(\Delta Q)$, where B_t and B_q are conversion rates, and (ΔT) and (ΔQ) are the gradients of temperature and water concentration between a growing ice crystal or water droplet and the surrounding environment, respectively;

o coalescence and aggregation expressed as growth equations of the form $G = ME_e\phi^c$, where M is the specific mass of one individual droplet, E_e is an efficiency factor, and ϕ is the hydrometeor diameter;

o precipitation rates computed by integrating the net settling fluxes of raindrops, snowflakes and graupel along their traveling path between cloud base and the ground surface.

The number of parameters in M1 models is directly proportional to the number of types of hydrometeors [water droplets, ice crystals, snowflakes, graupel].

Methodology (c) leads to bulk parameterization [M2 models], in that it attempts to connect directly, or through very few steps, the causative mechanism [orographic lifting] to the ultimate result [precipitation]. In bulk parameterization schemes, a common approach is to define a precipitation efficiency parameter or scavenging rate β, which estimates precipitation rates P from a layer of thickness ΔZ based on a relationship of the form $P=\beta\ Q_l\ \Delta Z$. Combined with adequate boundary conditions, and fine parameter tuning, these models have been shown to perform well (Rhea 1978, Alpert 1986, Gollvik 1984, Peck and Schaake 1990, Oki and Koike 1991, Barros and Lettenmaier 1993a).

In general, models of the M1 type require virtually no calibration, or if any is necessary, it is limited to those parameters for which controlled measurements are not considered adequate. Examples are ice nucleation or aggregation rates, which depend largely on highly variable local and synoptic conditions (Burrows 1992, Meyers and Cotton 1992). Models of the M2 type require calibration. To illustrate this point we compare the parameterization of cloud initiation in the model described by Barros and Lettenmaier (1993a), and in the diagnostic orographic model coupled by Bell (1978) to the weather model of the United Kingdom Meteorological Office. Barros and Lettenmaier (1993a) applied a modification factor, always equal or less than one, to the water vapor mixing ratio at saturation. This modification factor depends on estimated concentrations of CCN and IN and spatial location, and must be calibrated to achieve acceptable phase errors in the timing of precipitation triggering. Bell (1978) instead used a fixed value of 90 percent as the threshold relative humidity for cloud formation.

2.3.4 Simplifying Assumptions in Dynamic Modeling of Orographic Precipitation

Realistic modeling of the dynamics of orographically induced precipitation must include consideration of both cloud microphysics [entrainment, drop and ice crystal formation, growth], and circulation dynamics [wind, temperature, and humidity fields]. The primary consequence of the need to model these processes is that a wide range of time and space scales needs to be considered, which leads inevitably to a conflict between resolution requirements and computer resources. In light of these considerations, most orographic precipitation models make one or more of the following simplifying assumptions: a) flow and thermodynamic variables are specified externally; b) cloud microphysics are parameterized extensively; and c) the ascent of air parcels is assumed to occur adiabatically or pseudo-adiabatically as a result of linear deformation of the synoptic flow field by the local orographic slope.

Wind, temperature, and humidity distributions generally are provided by circulation models (Bell 1978, Gollvik 1984, Giorgi and Bates 1989), or are taken from radiosonde or balloon observations (Collier 1975, Rhea 1978, Nickerson et al. 1986, Barros and Lettenmaier 1993a, Meyers and Cotton 1992). In weather forecasting operations, data from geostationary satellites are used to track the evolution of synoptic systems (Browning 1989).

Analytical or quasi-analytical flow models have been coupled occasionally with cloud models for the numerical representation of well-controlled meteorological episodes (Sarker 1966, Fraser et al. 1973, Gocho 1978, Robichaud and Austin 1988). A frequent simplification in the application of these models has been the use of constant atmospheric saturation values, since the effect of this assumption upon the simulation of isolated rainfall events apparently is negligible (Sarker 1966, Gocho 1978, Carruthers and Perry 1986).

Airflow models based on the assumption of potential (inviscid) flow have been found to perform adequately for the simulation of orographic precipitation events over small hills [width ≤ 20 km and height ≤ 1 km] (Carruthers and Choularton 1983). However, Robichaud and Austin (1988) investigated the effects of variation of the wind curvature with height on precipitation amounts, and found that potential flow theory leads to underprediction of vertical velocities because it neglects mountain wave dynamics. Likewise, Smolarckiewicz and Rotunno (1989 and 1990) stated the need to account for nonlinear viscous effects in the case of low Froude numbers. Nonetheless, the assumption that the regional wind fields are determined by synoptic weather conditions, while local forcing is determined by orography alone allows for the linear addition of large-scale and local divergences, and this assumption has been used with good results in extended simulations (Gollvik 1984, Alpert 1986, Barros and Lettenmaier 1993a).

Among the numerous simplifications reported in the literature, two stand out because of the governing role they may play especially at high elevations [e.g. more then 1-2 km above MSL]: (1) neglecting deep convection upwind of the topographic divide [see Fig. 2.3c], which can induce significant errors of underestimation in the case of slow moving air masses (Robichaud and Austin 1988); and (2) failure to account adequately for cold cloud processes, which may be responsible for large errors both in amount and spatial distribution of post-frontal precipitation during fall and winter, in continental regions (Hobbs et al. 1973, Parsons and Hobbs 1983, Meyers and Cotton 1992).

The computational costs of models that include a complete description of both circulation dynamics and microphysics may be prohibitive for applications lasting more than one, or a few events. A time-step of 50 seconds was used by Hobbs et al. 1973, and Meyers and Cotton (1992) used time-steps equal to 5 and 2.5 seconds in their 2D non-hydrostatic model with solid and liquid phase microphysics. Time-steps of the order of one or two minutes are used routinely in the forecast models of the National Meteorological Center (NMC) and the European Center for Medium Range Weather Forecasts (ECMWF).

Heating and cooling processes inherent to, respectively, condensation and evaporation mechanisms generally are assumed to be negligible for cloud decks with a horizontal extent less than 200 km (Carruthers and Choularton 1983 and 1986). This observation does not extend to mesoscale processes associated with cumulus clouds, whose formation and growth are linked intimately to the release of conditional instability triggered by latent heating and cooling (Cotton and Anthes 1989). Nevertheless, Fraser et al. (1973), who included pseudo-adiabatic latent-heat release in their 2D, steady-state, stably-stratified inviscid flow model, found that atmospheric stability could be lowered significantly for blocking conditions. They also found that the effect of latent heat release was negligible for most atmospheric conditions under which orographic precipitation is produced. Numerical experiments carried out by Lin (1986) indicated the potential importance of this effect in the triggering of convective clouds for stable, or conditionally stable atmospheric conditions.

Cyclogenesis [development and deepening of low pressure centers] on the lee side of mountains may be responsible for higher precipitation amounts than would be predicted by the assumption of linear deformation of incoming flows. This mechanism was ignored in all of the studies reviewed above because of the complexity inherent to the coupling of synoptic and lee-systems dynamics (Speranza 1987).

2.4. Model Implementation

2.4.1 Solution Strategies

Analytical or semi-analytical models are based on steady state formulations of the flow problem [continuity, momentum, and thermodynamic equations], which are simplified and reduced to the wave equation for the vertical displacement ξ of the streamlines:

$$\nabla^2\xi + \mu_c\, \xi = 0 \tag{2.11}$$

where μ_c, the characteristic wave number of the propagation of the perturbations, depends not only on the geometry of the flow domain but also on the atmospheric stability upwind of a mountain's crest (Sarker 1966, Hobbs et al. 1973, Gocho 1978, Robichaud and Austin 1988). In these models, dynamic effects are restricted to the time evolution of microphysical processes such as the growth of raindrops or snowflakes until they reach the ground.

When time-dependence, nonlinearity, and interaction between flow and microphysical variables are retained in a model's formulation, the model must be solved numerically. An overriding concern in the design of numerical solution strategies is that they yield true solutions, or at least solutions which approach the true solutions within some pre-established order of accuracy. The second major concern is that they make advantageous use of available computational resources. Both conditions combine to define a model's predictive ability: how well a model replicates observed scenarios, and for how long it does (Anthes et al. 1989). In this context, the choice of the time-step plays a prominent role, and forces a compromise between two conflicting factors: (a) to stretch the size of the time-steps as much as allowed by requirements of numerical stability so as to optimize computation times, and; (b) to resolve adequately both fast and slow processes [in this context, transport is a fast process, and thermodynamical processes are slow, since during the average time of cloud formation (~ 40 minutes), a storm travels about 24 km for an average wind speed of 10 m s^{-1}] it is necessary to assure internal consistency between the range of scales over which the physics can be represented by the model. In summary, fast processes guide and set the upper limit in the selection of the time-step size.

The decision of the computational time-space frame of reference rests in part on the need to represent fast and slow processes adequately. The numerical methods used in orographic precipitation models fall into one of two major classes according to their time-space frame of reference: Eulerian methods describe the history of a state variable as a succession of snapshots taken at fixed points in time, with a constant field of view; Lagrangian methods track the fate of the state variables as they evolve in the time domain. Aside from implications for model accuracy and long-term model performance, the choice of which class to use determines the time-span of model simulations.

Theoretically, the time-step in Lagrangian methods should equal the simulation time, in which case spatial discretization would be the exclusive source of error. However, Lagrangian methods do not preserve mass in the strict sense [the domain of integration is not closed with respect to time, which leads to effects such as the Stokes' drift in wave driven transport]. Also, the implementation of these methods is based on the presumption of oscillation-free advection operators [the velocity fields defined by u(x,y,z,t), v(x,y,z,t), and w(x,y,z,t) need to be monotonic continuous functions in the solution space]. The latter assumption does not hold for long periods of time in the case of the highly nonlinear dynamics of atmospheric processes. For these reasons, the time-step size in a Lagrangian schemes is bounded (Smolarkiewicz and Rash 1991).

Eulerian schemes are plagued with numerical errors resulting from aliasing inherent to the period at which a solution is "sampled", that is, the time-step. The length of the time-step in the simulation of conservative transport in a homogeneous flow field is unlimited for Lagrangian schemes, whereas it is bounded by the Courant number condition [$Cu = \frac{u \Delta t}{\Delta x} < 1$] in the case of explicit Eulerian schemes. The partial differential equations include source/sink terms such as those in Eqs. (2.4), (2.5) and (2.6), and decay terms of various kinds, such as diffusion. These terms incorporate ellipticity into the equations, which cannot be handled by Lagrangian methods, although they can be suitably handled by sophisticated Eulerian methods. In situations such as these, instead of switching to fully Eulerian methods, a better strategy may be to solve advection in a Lagrangian framework, and then solve the remainder phenomena [cloud microphysics] in an Eulerian mode (Barros and Lettenmaier 1993a, Smolarkiewicz and Rash 1991). This approach is known as Eulerian-Lagrangian or Semi-Lagrangian.

The Cartesian coordinate system is used in most of the orographic precipitation models which are based on analytical or semi-analytical solutions of linearized fluid flow and thermodynamic equations. However, because of orographic irregularity at the surface boundary, terrain-following coordinates [mapping schemes based on a vertical coordinate normalized with respect to surface pressure p_s and the pressure at the uppermost atmospheric layer p_t, such as the sigma coordinate $\sigma=(p-p_t)/(p_s- p_t)$] are used in non-linear numerical models (Anthes et al. 1989, Mesinger and Janjie 1985). These include numerical weather prediction models for which there is a need to compute adequately the pressure gradient force, and models which allow for tracking of high-resolution orographic effects in the boundary layer between the surface and 850 hPa (Anthes et al. 1989, Nickerson et al. 1986, Durran and Klemp 1983).

2.4.2 Space-Time Discretization

Modeling of complex physical phenomena implies inevitably some degree of approximation in the space-time representation of the study domain. Analytical models have little application because the mathematical solutions on which such models are based require a continuous representation of orography. Continuous representations of orography consisting of bell-shaped curves fitted to the width and height of the orographic barriers to be modeled, or, composite curves resulting from the summation of sine and cosine functions obtained through Fourier decomposition of digital elevation data have been used (Carruthers and Choularton 1983 and 1986, Gocho 1978, Sarker 1966). In the case of numerical models, the fundamental issue is spatial discretization and, therefore, how well a region's orography can be resolved.

Major factors in the discretization process concern the preservation of spatial gradients, and the preservation of the location and properties of saddle lines (ridges, valleys, and basin divides). A model's ability to preserve these properties in its description of complex terrain is determined by computational considerations, the nature of the application itself, and the spatial properties of the data available for calibration and verification purposes.

In numerical weather prediction [e.g. models such as the NMC or the ECMWF], two approaches have been used to represent topographic features (orography): (1) mean orography; and (2) envelope orography. The first consists of taking the grid square mean elevation, the second results from adding a multiple of the standard deviation of the subgrid scale elevations to the grid square mean (Jarraud et al. 1987). Envelope orographies capture better the maximum heights as compared to the aliased mean orographies as illustrated by Fig. 2.6. On the other hand, topographic variations are smoothed, and the average elevation is increased, in envelope orography relative to mean orography (this characteristic is sometimes referred to as volume spreading), which makes envelope orography a bad choice for the representation of isolated mountains, and for mesoscale modeling in general. For grids used in regional and mesoscale modeling, the elevations of nodal points are obtained from averaging or interpolating among a number of neighboring pixels in the supporting Digital Elevation Map (DEM), or by making the location of grid points coincide with the center of individual DEM pixels. The order of the interpolation depends upon both the model and DEM resolution and the degree of topographic complexity within the limits of a threshold area of influence.

With exception of the debate between the use of mean or envelope orography in numerical weather prediction, the discussion of discretization strategies generally has been relegated to a secondary position in the literature. This situation appears to have resulted not from an intentional lack of appreciation for the implications of this issue, but rather from the discomfort scientists feel when using arbitrary discretization techniques such as averaging and interpolation. Among the few direct investigations of the effect of discretization on model performance, Collier (1977) investigated the dependence of model-predicted rainfall on model resolution. He concluded that, for storms characterized by a dominant orographic component of rainfall, model predictions showed improvement with the decrease of grid-size down to the length at which vertical velocities could be computed accurately [between 1 and 2 km in his study]; an exception was that significant overestimation of precipitation occurred when large-scale baroclinicity dominated. Another indirect source of information about the effect of resolution on model accuracy comes from studies using nested grid models. Figure 2.7 shows statistics of twenty-four hour rainfall forecast errors for selected sites in Wales and central England using the U.K. Meteorological Office model (a) without and (b) with nesting of a diagnostic model of orographic precipitation. In this application, each grid cell of the weather prediction model contained four grid cells in the orographic model (Bell 1978). The nested grid results are a clear improvement over the direct application of the (coarser scale) model. Care must be taken in interpretation of the results of both Collier (1977) and Bell (1978), however, because errors inherent to the parameterization or exclusion of some physical processes in either model are confounded with the effects of model resolution.

The smallest scale that can be resolved by the present generation of orographic precipitation models is about 5 km; more typical spatial scales are in the range 10-60 km. Within this range, errors related to subgrid effects remain. Radiometric measurements of an orographic cloud system by Sassen et al. (1990) give some idea of the smallest spatial scales at which orographic phenomena might be important. They found embedded isolated pockets of supercooled water droplets, the spatial locations of which were clearly linked to steep slopes, isolated peaks, and modest hills located along the path of wind direction, with a horizontal scale less than one km. Since feeder-seeder interaction within an orographic cloud system appears to be more efficient when supercooled regions play the feeder role, these results suggest that significant variations in orographic activity will occur at spatial scales considerably less than are likely to be resolved by orographic precipitation models in the foreseeable future.

2.4.3 Calibration and Validation

Calibration is the process of estimating those parameters of a model which are specific to a particular application that cannot be determined directly from physical principles or controlled experiments. Model validation is the process of testing a model to assure its proper performance. Ideally, model calibration and validation should be conducted using independent data sets (depending on the model, different time periods or events). Because model calibration involves comparison of model predictions with observations, and adjustment of model parameters to reproduce the observations to the extent possible, such data should not be used to assess model performance. Care must be taken to avoid overfitting, which results when too many degrees of freedom are used for calibration purposes, so that the apparent performance of the model with respect to the calibration data is better than in an independent validation period. For statistical methods, such as regression, there are well-established methods for parameter estimation which prevent overfitting from occurring. For deterministic models, such as those discussed here, there is no such theoretical framework for parameter estimation, and validation with independent data sets is essential.

Calibration and validation of orographic precipitation models following the above procedure are uncommon. One major problem is that the basis for assessing performance of these models is usually their ability to reproduce point rainfall data, which are often sparse with respect to the spatial domain of the model, and many times are lacking at high elevations. One important use of high-resolution orographic precipitation models is to predict sub-network scale spatial precipitation patterns. In addition, the difficulty in calibrating and verifying many existing models of orographic precipitation is that they have been developed for episodic one or two-dimensional simulations integrated in numerical experimentation studies. Only a few such applications have been verified against gage precipitation (Collier 1975; Bell 1978; Richard et al. 1987; Gollvik and Omstedt 1988; Oki and Koike 1989). Validation has also been attempted against satellite imagery of long-term snow cover (Bagchi 1982), and radar precipitation estimates (Alpert and Shafir 1989, Takeya et al. 1989). Many research applications have been directed towards sensitivity studies of cloud microphysics processes (Storebo 1976, Carruthers and Choularton 1986, Robichaud and Austin 1988), or attempts to establish consistent regressions between orographic indicators [width, length, slope], storm direction and measured precipitation (Oki and Koike 1991, Peck and Schaake 1990, Carruthers and Choularton 1986, Hendrick et al. 1978).

Calibration and validation remain one of the most challenging of the tasks involved in orographic precipitation modeling. Because of the remoteness and inaccessibility of mountainous areas, the lack of ground truth data is almost universal except for a few cases where orographic barriers are located in critical socioeconomic regions of major industrialized countries. One data set resulted from Project Pluvius, as a part of which about 1000 gages were installed in Sweden in the 1960's (Bergeron 1960b). Nickerson et al. (1986) used data from 361 precipitation stations to validate their one-event simulation of rainfall over the French Vosges and the Black Forest in Germany.

Weather radar can be a good indicator of the spatial distribution of the rainbands associated with the heaviest rainfall rates within a precipitating system, while Doppler radar measurements can be used to infer associated wind fields (Parsons and Hobbs 1983, Browning 1989, Rauber 1992). Unfortunately, the value of radar rainfall estimates for calibration and validation of orographic precipitation models is limited due to the corruption of the backscattered signal by terrain in the vicinity of mountains. Infrared and microwave imagery of atmospheric water can be useful to identify cloud type, extent, movement and position of cloud top. However, the retrieving algorithms used currently for scanning the atmospheric column are unable to distinguish what happens below cloud tops, so these methods generally are not reliable for estimation of orographic precipitation, which is a low troposphere phenomena.

A different approach to model validation is to verify the volumetric water balance of river catchments:

$$P = Q + E + \Delta S + \Delta S_n \tag{2.12}$$

where, over a time period t, P is precipitation over the catchment area, Q is streamflow, E is evapotranspiration, S is soil moisture and canopy storages, and S_n is snow water storage. Surface energy and runoff models must be coupled to orographic precipitation models to estimate evapotranspiration, snow accumulation and ablation, infiltration, and soil moisture storage. Over a relatively long period (a North American water year, from October 1 to September 30), it may be possible to neglect the terms ΔS and ΔS_n, which simplifies the water balance considerably. In regions of high precipitation and low evapotranspiration, it may be possible to obtain a fairly accurate estimate of long-term precipitation even if the estimate of evapotranspiration is poor.

Given the difficulty of obtaining adequate data for model calibration and validation, the standard validation strategy of attempting to replicate observed values of the prognostic fluxes at specific locations and times has sometimes been relaxed. Elliott (1977) grouped stations located along the predominant storm-tracks according to their elevation, and subsequently calibrated the model against the mean precipitation values observed within some elevation band and for each one of four distinct orographic cloud systems [warm stable, warm unstable, cold stable, cold unstable]. Nickerson et al. (1986) used point daily precipitation data to verify their six hour simulation. Giorgi and Bates (1989) compared the average monthly precipitation of dozens of stations distributed

distributed over areas of the order of thousands of km in the Western U.S. with the corresponding model areal averages. Barros and Lettenmaier (1993a) used a rough estimate of evapotranspiration and measured streamflow data to permit approximate validation of the long-term spatial distribution of precipitation.

The limitations intrinsic to such exercises restrict the calibration and validation processes. Averaging the observations of similar events at multiple stations precludes validation for single events or continuous simulations. Likewise, comparison of daily and hourly data leads to, at best, a qualitative validation. Averaging of data from a large number of stations independently from their elevations and distances from the ocean and from large mountain barriers can be used to verify large-scale mass balance but it does not allow validation of the model's ability to reproduce the fundamental controls of orography on precipitation. Finally, the absence of a coupled model of precipitation and surface hydrology limits use of hydrologic data for validation of large area precipitation to the annual time scale.

Alternative approaches to model calibration are possible for cases where orographic precipitation models have been coupled with 4D data assimilation methods (Browning and Collier 1989, Alpert and Shafir 1989, Collier 1977). Such methods combine precipitation predictions from an orographic precipitation model with radar and precipitation gage data to produce estimates that are more accurate than could be obtained from any of the three sources alone. The coupling of data assimilation procedures with a deterministic model of orographic precipitation has the additional advantage that it offers a framework for model calibration and validation. Rather than attempting to adjust the parameters of the orographic model to reproduce precipitation at particular gage locations, the parameters of the orographic precipitation can be approximated, and the parameters of the data assimilation models can be estimated to produce point precipitation values. In this way, the data assimilation procedure is used to remove local biases attributable to resolution effects, and the parameters of the orographic precipitation model produce more general, large scale features. One of the potential problems with assimilation approaches is the need to establish independence criteria between data used to impose boundary conditions and data used to calibrate the model.

Model calibration and validation must be treated as location-specific. This is demonstrated well in Fig. 2.8, where model results obtained for the San Juan massif in Northern California [Fig. 2.8a] are compared with model results for the Wasatch massif [Fig. 2.8b] (Elliott 1977). The parameters calibrated for unstable cold conditions in the San Juan massif were used for similar conditions in the Wasatch massif, with poor success. The need to repeat calibration and validation for each new application is universal for M2 type models.

2.5. Intercomparison of Model Performance and Applicability

Of the many models reported in the literature and referred to in this review, only a handful have been validated using surface measurements. Most of the models based on complex parameterization schemes of microphysical processes have been used solely for sensitivity studies (e.g. Hobbs et al. 1973, Carruthers and Choularton 1983 and 1986, Meyers and Cotton 1992). In this section, we focus on the performance of models that have been tested against surface observations.

The final product of an orographic precipitation model consists of the time-history and the spatial distribution of precipitation at the ground. The time-history of orographic precipitation is linked intrinsically to the duration of model simulations, and the length of the time-step used. Models intended for long-term hydroclimatological applications, such as those of Giorgi et al. (1993) and Barros and Lettenmaier (1993a), have been used to simulate precipitation patterns for periods of time as long as two and eight consecutive years respectively. The former was possible through access to exceptional computational resources (several hundred hours Cray X-MP time); the latter was possible by implementing a model with prescribed circulation in a semi-Lagrangian framework. Short-term simulations traditionally [2-12 hours] have been associated with weather forecasting and the prediction of maximum probable floods.

Model dimensionality [2D versus 3D] strongly affects the feasibility of long simulation lengths. Unless the spatial scale is quite coarse or the simulation period short (e.g., days versus months or years) long-term 3D simulations require that circulation be prescribed. Although 2D models are computationally less demanding, such models are valid only when the computation grid is representative of the region along the path of the prevailing winds. Fig. 2.9 shows the distribution of orographic updrafts for storms coming from two distinct directions and advancing over the Orofure Mountains region in Japan (Takeya et al. 1989). In this region, the relationship between precipitation amounts and the intensity of orographic updrafts is linear, and the figure shows clearly that a 2D grid built on an elevation slice oriented along the direction of approach of one of the storms would not be able to handle the change in wind direction for the other storm. This effect is ameliorated upwind of extended mountain barriers [e.g. the Cascade or the Sierra Nevada Mountains], but can be dramatic in the case of isolated mountains, small orographic complexes, and to leeward of large mountains (Sarker 1966 and 1967, Fraser et al. 1973, Colton 1976, Alpert 1986, Cotton et al. 1986, Meyers and Cotton 1992). With few exceptions [e.g. Nickerson et al. 1986], complex models of orographic precipitation are generally 2D in nature, or if three-dimensional [3D] they have been used and validated as a 2D model. Therefore, such models can only be used for the simulation of single events. Long-term continuous simulations can only be achieved by three-dimensional [3D] models.

Regarding the evaluation of the performance of 2D orographic precipitation models, two common characteristics can be identified: (1) model verification concentrates on upwind effects [this is illustrated for the Western Ghats and the Sierra Nevada Mountains in Figs. 2.10 and 2.11], and; (2) when errors are defined as $\frac{(P_s - P_o)}{P_o}$, where P_s and P_o are respectively simulated and observed precipitation amounts, the typical error magnitudes at the location of precipitation gages are within the range between 35 and 50 percent for time-steps of the order of minutes. Occasionally, these errors can be below twenty percent at individual stations for particular storms (Sarker 1966 and 1967, Rhea 1978, Colton 1976, Alpert 1986). Models based on M1 type parameterization schemes do not appear to perform better than highly simplified models. This is shown in

Fig. 2.12 for the results of the application over northern Colorado of a complex 2D, non-hydrostatic model, which included descriptions of ice-particle vapor-deposition growth, riming, aggregation, and nucleation mechanisms (Cotton et al. 1986). The shaded area in Fig. 2.12 represents the range within which fall the results of several numerical experiments, which consisted of turning off one or more microphysical processes. This does not imply necessarily that calibration dependent models [M2] are preferable to physics oriented models [M1]. It indicates state-of-the-art model limitations, which are the result of the multiscale characteristics of precipitation, among which the interactions between circulation dynamics and microphysical processes play prominent roles.

3D models (Nickerson et al. 1986, Giorgi and Bates 1989) have been verified not only against point data, but also against spatial patterns constructed from monitoring networks, or alternative data such as streamflow and snowpack records. Both upwind and leeward stations have been used in the evaluation of model performance, such as the case illustrated by Fig. 2.13 for two upwind and two leeward stations in the Olympic Mountains (Barros and Lettenmaier 1993a).

Because orographic effects are the only effective precipitation trigger in many orographic precipitation models, the results obtained often show evidence of the following characteristcs: (a) too little precipitation in days of strong convective activity; (b) too little precipitation in very cold dry days; (c) too little precipitation in the low elevation regions surrounding a mountainous formation; and (d) excessive precipitation when the orographic component is the predominant component of precipitation. To reduce the influence of these errors, model results often are post-processed. This additional filtering can be introduced formally either as part of the parameterization and the verification processes (Elliott 1977, Peck and Schaake 1990, Barros and Lettenmaier 1993a), or arbitrarily as a corrective coefficient based on the ratio $\frac{P_o}{P_s}$ (Alpert 1986). To account for spatial variability, Elliott (1977) introduced a corrective drift parameter which, for different cloud types, was obtained by a multiple regression involving observed precipitation, 700 hPa winds, cloud depth above the mountains' crest, crest height above cloud base, and atmospheric stability. Barros and Lettenmaier (1993a) also used a multiple regression involving the characteristics of precipitation at coastal stations. distance away from the coast, topographic slope. and elevation in an attempt to account for the effects of coastal circulations on the triggering and feeding of low level precipitation. Additional processing has been used at the time of validating model results by aggregating together stations over wide regions, or by aggregating them in groups according to their elevation or location with respect to storm approach, and therefore smoothing errors through averaging (Elliott 1977, Rhea 1978, Giorgi and Bates 1989).

2.6. Summary

The current state of knowledge upon which orographic precipitation models are based can be summarized as follows:

(a) Orographic modulation of rainfall upwind of a topographic divide can reach values that vary from 50-85 percent for low topographic features [hills from tens to a few hundred meters high] to more than 200 percent for high elevation areas [above 1-2 km] (Storebo 1976, Browning 1980, Hobbs et al. 1973, Robichaud and Austin 1988, Corradini and Melone 1989).

(b) For low to moderately high and narrow mountains [e.g. half-width < 10 km], the orographic effect consists of the intensification of pre-existing rain from stratiform clouds by means of a seeder-feeder type of interaction with the cap clouds (Browning 1980, Rutledge and Hobbs 1983, Robichaud and Austin 1988, Gocho 1978).

(c) In the case of rainfall alone [warm clouds], or rainfall and graupel, the peak orographic enhancement is upwind of the topographic peak, and there is a strong negative gradient in the lee side [the precipitation maximum and its upwind displacement increase with precipitation intensity (Hendrick et al. 1978, Carruthers and Choularton 1986), although significant amounts of low-level moisture may affect atmospheric stability, and in some cases may eliminate orographic modulation completely (Richard et al. 1987, Robichaud and Austin

1988)].

(d) When precipitation falls in solid form, its distribution over low to moderately high mountains includes a tail that spreads over the lee side, due to improved efficiency of horizontal advection relative to the terminal fall speeds of ice particulates (Hobbs et al. 1973, Choularton and Perry 1986).

(e) The dynamics of flow deformation by orography prevail over cloud microphysical processes with respect to the bulk quantification of precipitation (Rhea 1978, Richard et al. 1987, Robichaud and Austin 1988, Barros and Lettenmaier 1993a, Meyers and Cotton 1992).

(f) Precipitation rates show an almost linear relationship with the horizontal low-level wind velocities and the orographic updrafts (Collier 1975, Bell 1978, Gollvik 1984, Carruthers and Choularton 1986. Richard et al. 1987).

(g) Vertical motion ranging from the synoptic to the scale of the local orographic gradients, is the variable to which orographic precipitation rates and amounts have the highest correlation (Cotton and Anthes 1989, Dunn 1991).

Regarding their representation of physical processes, two types of models have been identified: M1 models, which include both extended representations of flow and cloud dynamics, and make wide use of complex conceptual schemes to parameterize microphysical mechanisms; and M2 models, which are based on highly simplified representations of flow and cloud processes, and rely strongly on the bulk-parameterization approach. On the basis of their ability to reproduce surface precipitation measurements, present validation capabilities suggest that complex M1 models offer no superiority over simpler M2 models that are locally calibrated for local conditions.

The implementation of orographic precipitation models requires consideration of both computational resources, and the integration and application of scientific knowledge; many physical processes are not understood, or have not been identified. Efforts to close the gap between a model's range of applicability in both time and space domains and the implementation of coherent descriptions of physical phenomena have been conducted on two fronts: investigation of numerical solution techniques to aid processing speed and the handling of highly non-linear phenomena [the development of semi-Lagrangian methodologies]; and experiments to unravel the hierarchy of governing processes. and their mutual interactions [sensitivity studies, flight and radar measurements].

There is a need to focus further research activity on exploration of new and efficient 4D analysis techniques to facilitate the incorporation of a growing and diverse data base [radar, satellite, monitoring stations] into the structure and routine use of models, and the development of aggregation and disaggregation methods to tackle the multiscale challenge. The ultimate objective is the realization of long-term simulations [several years], with the detail necessary to discern snow and rainfall patterns [when and where and how much] at the time-scale of the mean storm duration in the study region. 4D analysis may be feasible in the case of both weather forecasting and hindcasting, as well as for calibration and validation at the time scale of individual storms of cloud properties, the paths of active raincells, and precipitation rates.

One apparently feasible way to forge the integration of complex microphysics into fast numerical models is through across-scales aggregation of those processes. On the other hand, the description of precipitation features at the spatial scales of orographic complexity requires the implementation of disaggregation tools. This can be achieved by exploring scale sorting approaches such as multiscale computational methods, or the implementation of existing models in parallel computers. Multiscale computational methods imply the creation of multilevel solutions resulting from the combination of partial solutions of a limited number of processes per grid level, the resolution of which is consistent with the dominant length scales. A similar effect can be created by developing a hierarchy of groups of processors in parallel implementations. Separate groups of processors may be used to track the evolution of groups of processes operating at distinct scales. Communication among processors can be established through software valves developed to regulate the fluxes of information at appropriate time nodes, which can be designed according to the frequency requirements used to guarantee proper updating of boundary conditions in nested modeling.

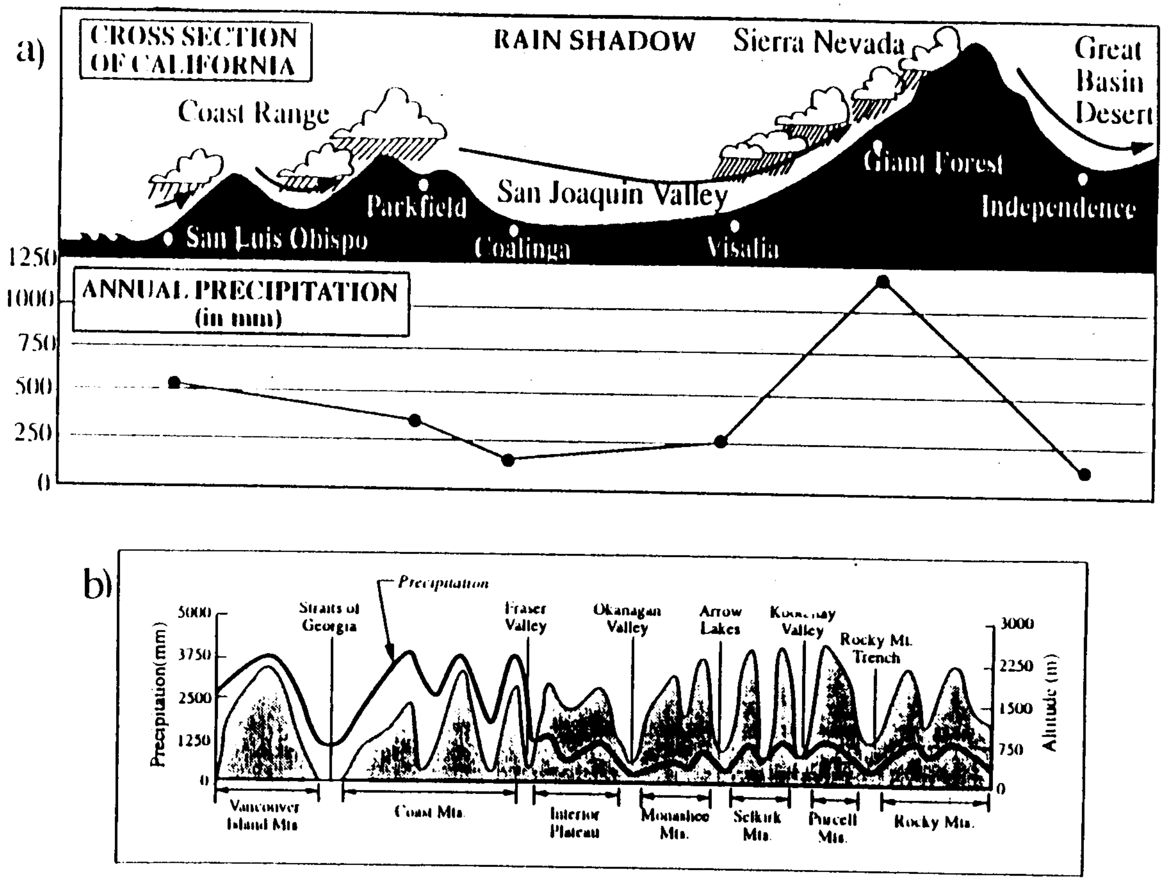

Figure 2.1 Elevation and corresponding precipitation profiles: a) Sierra Nevada Mountains; b) Western Canada, along the Canada-USA border. (After Anderson 1975 and Klemes 1990, respectively)

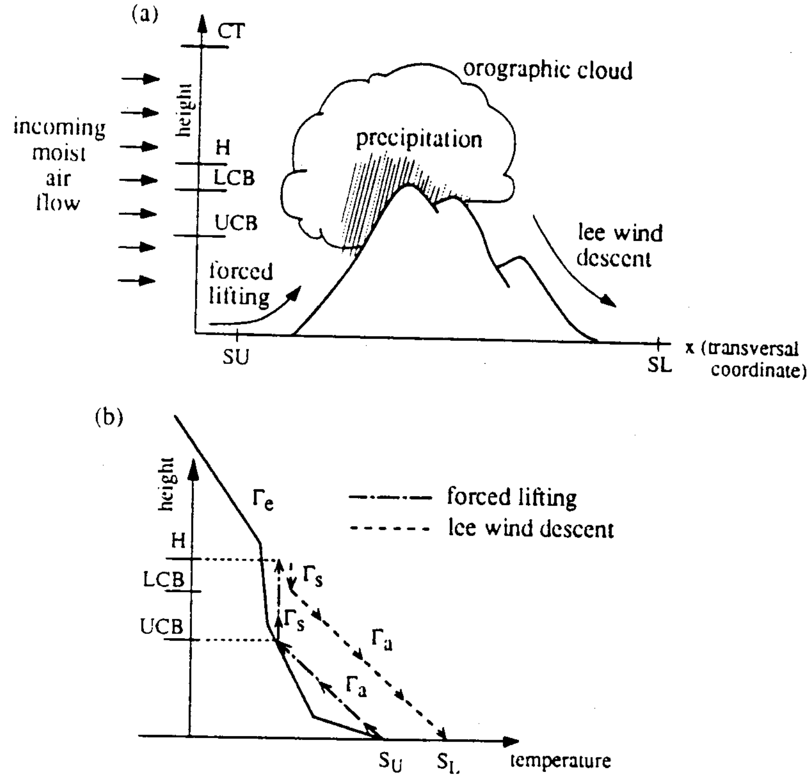

Figure 2.2 Development of orographic cloud systems: a) illustration of the orographic lifting effect; b) pseudo-adiabatic chart representation. (After Sumner 1988)

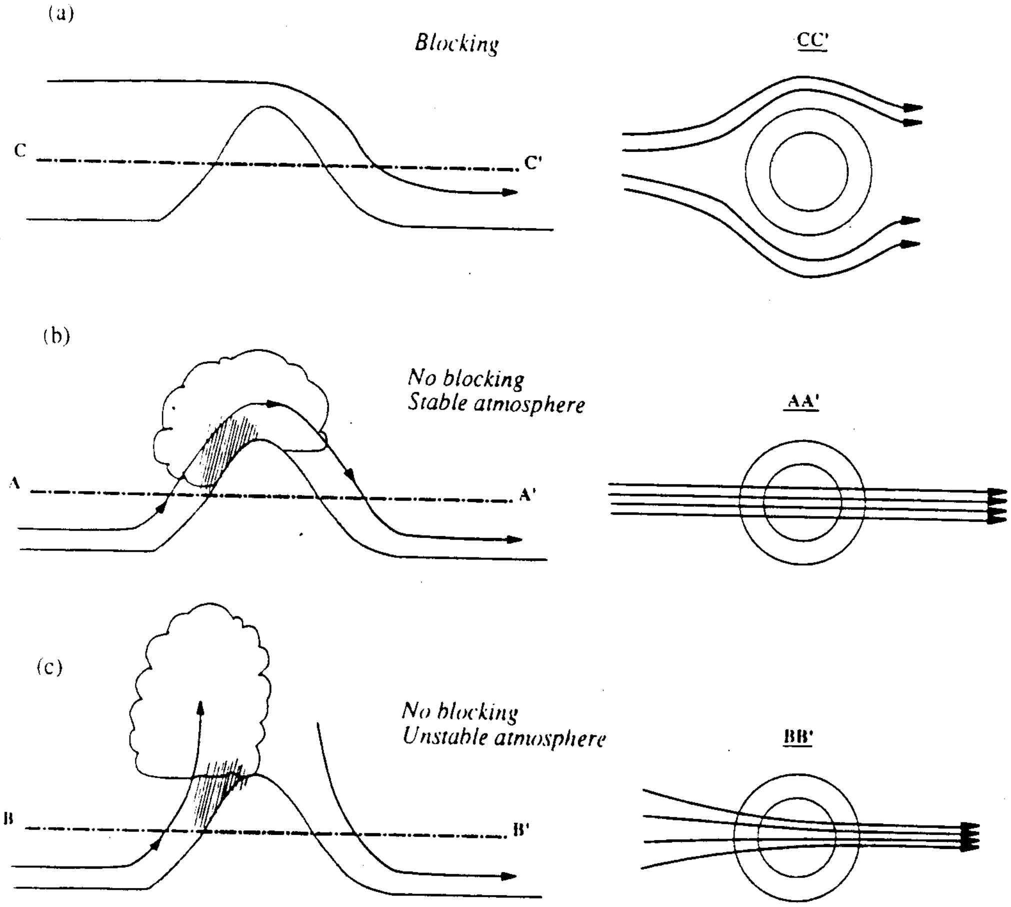

Figure 2.3 Orographic influences on atmospheric circulation: a) blocking; b) no blocking in a stable atmosphere; c) no blocking in a conditionally unstable atmosphere. (After Barry 1981)

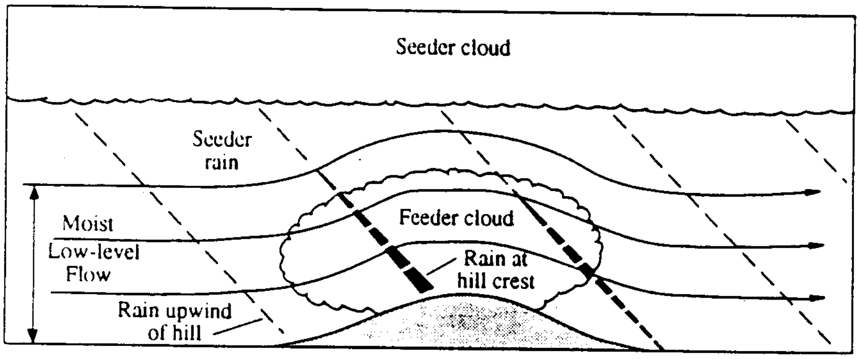

Figure 2.4 Conceptual representation of the seeder-feeder mechanism; dashed line thickness indicates relative precipitation amount. (After Cotton and Anthes 1989)

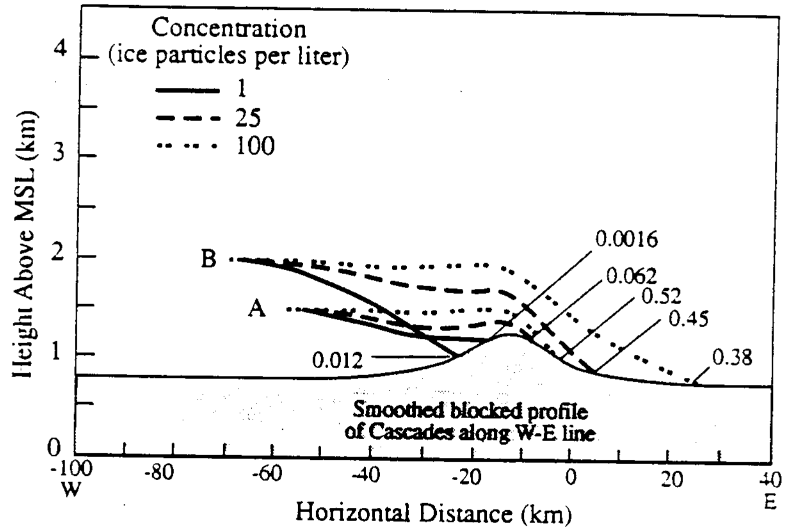

Figure 2.5 Snow drift effects for precipitation particles by deposition riming over the Cascade Mountains in a westerly airstream with simulated blocking. The number at the end point of each trajectory is the total mass (mg) of precipitation that reaches the ground at that point originating in a volume of 1 liter at the starting point of the trajectory. (After Hobbs et al. 1973)

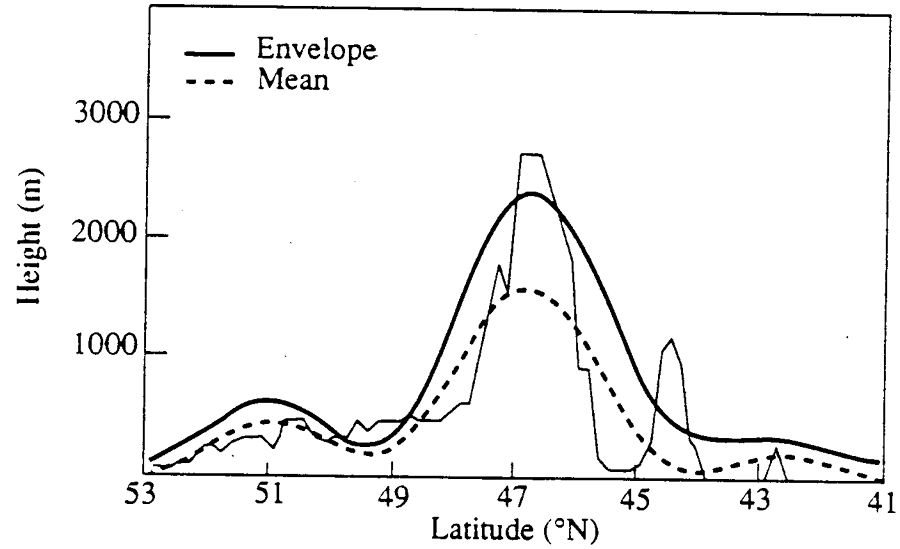

Figure 2.6 Envelope and mean orography approximations of terrain elevation for a north-south transect between 53°N and 41°N at 105°E in the T106 version of the ECMWF weather forecast model. (After Jarraud 1987)

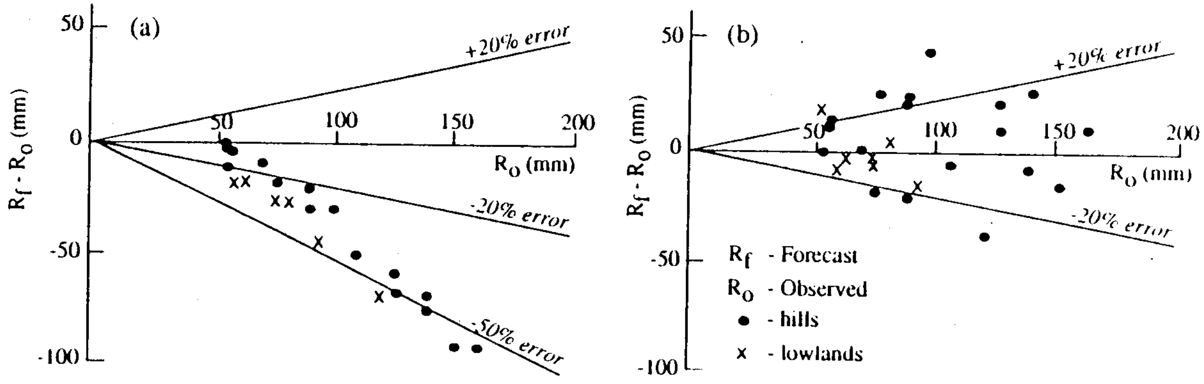

Figure 2.7 Twenty four-hour precipitation forecast errors as a function of observed rainfall amount for selected Wales and central England sites for a two-week period: a) 10-level U.K. Meteorological Office model; b) 10-level U.K. Meteorological Office model nested with a higher resolution diagnostic model of orographic precipitation. (After Bell 1978)

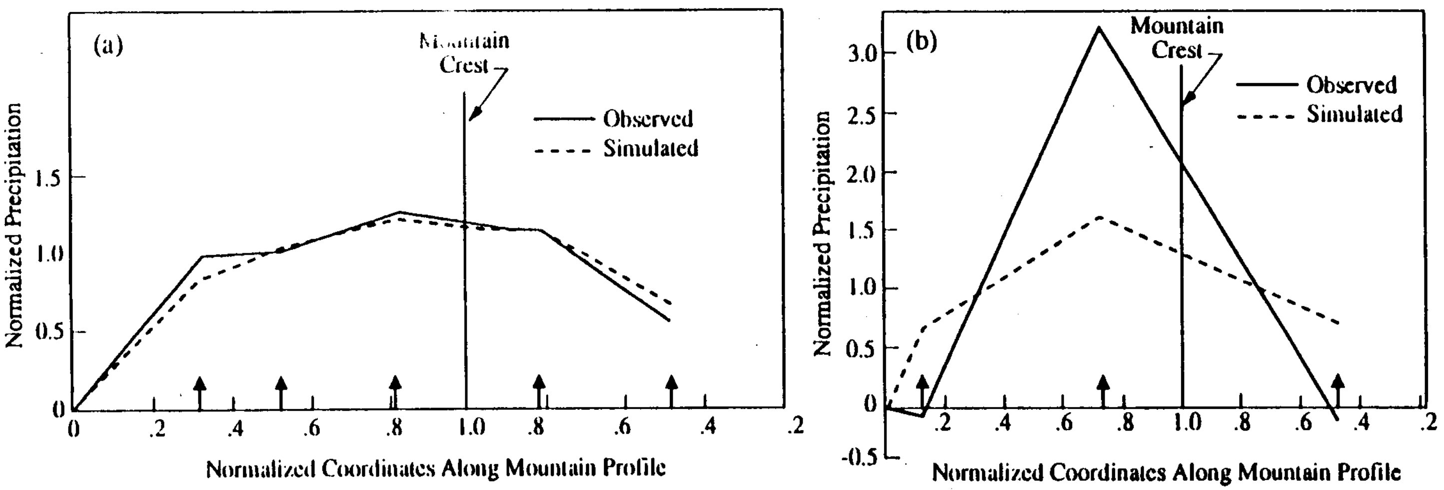

Figure 2.8 Distribution of normalized observed and simulated precipitation along the transects of two mountainous formations: a) San Juan Mountains in Colorado: calibrated experiment; b) Wasatch massif in Utah: non-calibrated experiment. (After Elliott 1978)

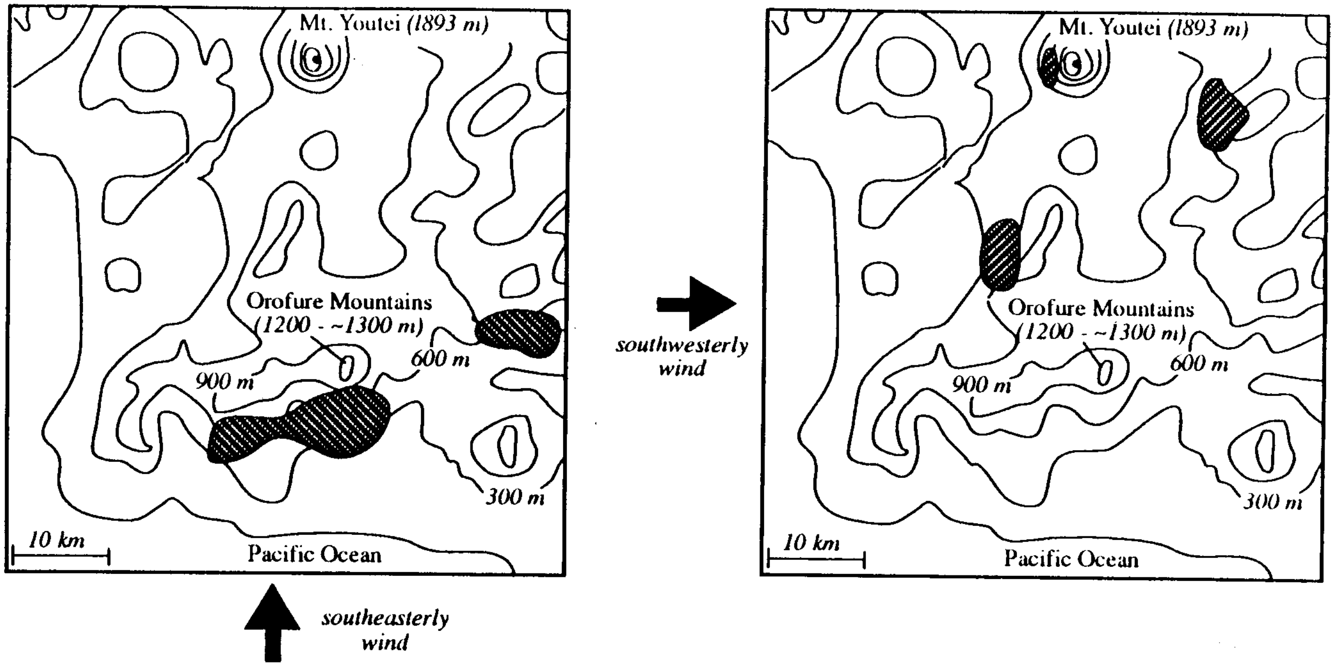

Figure 2.9 Spatial distribution of regions of strong updrafts for south-easterly and south-westerly storms over the Orofure Mountains, Japan. (After Takeya et al. 1989)

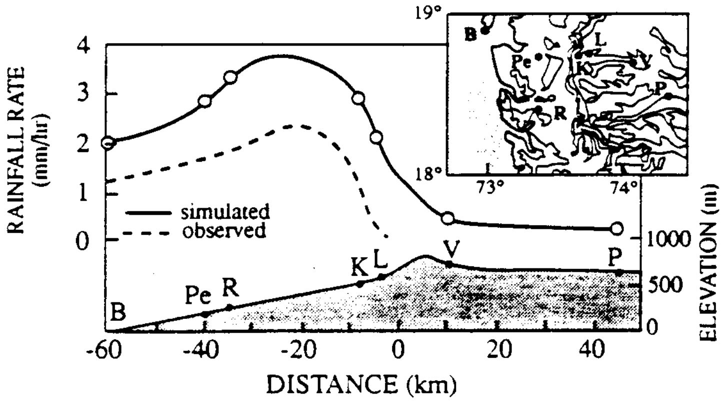

Figure 2.10 Simulated and observed rainfall for a weak monsoon day over the Western Ghats,India. The inset shows the spatial distribution of the precipitation stations. (Modified after Sarker 1966)

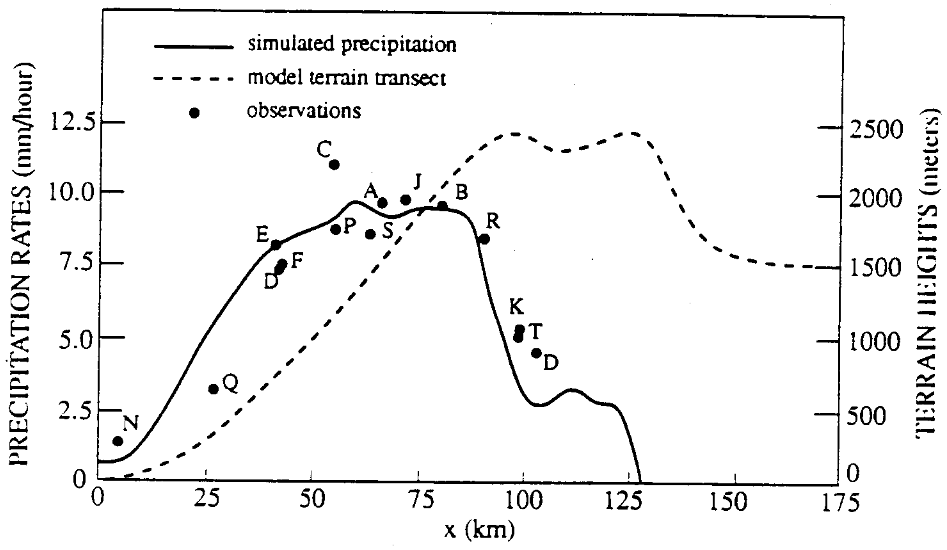

Figure 2.11 Comparison between simulated and observed values of accumulated precipitation for the 24 hour period starting at noon on the 21 of December 1955. The lettering indicates the location of precipitation stations within a 6' latitude band, which is centered at 39° 15' N and intersects the Sierra Nevada Mountains.
(Modified after Colton 1976)

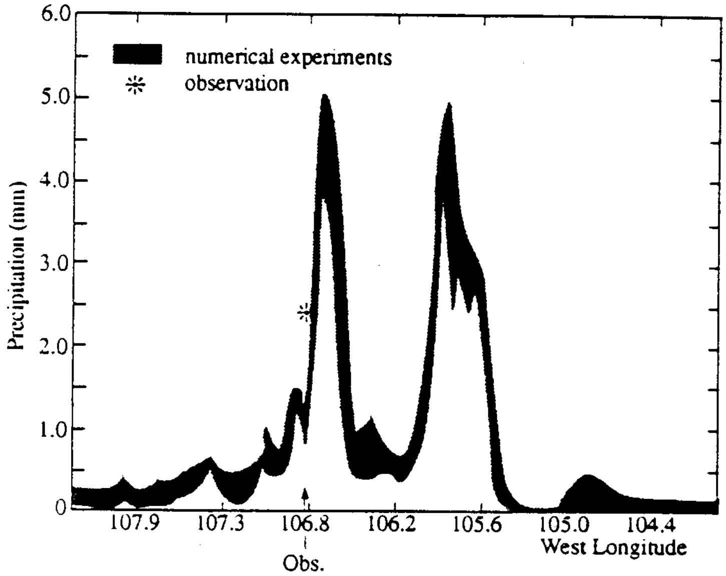

Figure 2.12 Observed and simulated liquid equivalent precipitation accumulated at the ground across northern Colorado.
(Modified after Cotton et al. 1986)

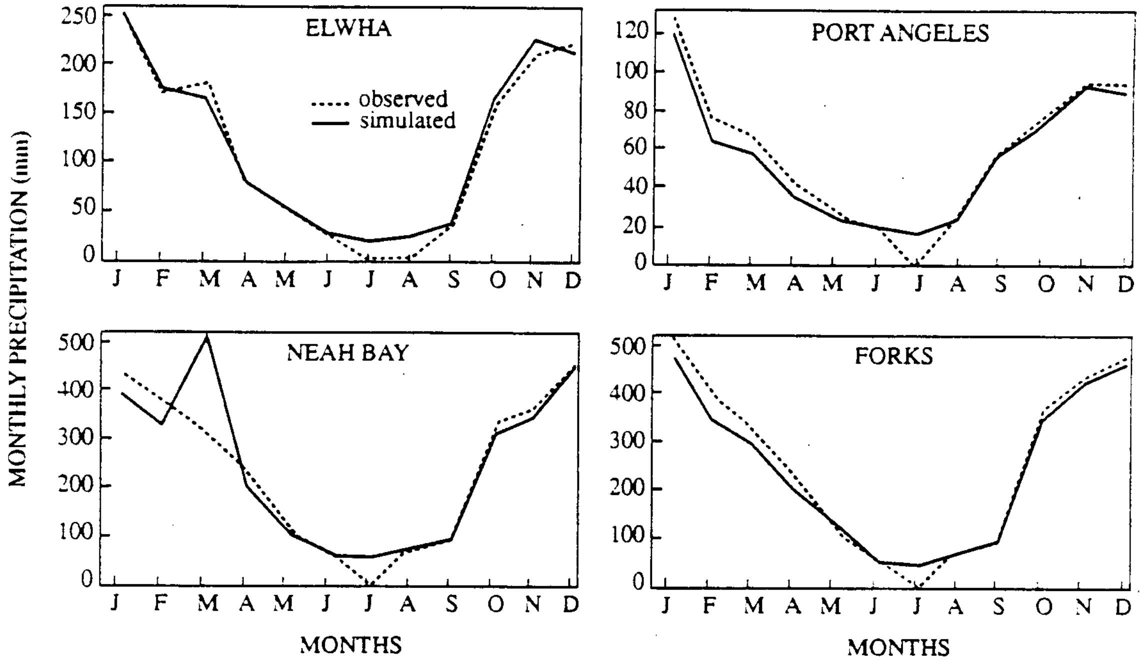

Figure 2.13 Observed and simulated monthly mean precipitation at the location of two leeward (Elwha and Port Angeles), and 2 upwind stations (Neah Bay and Forks), for a period of eight consecutive years.

CHAPTER III - A DYNAMIC MODEL OF THE SPATIAL DISTRIBUTION OF OROGRAPHIC PRECIPITATION

> *"By a model is meant a mathematical construct which, with the addition of certain verbal interpretations, describes observed phenomena. The justification of such a mathematical construct is solely that is expected to work."*
>
> *John von Neumann, cited by Gleick (1988)*

3.1. Introduction

The motivation for improved understanding of the long-term dynamics of orographic precipitation is in part based on the need for better estimates of the areal and temporal distributions of precipitation, which can best be achieved through improved representations of local orography and atmospheric dynamics. This objective cannot be attained with current atmospheric models, because of their limited ability to resolve for the spatial and time scales needed to describe orographic precipitation. For instance, in the case of general circulation [GCM] and limited area models [LAM] (e.g. Giorgi and Bates 1989), the spatial scales resolved are typically around 500 km and 100 km respectively, and hence complex terrain and its effects upon atmospheric dynamics cannot be represented adequately. In the case of mesoscale models, the spatial resolution is of the order of 10 km, but computational costs become prohibitive for simulations of more than a few storm episodes at a time due to the short integration time-steps imposed by numerical stability conditions (Cotton and Anthes 1989). Many 2D and 3D models reported in the literature use a single bell-shaped mountain as a terrain singularity and time-steps on the order of a few minutes. Also, such models have often been developed for the investigation of specific phenomena of atmospheric dynamics in the vicinity of mountains [e.g. dry gravity waves, lee waves], under conditions which may or may not be relevant for prediction of precipitation amounts.

In this Chapter, we describe a regional Lagrangian model for the continuous simulation of precipitation in areas of extreme topographic relief. The model, which simulates the deformation of wind fields by topographic barriers, transports moist static energy and total water through a 3D finite-element grid. The production of water and ice is governed by thermodynamic considerations, while precipitation is parameterized as a sink term, the controlling parameters of which are estimated from surface data. A multi-year investigation of the long-term distribution of precipitation for the Olympic Mountains, Washington, is used to illustrate model performance. The results are validated with gauge precipitation, snow depth and snow water equivalent measurements, as well as streamflow records from which areal precipitation is estimated. The model was calibrated and verified for one year [1967], and the seven subsequent years were used exclusively for model validation. In addition, results from the application of the model in predictive mode are illustrated through generation of quantitative precipitation forecasts for selected storms.

3.2. Model Formulation

The model we describe here is based on prescribed atmospheric circulation, including three-dimensional wind fields, temperature, and relative humidity. Time-series of these variables can be obtained either from an independent atmospheric circulation model, or from observations. We used the latter data-driven approach in the case-study discussed in this Chapter.

3.2.1. Basic Equations

Adiabatic flow is the fundamental thermodynamic assumption of the model. Under this assumption, moist static energy and total water are conservative, and can be used as tracers for the study of the movement of an air parcel in the atmosphere (Cotton and Anthes 1989). The conservation of moist static energy h_M can be stated by the following transport equation:

$$\frac{Dh_M}{Dt} = S(p) \tag{3.1}$$

with

$$h_M = c_p \, T + L \, q_v + g \, z \tag{3.2a}$$

and

$$\frac{D}{Dt} = \frac{\partial}{\partial t} + u \frac{\partial}{\partial x} + v \frac{\partial}{\partial y} + w \frac{\partial}{\partial z} \tag{3.2b}$$

where the scavenging term S(p) is a function of the precipitation rate p; and T and q_v are respectively temperature and water vapor content, c_p is specific heat, L is latent heat of vaporization, g is the acceleration of gravity, and z is the atmospheric height.

The precipitation rate p is the only scavenger of moist static energy considered by the model. The precipitable water q_p is calculated as the excess amount of water that satisfies the continuity of total water Q under saturated conditions.

$$\frac{DQ}{Dt} = p \tag{3.3}$$

$$Q = q_p + q_s \tag{3.4a}$$

and

$$q_p = q_l + q_i \tag{3.4b}$$

where the subscripts s, l and i refer respectively to saturation, and the liquid and ice phases of cloud water.

Condensation is triggered when an ascending air parcel passes its lifting condensation level [LCL]. Although there is no specific treatment of cloud microphysics in this model, we introduced a corrective coefficient η, which modifies the relative humidity conditions for which "effective" supersaturation occurs by acting upon the water vapor content at saturation q_s [e.g. condensation is enhanced by cooling the environment]:

$$q_s^{\star} = \eta\, q_s \tag{3.5}$$

By using this artificial corrective coefficient we intend to account for such processes which occur at a time scale much faster than the one inherent to the model's range of time-steps, and whose effect upon cloud formation and growth is aggravated by orographic lifting. Among others, the conditions which contribute to the signature of fast cloud processes are: (a) the competing effects of cloud drop growth by collision or simple condensation according to the regional concentrations of cloud condensation nuclei (CCN); (b) the presence of high salt concentrations, which activate drop nucleation through the solution effect; (c) abundant drizzle in coastal regions is an important agent of CCN activation, while it also plays the role both of seeder and feeder of cloud formation and growth (Bergeron 1960a, Wallace and Hobbs 1977, Baker and Charlson 1990). The corrective coefficient η [$\eta \leq 1$ for coastal air when $Q > q_s$, $\eta = 1$ otherwise] depends on the mean regional values of CCN and salt concentrations on the study region.

The depletion of condensed water by precipitation is resolved by a linear relationship of the form:

$$p = K\, q_p \tag{3.6}$$

and

$$P(x,y,t) = \int_Z p\,(x, y, z, t)\, dz \tag{3.7}$$

The parameter K, which varies both in time and space, is estimated from surface records of total precipitation. Rain or snow events are partitioned according to the position of the freezing level [FL] through the study domain and the temperature gradient between 850 and 500 hPa (Murray 1952).

3.2.2. Model Implementation

The transport of moist static energy and total water is interpreted by the model using a strategy of decoupling Eqs. (3.1) and (3.3) into equations accounting independently for transport [pathway (1) and (2) in Fig. 3.1], and thermodynamics [pathways (3) and (4) in Fig. 3.1]. Conceptually, this means that air parcels are isolated from interaction with the environment [e.g. no precipitation] while they travel between two locations, and precipitation is controlled by a point release process that is switched on or off as determined by thermodynamic considerations.

The use of this methodology was motivated by the necessity to resolve the difference between the horizontal scales of synoptic motions [on the order of 1000's of km] and the orographic updrafts [on the order of 100's of m] in the space domain, so that the time scale of precipitation [minutes] can be preserved for long periods of simulation [years]. Therefore, Eqs. (3.1) and (3.3) are partitioned into two pairs of equations: one for total advection of h_M and Q, Eqs. (3.8a) and (3.8b), which account for both horizontal and vertical components, and a second pair, Eqs. (3.14) and (3.15) to describe depletion of h_M and Q by precipitation. The latter is used only when the necessary thermodynamic requirements are met.

$$\frac{Dh_M}{Dt}\Big|_\xi = \frac{\partial h_M^\xi}{\partial t} + V_\xi \cdot \nabla_\xi h_M = 0 \tag{3.8a}$$

$$\frac{DQ}{Dt}\Big|_\xi = \frac{\partial Q^\xi}{\partial t} + V_\xi \cdot \nabla_\xi Q = 0 \tag{3.8b}$$

where ξ refers to the transport mode.

The initial boundary-value problem defined by Eqs. (3.8a) and (3.8b) is hyperbolic. This means that the quasi-linear partial differential equation associated with it has three families of characteristic lines in the real domain, which are defined by $[x \pm ut]$, $[y \pm vt]$, and $[z \pm wt]$ respectively. Prognostic applications of Lagrangian methods take advantage of the hyperbolic form of the equations by tracking along the characteristic lines of the solution space the trajectory of a state variable from a point [x,y,z] to a previous position [backwards method of characteristics - BMC]. Due to its high variability, the 3D advection field is well-suited to a Lagrangian framework, which allows for the tracking of air parcels at the scale of all three velocity components without numerical compromises.

Accordingly, we implemented Eqs. (3.8a) and (3.8b) in the form of a 3D adaptive BMC, which uses a 5th order Runge-Kutte method to solve for the three characteristic equations:

$$\frac{dx}{dt}\Big|_\xi = u\ (x,\ y,\ z,\ t) \tag{3.9a}$$

$$\frac{dy}{dt}\Big|_\xi = v\ (x,\ y,\ z,\ t) \tag{3.9b}$$

$$\frac{dz}{dt}\Big|_\xi = w\ (x,\ y,\ z,\ t) \tag{3.9c}$$

Theoretically, the time-step in Lagrangian methods would equal the simulation time, and consequently interpolation in a discretized space would be the exclusive source of error. In fact, we can describe the velocity field defined by u, v and w only in discretized form (i.e. wind fields are updated only when new boundary conditions are available), and not as continuous functions in the solution space. Because the uniqueness of the solutions of Eqs. (3.8a) and (3.8b) is only certain within the limits of approximation of the velocity field, the time-step in Lagrangian schemes is eventually constrained by the variability of the flow field itself: the time-step cannot exceed the interval during which the assumptions that u, v and w are constant hold. In this case, we implemented an adaptive time-stepping procedure, which reconciles automatically the size of the integration time-step with the magnitude of the zonal synoptic wind at 850 hPa. This feature is used to optimize the efficiency and resolution of the model for both average and extreme weather conditions.

A 3D finite-element grid [linear elements with 8 nodes] implemented in terrain-following coordinates describes the domain of application. The solution of the system of Eqs. (3.9) predicts the position of nodal air parcels at the beginning of the current time-step. The moist static energy and total water of the air parcel are then determined by interpolating among adjacent nodes. Moist static energy and total water are conservatively transported during the time interval of advection, but are updated with respect to water content whenever air parcels reach their lifting condensation level. At that height, or above, supersaturation values can be calculated from the distributions of h_M and T:

$$q_v = (h^{\xi}_{M} - c_p T - g z)/L \tag{3.10}$$

and

$$\Delta q_s = q_v - q_s \tag{3.11}$$

Formally, the replacement of q_s by q_s in Eq. (3.11) can be interpreted as an adjustment for the fact that a traveling air parcel, which is unsaturated at time (t-Δt) and is saturated at time t, must have undergone saturation somewhere in between its previous and current locations. The precipitable water contents above freezing level q_i and below freezing level q_l can be readily obtained from the continuity and condensation flux, respectively Eqs. (3.4) and (3.11) :

$$q_{i/l} = Q^{\xi} - q_v + \Delta q_s \tag{3.12}$$

Finally, the rain and snowfall rates are the following:

$$p_r = K_1 \, q_l \tag{3.13a}$$

$$p_s = K_2 \, q_i \tag{3.13b}$$

For the time scale typical of the triggering of orographic precipitation [< 1 hour], melting of snow as it travels through the atmosphere until it reaches the ground can be neglected (Browning and Collier 1989). The total water content and the moist static energy at the beginning of the new integration interval are obtained from continuity of total water:

$$Q = Q^{\xi} - p_r - p_s = q_s^{\star} + q_l \, (1 - K_1) + q_i \, (1 - K_2) \tag{3.14}$$

$$h_M = h_M^{\xi} - L \, \Delta q_s \tag{3.15}$$

3.2.3. Computational Aspects

The finite-element grid constructed for the Olympic mountains has a total of 2112 nodes and 1575 elements (Fig. 3.2), with six vertical layers corresponding to the 1000, 950, 900, 850, 500 and 250 hPa pressure levels. Figures 3.3a,b illustrate the quality of the topographic representation in the finite-element grids as compared to the "real" topography obtained from a 3 arc second [approximately 90 m] digital elevation map [DEM].

The horizontal resolution of the grid is about 10 km. A variable time-step ranging from about 10 minutes to one hour was used, depending on the 850 hPa wind speed. The model requires an average of less than 5 CPU seconds on an IBM RS6000 model 530 workstation to complete one time-step (one year of simulations takes approximately one hour of computer time).

3.3. Data Analysis

3.3.1 Initial and Boundary Conditions

For a given simulation, initial boundary conditions are established by computing a distribution of atmospheric moisture consistent with the daily values of precipitation observed at the beginning date. The results for the simulation of the excursion of the first weather feature through the application domain [typically 3 to 4 days] are ignored. By so doing, we eliminate the impact of initial conditions on the global analysis of results. This safeguards us against inconsistencies that might result from mistaken specification of initial conditions, such as the estimation of the spatial distributions of precipitation from a sparse number of point measurements [rain gages].

In the absence of detailed atmospheric circulation information for the study domain, we used radiosonde data for the specification of the boundary conditions. There are three radiosonde stations along the northwest coast of North America that might be relevant to this effort: two out-of-state stations, one in British-Columbia and the other in Oregon, and one in-state station at Quillayutte (see Fig. 3.4). These stations are positioned to observe the arrival of weather phenomena approaching respectively from north, south and west. Because precipitation along the northwestern coast of the U.S. is usually accompanied by westerly and southwesterly winds (Speers 1986), we selected Quillayutte as the source of boundary condition data for our simulations. This is generally adequate for the application to the Olympic Peninsula described here. However, during late spring and summer, when easterly or southeasterly winds occur, the use of Quillayutte as a reference station to impose boundary conditions is inappropriate. Because late spring and summer precipitation are responsible for less than 10 percent of the annual mean precipitation in the Olympic Peninsula, we simply omitted the precipitation simulated during those periods from our summary statistics.

During the study period [1967-1974], radiosondes were launched from the Quillayutte station four times daily, and during the six-hour intervals for which no new data are available we keep the boundary conditions constant. Clearly, during intense storms, when the model must operate at a time-step of a few minutes, significant discrepancies may occur at the level of instantaneous precipitation rates. From the point of view of long-term distributions of precipitation though, the spatial mass balance is altered only minimally by such episodes. Synoptic winds, temperature, and relative humidity data form the radiosonde data base. Temperature and relative humidity were used to establish the boundary conditions for moist static energy and total water contents. In addition, from the environmental and dew point temperature profiles we defined the distribution of the lifting condensation level for air parcels located at all nodes of the finite-element grid.

3.3.2 Wind Field

Wind, which is the major dynamic component of the model, governs the transport and distribution of energy over the spatial domain. Following previous investigators (Bell 1978, Gollvik 1984), we consider three distinct, though linearly related, wind field components: (a) a synoptic contribution linked to the general circulation of the atmosphere, (b) a surface contribution associated with the planetary boundary layer, (c) an orographically modulated wind field.

The large-scale horizontal wind field is extracted from radiosonde records at convenient heights [the atmospheric layers in the finite-element grid]. We expanded both zonal and meridional winds uniformly over the study area. This is clearly a crude approximation in the vicinity of baroclinic highs and lows, or, especially in the case of the Puget Sound, when mesoscale singularities such as convergence phenomena take place (Mass 1981). On the other hand, this approximation is well within the bounds commonly accepted in GCMs and meteorological forecasting models.

In an effort to attain a better representation of near-surface wind fields, a technique of optimal statistical analysis was applied for the spatial interpolation of wind data available at surface stations. Initially, clustering and principal correspondence analysis [PCA] according to Murtagh and Heck (1987) were used to investigate patterns of similarity among the available stations, with the objective of building a systematic classification scheme. This preliminary analysis was inconclusive. An alternative approach was then evaluated which identified the characteristics of winds with a probability of occurrence equal to or greater than 50 percent at each one of the locations [see Fig. 3.2 for wind station locations, and Fig. 3.5 for analysis of normalized results at Bellingham, Hoquiam, Olympia and Seattle-Tacoma airports]. Furthermore, our analysis showed that during fall and winter, the dominant daily wind direction was the same [within 45° octants of the wind rose] for more than 75 percent of the days on which rainfall occurred.

A further evaluation of temporal consistency among the surface stations and the 850 hPa wind at Quillayutte was also undertaken. This allowed us to determine the most frequent local surface winds seasonally. Spatial interpolation of the surface wind field was accomplished using the objective analysis approach of Thiebaux and Pedder (1987) as follows:

$$Y(x,y) = \sum_{i=1}^{n} \alpha_i(x,y)\,\chi_i \tag{3.16a}$$

and

$$\alpha_i\,(x,y) = \rho_i\,(x,y)\,\omega_i \tag{3.16b}$$

where χ and Y are respectively observed and estimated wind properties (intensity and direction), ρ_i is a correlation coefficient, and ω_i are weighting factors. The latter were established by mean square error analysis applied to the minimization of the difference Ψ between observed and estimated wind properties at the n reference stations:

$$\Psi = \{\sum_{i=1}^{n} [(\chi_i - Y_i)^2]\,/n\,\}^{1/2} \tag{3.16c}$$

The process was carried out independently for the zonal and longitudinal components of the wind vector. The velocity fields thus obtained were linearly interpolated from the surface up to the 850 hPa level, at which the surface influence was forced to vanish.

In summary, the first two components of the horizontal wind field are: the mean large-scale synoptic circulation and the surface-induced deviations. The vertical component is readily computed by integrating the continuity equation for incompressible fluids over the depth of the finite-element grid:

$$\frac{\partial u}{\partial x} + \frac{\partial v}{\partial y} = - \frac{\partial w^{\star}}{\partial z} \tag{3.17}$$

Finally, the third component of the wind field is introduced by estimating the effect of orography upon the generation or amplification of the vertical velocity field. Blocking effects and differential advection, deflection, and stratification are ignored by this formulation. The result of this approach is that the flow field appears as if the streamlines were molded to fit the topography. Therefore, the vertical velocity resulting from the deformation of the horizontal velocity fields can be described in terms of the partial orographic gradients z_x and z_y:

$$w_o = u\, z_x + v\, z_y \tag{3.18}$$

where,

$$z_x = \left(\frac{\partial z}{\partial x}\, dx\right) \left[\left(\frac{\partial z}{\partial x}\, dx\right)^2 + dx^2 \right]^{-1/2}$$

and

$$z_y = \left(\frac{\partial z}{\partial y}\, dy\right) \left[\left(\frac{\partial z}{\partial y}\, dy\right)^2 + dy^2 \right]^{-1/2}$$

The total wind vertical velocity at any point results from combining linearly the contributions from Eqs. (3.17) and (3.18):

$$w = w^{\star} + w_o \tag{3.19}$$

In fact, $w^{\star} \ll w_o$ [cm s^{-1} for synoptic scale motions versus m s^{-1} for the orographic updraft] and finally

$$w \approx w_o \tag{3.20}$$

3.3.3 Calibration and Verification Data

Daily rainfall records and catchment-average precipitation inferred from streamflow data were the main source of calibration, verification and validation data. In addition, snow-water equivalent measurements were also used in the validation phase.

As if to confirm the need for a model of orographic precipitation that would allow dynamic interpolation of scarce high elevation precipitation data. the Olympic Mountains are a typical example of scarcity and inadequate distribution of long-term rainfall gaging stations (Fig. 3.4). All but one of the stations are located at low elevation along the Strait of Juan de Fuca. Sappho is the highest station at 232 m above MSL. The distribution of precipitation stations is clearly inadequate for model validation purposes, because most of the significant precipitation events approach the mountains from the west and southwest, and the precipitation maximum is estimated to occur at about 1800-2000 m above MSL (Miller et al. 1973).

The situation does not improve much when high elevation snow course observations are included. Long-term snow data have been collected at only three snow course stations, Hurricane Ridge in the Elwha River basin, Cox Valley in the Morse Creek drainage basin and Deer Park in the Dungeness River basin, in addition to surveys of glaciers in the Mount Olympus area (Fig. 3.4). Snow water equivalent is measured manually on a monthly basis from January through May, at which time the snowmelt season is underway.

Calibration and verification of the model results with the available precipitation data were carried out in three steps: a) estimation of the characteristic rain and snow fall speeds, K_1 and K_2, by minimizing the mean square of the difference between model predictions and observations; b) comparing the areal distribution of precipitation computed by the model to estimated long-term precipitation distributions from a precipitation atlas (Miller et al. 1973), snow course data, and glacier location; and c) comparing annual mean areal rainfall over selected catchments delineated by the U.S. Geological Survey stream gages with mean catchment rainfall estimated from annual runoff inferred from stream gages. For this purpose, we concentrated on the Quinault, Hoh and Elwha river basins [areas of about 500-1000 km^2], which are located in the critical north, west and southwest slopes of the Olympics (Fig. 3.6a). In addition to the use of streamflow data, indirect measurements of precipitation including snow depth and snow water equivalent were used for mass balance control and long-term seasonal validation of model performance.

Storm predictability was analyzed with respect to interstorm arrival times, time to peak, peak magnitude and duration. A major storm at the end of

January 1967 was investigated in detail, and was used to evaluate the model's ability to simulate extreme conditions.

3.4. Results

Model calibration was carried out for low elevations by using precipitation data collected at the eight low elevation precipitation stations shown in Fig. 3.4, and for high elevations by matching seasonal and annual precipitation inferred from runoff for the Hoh, Elwha and Quinault river basins, and snow course observations at Hurricane Ridge, Cox Valley and Deer Park. Relevant statistical properties of the data are summarized in Table 3.1. Daily and accumulated precipitation for 1967 were used for initial calibration. The streamflow data were used to investigate the performance of the model for high elevations. Point precipitation, catchment average precipitation, and snow course observations for the period 1968 to 1974 were subsequently used for model verification. When the model was used in predictive mode, we placed special emphasis on the verification of long-term seasonal means at all stations for both precipitation and runoff, and the evaluation of storm properties [interarrival times, duration, and precipitation maxima].

3.4.1 Calibration

The initial phase of the calibration process was aimed at finding an adequate description of the spatial variability of the rate of extraction of atmospheric water at all times [e.g. a characteristic distribution of hydrometeor scavenging over the study domain]. A major objective of this phase of the work was to accomplish calibration without compromising the applicability of the model to special atmospheric conditions, or regional features. Hence, a methodology was developed that is based on rules that will be consistent with future applications of the model to other regions. The approach relies exclusively on topography, and synoptic temperature and humidity fields.

Based on the results from past studies of orographic distribution of precipitation, we tentatively defined the following master relationship among surface elevation h, local updraft w_l, and relative position in a mountain slope:

$$K_l = \beta_l \, w_l \tag{3.21}$$

and

$$\beta_l = \beta_l^m \, z \, / \, z_{ref} \tag{3.22}$$

where β is the orographic enhancement function, the subscript l refers to the atmospheric layer, β^m is the maximum orographic enhancement and z_{ref} is the elevation at which maximum precipitation is estimated to occur. For a given calibration period, the optimization process consists of searching for values of β_l^m, which result in the best simulations of fall, winter, and spring precipitation. Because of the high frequency of easterly winds during summer, and because summer precipitation is mainly driven by convective activity associated with convergence originated by mountain-valley gradients of radiative forcing, which is not represented in the model, no attempt was made to calibrate for summer conditions. Nonetheless, the results obtained describe the observed rainfall well for most of the calibration and verification periods (including summer), mainly due to the prevalence of dry weather during late spring and summer (Fig. 3.7).

Equation (3.22) suggests, consistent with the model dynamics, that the local elevation can strongly affect the magnitude and evolution of precipitation. Also, mountain blocking of synoptic circulation may have significant impact upon the spatial distribution of moisture availability in the surrounding atmosphere (PierreHumbert 1984). Despite continuous improvements in the resolution of atmospheric models, aliasing of low elevations cannot be avoided in discrete representations of the Earth's orography: for instance, a regional model such as the one described by Giorgi and Bates (1989), which has a resolution of 60 km, fails to represent the Olympic Mountains at all. While our model is of considerably finer resolution [< 10 km], the effect of elevation aliasing is still significant as shown in Table 3.2, where actual elevation data at individual precipitation stations is compared with the gridded elevations of our finite-element mesh. To counteract this effect, we developed a spatial filtering scheme through which a 3D correction surface is fitted to the application domain. Local slope I, distance to the oceanic boundaries D, and aliased elevations Z are combined linearly to define the mapping function F(I, D, Z):

$$F(I, D, Z) = a_1 + a_2 I + a_3 D + a_4 Z \tag{3.23}$$

The weighting factors a_i are computed by matching selected points: natural choices are the precipitation and streamflow gages, or snow course stations.

The use of low elevation precipitation data in this study results from the lack of alternative data sources [high elevation precipitation gages]. Besides the orographic disparity associated with topographic aliasing, other important effects inherent to mesoscale coastal phenomena such as land and sea breeze, which are neglected in this model, may interfere with calibration. Scaling arguments presented by Rotunno (1983) indicated that, where the Coriolis coefficient f is larger than the diurnal frequency of radiative heating and cooling ω_d, such circulations are relevant over a distance L from the coastline which can be estimated given a characteristic Brunt-Väisälä frequency N and the vertical length scale of heating H:

$$L_w = N H / (f^2 - \omega_d{}^2)^{\frac{1}{2}} \tag{3.24}$$

In the case of the Olympic Mountains, the length L_w extends about 30 km from the coast for average conditions. This implies that all the precipitation gages used in this application are within the area of influence of land and sea breeze phenomena. We resorted to synoptic information on relative humidity and temperature fields to establish a set of three adjusting filters applicable to dry and wet, and cool and hot weather conditions in the Olympic Peninsula. These filters have the structure presented by Eq. (3.25), where μ_x and $x_{\min}$ are respectively the mean and the minimum observed precipitation at the individual stations, and x is an instantaneous model result:

$$F(\mu_x, x_{\min}, x) = b_1 \mu_x + b_2 x_{\min} + b_3 x \tag{3.25}$$

The weighting coefficients b_i were estimated for a variety of scenarios characterized by dew point temperatures T_D above and below 3°C, and the number of days with below freezing-level temperatures.

For this case study, the adjustment parameter η was made equal to 0.95 and the orographic enhancement parameter β_l^m assumed values equal to 1.5 and

1.0, for T_D above and below 3°C respectively. Major obstacles to the calibration process were encountered for days during which northerly frontal systems or easterly winds were present. In fact, the problems found are not a consequence of the weather features per se, but result from the poor description of the boundary conditions in such occasions.

Consider first the case of frontal systems. The arrival and evolution of a frontal system in the third week of January, 1967 is stylized in Fig. 3.8, and will be used to illustrate the discussion. Radiosondes launched from Quillayutte, which provide point measurements at selected atmospheric heights, fail to provide information on the thermodynamic [temperature and humidity] gradients, and wind field discontinuities which characterize the presence of a front. From our example, in the first day the radiosonde does not "see" the frontal system through a large extent of the lower troposphere. Hence, a delay is expected to be observed in the comparison between data and storm arrival times at the northern stations, which the frontal system has already reached. On the other hand, in the second day, the reverse is true for the south and easterly areas of the study domain, where the front has yet to arrive. This deficiency in the timing of the specified boundary conditions translates quantitatively into phase errors of model predicted storm arrivals. However, another difficulty may arise with respect to the magnitude of the storm peak: precipitation will be lower than expected at the northern stations in the first day, and higher at the south and easterly stations in the second day. In practice, this may result in the amplification of low precipitation values and reduction of storm peaks for locations in front of, and behind the frontal system respectively. In this context, the use of radiosonde data to impose boundary conditions should be restricted to the area of influence of the radiosonde only, and modeling of large areas necessarily implies one of the following: (a) the availability of a large number of radiosonde stations, ideally one at or in the vicinity of each boundary node in the numerical grid; (b) the coupling of a transport model such as the one depicted in this paper with a regional circulation model, whose role is to interpolate sparse information through physical operators.

In the case of easterly winds, the most important issue relates to the nature of the boundary conditions: for northerly, westerly, or southerly winds, the boundary conditions perform as forcings that activate and induce transport; for easterly winds, the boundary conditions constitute anchor points for verification of the transport solution. This type of boundary condition has the potential to induce artificial reflection, which may lead to the generation of spurious waves in the transport solution near the boundaries. This problem can be quite naturally avoided if the grid is extended significantly outside of the area of interest. However, computational considerations preclude arbitrary expansion of the spatial domain without affecting model resolution. For this reason, an alternative approach of simply replacing the spatial distribution of precipitation inferred from the statistics of historical observations on the limited days when the synoptic winds were easterly was used. We applied the same statistical objective analysis scheme as was used for estimation of surface wind fields to determine the precipitation distribution on days of easterly winds. Normalized distributions of precipitation, such as the one depicted in Fig. 3.9 for winter conditions, were found by applying optimal objective analysis with a spatial correlation field [$\rho'(x,y) \equiv \rho(x,y)$ in Eq. (3.16b)] modulated with the surface orographic enhancement function β_l described in Eq. (22):

$$\rho'(x,y) = \beta_l \exp[(x^2 + y^2)^{-1/2} / x_L] \tag{3.26}$$

where x_L is a correlation length, which we took to be 200 km. The precipitation stations are far enough apart that the inter-station correlations are relatively small [less than 0.3], which is a necessary condition for application of optimal spatial objective analysis.

Daily and accumulated precipitation values were used to calibrate the model at low elevations, while the catchment water balance involving streamflow R, total precipitation P, and evapotranspiration fluxes E, was used to infer model performance at higher elevations:

$$P - R - E = \Delta S \tag{3.27}$$

where ΔS is the change in catchment water storage [as snow water equivalent or soil moisture storage]. On an annual basis, especially using the water year

October-September, ΔS can be taken as zero.

The estimation of evapotranspiration is a difficult problem: adequate meteorological data are available only at Quillayutte [elevation 60 m] in the Olympic Peninsula. However, there is a meteorological station at Stampede Pass [elevation 1200 m] in the Cascade Mountains, which can be used to approximate evapotranspiration at roughly similar elevations in the Olympic Mountains. We found that, for a typical hydrological year [1967], a Bowen ratio of 0.9 [typical of the latitude and climate of the Olympic mountains], potential evapotranspiration calculated according to Arya (1988) was approximately 650 mm at Quillayutte, and 900 mm at Stampede Pass. Our main goal was to verify the water balances of selected river basins on an annual basis. For this purpose, we assumed a value of 650 mm for the actual evapotranspiration, with uniform spatial and temporal distributions during late Spring and Summer.

3.4.2 Validation and Storm Forecast

Figures 3.10a through 3.10h compare the monthly mean total precipitation simulated by the model and the observed station values. The annual distribution of monthly mean precipitation maxima in the Olympic Peninsula as compared to the observed monthly mean precipitation at Forks is shown in Fig. 3.11, which illustrates the enhancement effect of precipitation by orography, as well as the consistency of model simulations with respect to the regional seasonality. Table 3.3 provides a quantitative evaluation of the performance of the model not only for the simulation of long-term annual means, but also for seasonal values, e.g. spring, and winter and fall combined. There is good agreement between observed and simulated data, suggesting that the anti-aliasing and the post-processing filters are consistent with the dynamics of the predominant physical processes in the low regions.

Table 3.4 contains information relative to frequency, duration and magnitude of storms at the four stations located farthest from the coast: Forks and Sappho in the west side, and Elwha and Lake Sutherland in the north side. The errors are relevant for the two west side stations, both for storm timing and peak values. Some of the errors are attributable to the convention used for specification of storm events: precipitation below 0.5 mm/day was considered negligible. This threshold appeared to be adequate for the northern stations, but not in the case of western stations, for which the simulated time-series of storm occurrence are characterized by long tails with very low precipitation intensities. Also, the post-processing filter did not perform well with respect to the peak storm precipitation at Forks and Sappho. We show in Fig. 3.12 the time evolution of precipitation during the winter season of 1967, for both observed and simulated data. In particular, analysis of the period corresponding to the storm of the 19^{th} of January [Julian day 19], which is referred to in the Storm Data and Unusual Weather Phenomena (US Weather Bureau 1967), indicates that the storm peak is under-predicted by the model, while the phase error is about one day for these two stations. The peak error for this large storm is somewhat typical: in general, the model tends to attenuate large storms, and magnify the more frequent, lesser ones. Phase errors are mainly related to the identification of approaching frontal systems as discussed above.

The most important goal of the validation process was to investigate the distribution of precipitation in the high mountainous areas, for which both snow course and streamflow records are surrogates in an integrated areal sense. The results for snow course stations are summarized in Table 3.5. As is apparent from Fig. 3.4 the three snow course stations are located in the Northwest lee side of the mountains, where the rainshadow effect is significant. Although no direct measurements were available for the glacier regions during the simulation period, it can be seen that the location of precipitation peaks in model simulations coincides with the locations of the perennial glaciers.

The three catchments used in this study were identified in the numerical grid by the elements from which water drains towards the outlet streamflow station (Fig. 3.6). The basin areas match the USGS estimated areas within 5 percent for the Hoh and Elwha river basins, and 10 percent for the Quinault river basin. The total precipitation P over a watershed was evaluated as follows:

$$\mathrm{P} = \int_T \left\{ \sum_{i=1}^{n} \int_{\Omega_e} \mathrm{p(x,y,t)\ dx\ dy} \right\} \mathrm{dt} \tag{3.28}$$

where n is the number of finite-elements of area Ω_e within the watershed, and T is the integration period. This analysis was carried out in a seasonal basis, and the results are presented in Table 3.6. In this case, the seasonal errors are consistent with the seasonal snow melting and accumulation: the apparent winter errors are positive, and in summer [results not shown] the apparent errors are negative. Neither snowmelt nor snow accumulation, ΔS in Eq. (3.27), were accounted for in our calculations. Therefore phase errors such as the ones identified at the end of winter are unavoidable, and it is best to focus on the annual errors. Years with large errors, e.g. well above 20 percent, are mostly associated with atmospheric conditions characterized by abnormally low dew point temperatures, for which the model exhibits less sensitivity as compared to conditions characterized by normal or high dew point temperatures. This is the case for the dry winter seasons of 1968, 1971, and 1972. The errors are magnified for the Hoh and Quinault river basins, because the hydrological behavior of these basins is strongly regulated by what happens in the alpine areas. However, the observed annual totals are matched by model simulations with an error of less than 15 percent. This close agreement is promising for applications of the model to hydroclimatological studies.

Figures 3.13a through 3.13e show the mean monthly spatial distribution of precipitation for the months of January, March, May, November and December, as obtained from the eight years of model simulation. The orographic effect of the Olympic Mountains upon the regional distribution of precipitation is reflected in the dramatic increase of precipitation with elevation, which can be as much as 200 percent at the highest elevations. Because the dominant direction of storm approach in the winter months is from the southwest, the orographic enhancement on the upwind side of the mountains is well illustrated by Figs. 3.13a,b and 3.13d,e [January, March, November and December]: some low-lying ridge crests toward the southwest receive nearly as much precipitation on average as the upwind side of the highest peaks. During the spring months, storm directions are more variable [as reflected by Fig. 3.13c for May] but the southwesterly dominance begins to be reestablished in the late fall [see Fig. 3.13d for November].

Inter-annual variability of the spatial distribution of precipitation is illustrated by Figs. 3.14a and 3.14b, which allows evaluation of such variability through comparison of the precipitation distribution during February of 1967 with the same month of 1969. The "patchy" appearance of the spatial distribution of precipitation during February of 1969, indicates that storm activity was significantly larger during that period than during the corresponding month of 1967, which can be confirmed through the atmospheric records. An important aspect of these results is that, although the spatial distribution of precipitation is distinct for each of the hydrological years, the location of the precipitation maxima remains the same.

3.5. Discussion

An earlier approach to modeling orographic precipitation (Barros and Lettenmaier, 1990) consisted of simulating Eulerian transport of vapor and liquid water. The thermodynamic mechanisms were implemented according to penetrative parcel theory modified by entrainment and precipitation, the rate coefficients for which were estimated through calibration. The model, which is based on a fully implicit scheme, was abandoned due to excessive computational costs. The model formulation described in this paper is close to the convective adjustment scheme described by Cunnington and Mitchell (1990), who suggested that, in climate models, such a scheme transports heat and moisture less efficiently than penetrative parcel schemes. We experienced the same results with respect to the production of precipitation in mountainous regions.

We conducted sensitivity analysis to evaluate the importance of the model time-step. Because of the interactions between synoptic circulation and local orographic features, we concluded that the time-step should be allowed to vary spatially. This is illustrated qualitatively in Fig. 3.15a: larger errors are observed for lower frequency storms and for easterly winds, which both reflect inadequacy of the boundary conditions used as well as gross representation of atmospheric dynamics. At a given station, the error surface expressed as a function of local slope and time-step has a bell shape tilted towards the origin (Fig. 3.15b). At the origin, the error equals the interpolation error, which decreases as the time-step increases up to the point when scaling error, intrinsic to the simulation of physical processes, take over and increase theoretically to infinity.

3.6. Summary

We have developed, implemented and applied a 4D Lagrangian model to simulate orographically induced precipitation. The model is designed to allow estimation of the long-term hydroclimatology of large regions characterized by complex, inaccessible terrain, and to reproduce the properties of individual storm events. It was tested for the Olympic Mountains, with success. We believe that coupling of the model to a spatially distributed surface energy model is desirable to improve the verification of the hydrological balance throughout the spatial domain, and this is an improvement we intend to pursue.

Subgrid scale processes such as blocking, thermally forced circulations, lee side cyclogenesis, and lee waves, are not considered in the present form of the model. Hence, although long-term properties of the spatial distribution of precipitation are preserved in model simulations, local effects of mesoscale and field scale circulation phenomena cannot be reproduced. Assessment of climate change at the catchment scale, and the forecasting of extreme events are among the promising fields for the use and further development of the model.

Table 3.1 a) Mean and standard deviation of monthly precipitation (in mm): winter and fall 1967-74. (see Fig. 3.4a for station locations) [Stdv - Standard deviation]

	Stations							
	1	2	3	4	5	6	7	8
January								
Mean	325.1	256.5	254.0	383.5	386.1	63.5	119.4	475.0
Stdv	124.5	129.5	121.9	177.8	177.8	33.0	53.3	188.0
February								
Mean	215.9	175.3	157.5	322.6	307.3	30.5	63.5	350.5
Stdv	124.5	81.3	78.7	172.7	119.4	12.7	30.5	170.2
March								
Mean	195.6	165.1	139.7	266.7	241.3	35.6	58.4	297.2
Stdv	81.3	68.6	55.9	99.1	83.8	15.2	22.9	94.0
October								
Mean	218.4	167.6	182.9	309.9	271.8	43.2	73.7	350.5
Stdv	106.7	81.3	94.0	114.3	106.7	25.4	43.2	150.0
November								
Mean	297.2	231.1	223.5	363.2	348.0	53.3	94.0	429.3
Stdv	73.7	83.8	81.0	83.8	99.1	22.9	35.6	114.3
December								
Mean	330.2	215.9	223.5	452.1	348.0	50.8	91.4	469.9
Stdv	81.3	58.4	61.0	91.4	58.4	15.2	17.8	160.0

Table 3.1 b) Mean and standard deviation of annual streamflow (m^3 s^{-1}) 1967-74. [Stdv - Standard deviation]

River Basin	Mean	Stdv
Elwha	40	7
Hoh	61	8
Quinault	9	2

Table 3.2 Effect of elevation aliasing at precipitation stations.

Stations	Actual Elevation (m)	Model Elevation (m)
Neah Bay	3.0	175.0
Clallam Bay	9.0	238.0
Forks	107.0	192.0
Sappho	232.0	530.0
Elwha	110.0	584.0
Lake Sutherland	174.0	337.0
Sequim	55.0	151.0
Port Angeles	12.0	126.0

Table 3.3 Percentage errors in simulated monthly precipitation for years 1967-74. [expressed as (simulated-observed)/simulated]

Stations	Spring	Winter-Fall	Annual
Clallam Bay	+17.5%	+3.5%	+5.5%
Elwha	+12.5%	-1%	-1%
Lake Sutherland	-4%	+5%	0
Neah Bay	-11%	+3%	-2%
Sappho	-10%	+8%	-9%
Sequim	-9%	+7%	-3%
Port Angeles	+10%	+8%	+4%
Forks	+16%	+7%	+5%

Table 3.4 Observed and simulated mean storm properties, 1967-74.
[MNS - mean number of storms; MIAT - mean interarrival times (days); MD - mean duration (days); MSP - mean storm precipitation (mm)]

Stations	Winter				Fall			
	MNS	MIAT	MD	MSP	MNS	MIAT	MD	MSP
Sappho								
Observed	18	1.8	3.1	57.9	18	2.1	3.0	39.2
Simulated	18	2.4	2.9	57.3	21	2.1	2.3	29.6
Forks								
Observed	18	1.6	3.1	72.0	18	2.0	2.7	48.5
Simulated	21	1.6	2.6	66.5	21	1.6	2.7	43.1
Elwha								
Observed	15	2.8	3.6	43.2	18	2.1	2.8	24.4
Simulated	18	2.3	2.8	36.5	21	2.1	2.3	17.2
Lake Sutherland								
Observed	12	2.9	5.0	53.1	15	2.4	3.3	30.6
Simulated	12	2.7	5.0	61.0	15	2.4	3.4	30.8

Table 3.5 Percentage errors in accumulated precipitation as estimated at high elevation snow course stations January-May: (a) 1967: (b) 1968; (c) January-May 1969. [expressed as (simulated-observed)/observed]

Stations		Observations (mm)	Model Results (mm)	Error
Cox Valley				
	(a)	---	---	---
	(b)	171	155	-10%
	(c)	357	337	-6%
Deer Park				
	(a)	360	347	-3.6%
	(b)	181	179	-1.4%
	(c)	186	256	+37.5%
Hurricane Ridge				
	(a)	422	458	+8.6%
	(b)	211	181	+16.7%
	(c)	363	352	-2.8%

Table 3.6 Percentage errors in simulated precipitation for the Hoh, Quinault, and Elwha river basins. [expressed as (simulated-observed)/observed]

	Hoh		Quinault		Elwha	
	Winter	Annual	Winter	Annual	Winter	Annual
1967	+15%	+3%	+20%	+12%	+5%	-21%
1968	+45%	+10%	+46%	+15%	-7%	0
1969	+3%	+5%	+5%	+1%	-28%	-9%
1970	+30%	+4%	+33%	+21%	-8%	-19%
1971	+57%	+13%	+7%	+6%	+4%	-8%
1972	+77%	+2%	+27%	+4%	-13%	-1%
1973	+28%	+9%	-16%	+7%	-27%	-5%
MEAN	+36%	+7%	+25%	+9.5%	-11%	-13.5%

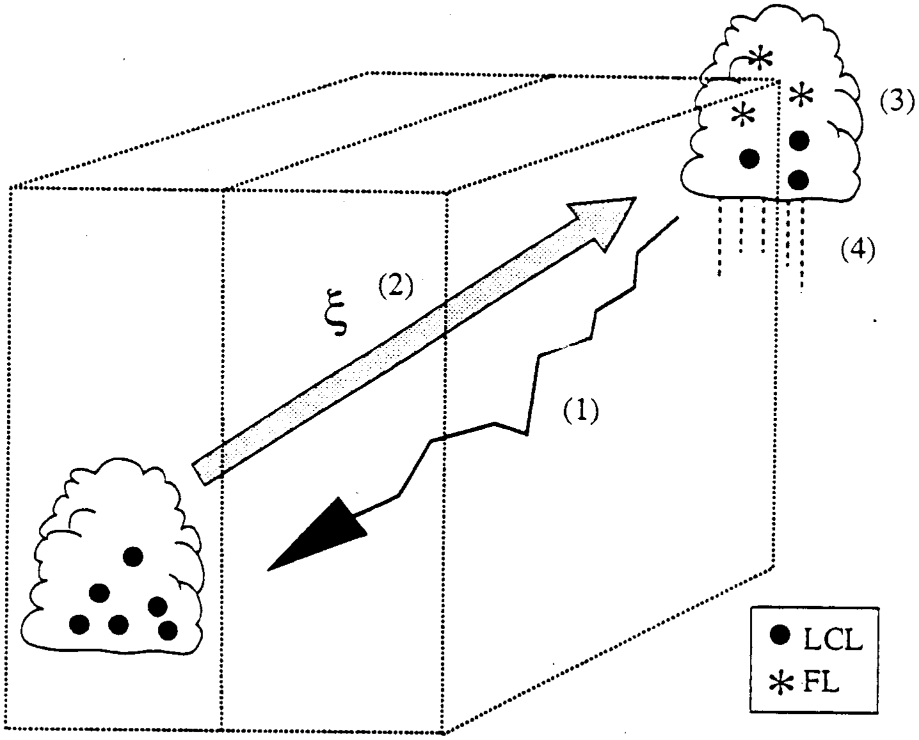

Figure 3.1 Conceptual description of the model: (1) - backwards tracking of an air parcel; (2) conservative transport; (3) cloud formation and evolution; (4) precipitation.
(LCL - Lifting Condensation Level; FL - Freezing Level)

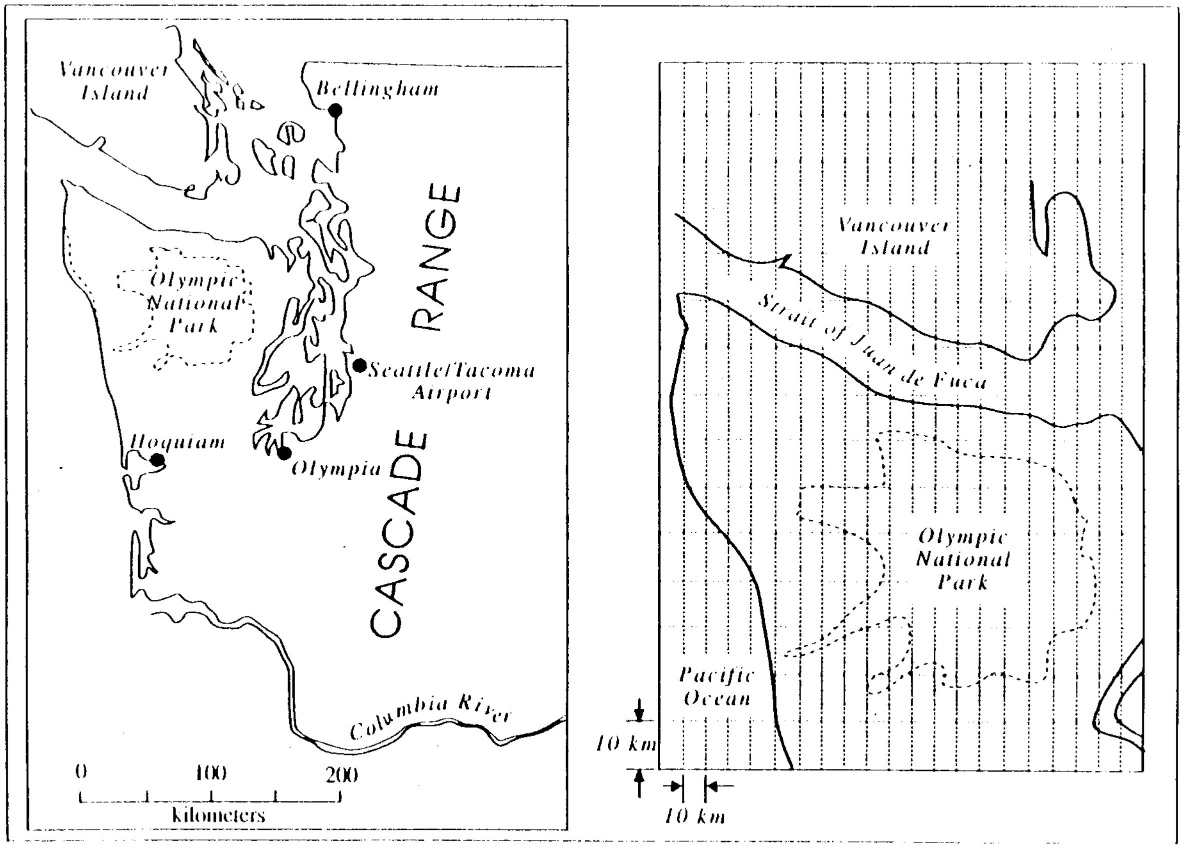

Figure 3.2 Map of the Olympic Mountains and surroundings, and finite-element grid over the Olympic Peninsula area.

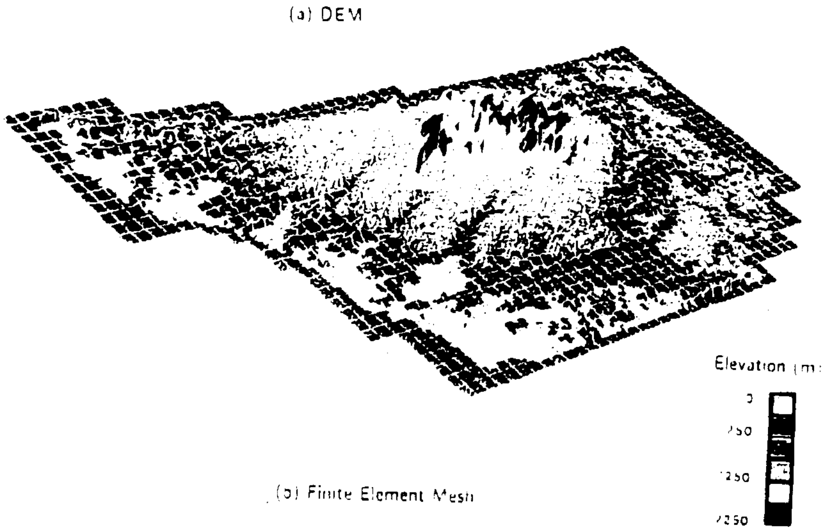

(a) DEM

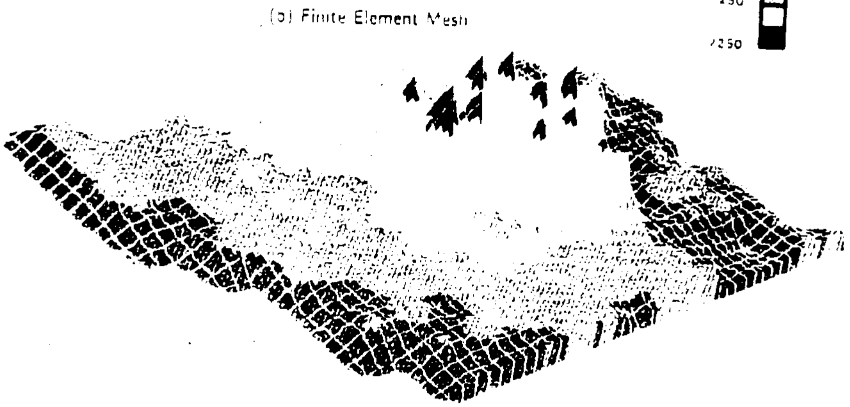

(b) Finite Element Mesh

Figure 3.3. a) DEM representation of the Olympic Mountains (3 arc second resolution interpolated to 2 km grid);
b) model representation of the Olympic Mountains orography (10 km resolution interpolated to 2 km grid).

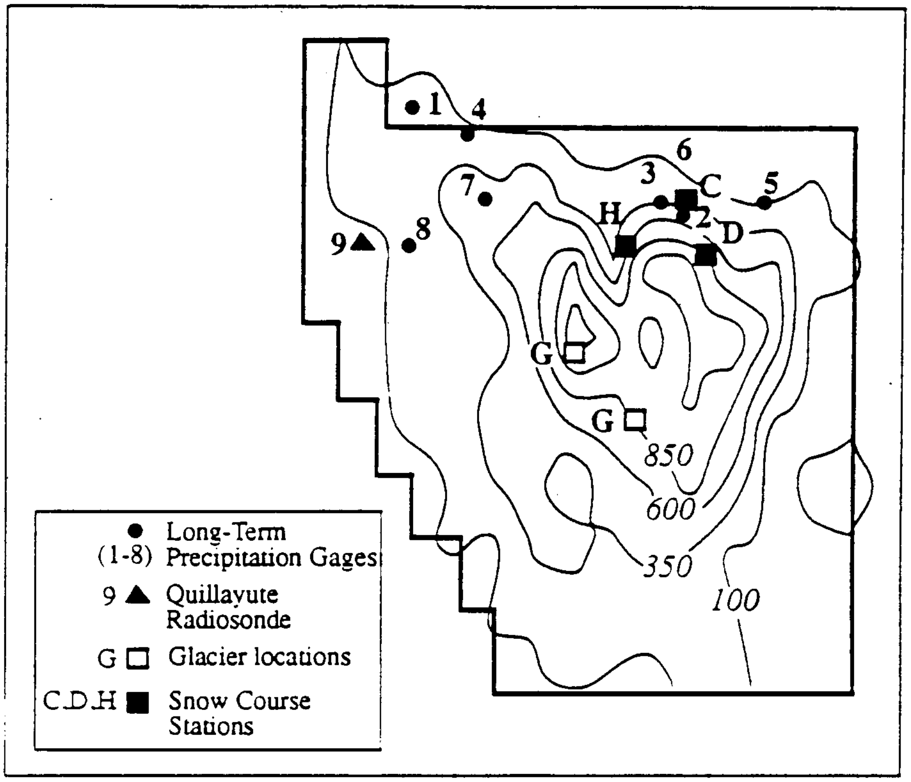

Figure 3.4 Rainfall gages, radiosonde and snow course stations, and glacier locations in the Olympic Peninsula. (1-Neah Bay; 2-Elwha; 3-Lake Sutherland; 4-Clallam Bay; 5-Sequim; 6-Port Angeles; 7-Sappho; 8-Forks; 9-Quillayutte Radiosonde; G-prominent glaciers; H-Hurricane Ridge; C-Cox Valley; D-Deer Park)

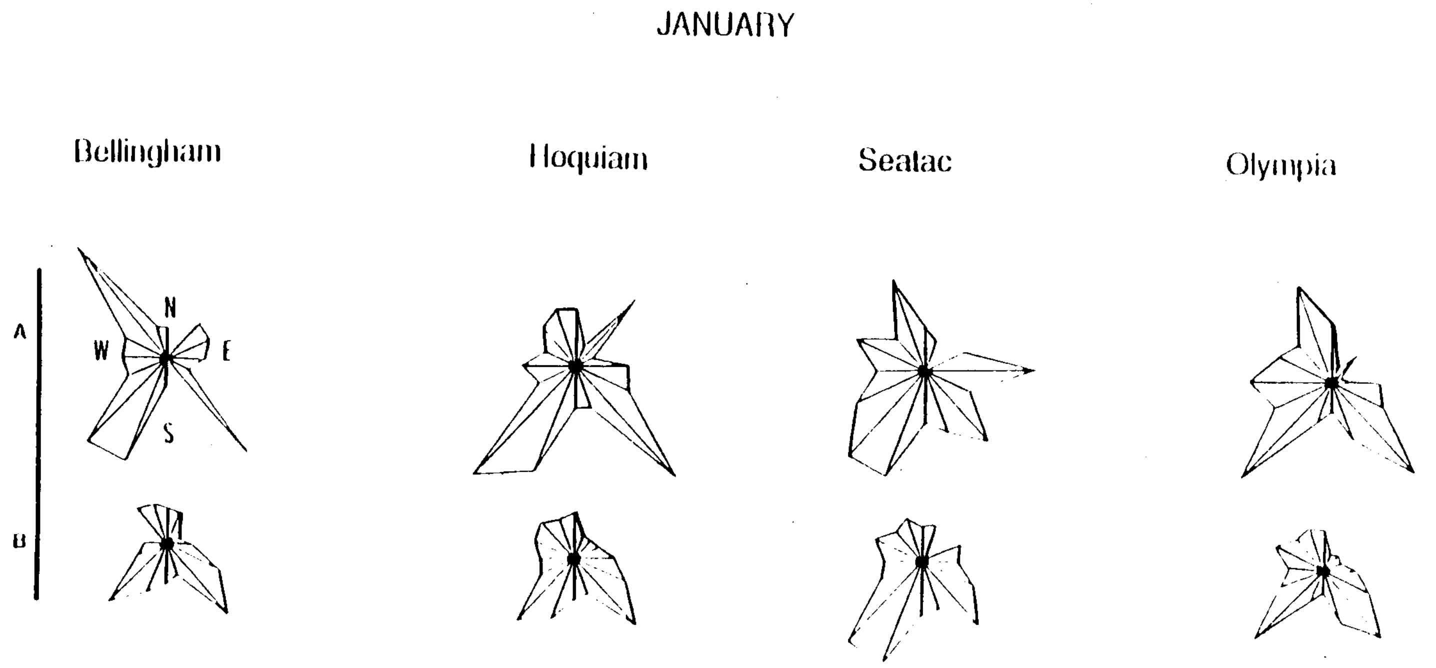

Figure 3.5 Characteristic surface winds with frequencies equal or greater than 50 percent in rainy days, during January, at selected Olympic Peninsula stations.
(A- normalized wind intensity; B-wind direction)

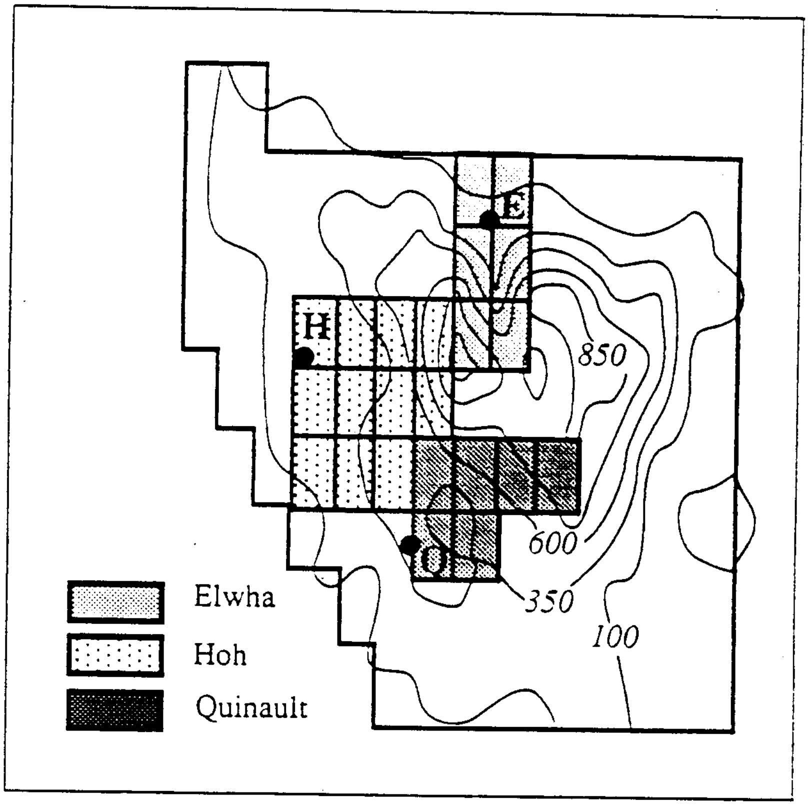

Figure 3.6 Long-term streamflow gages and approximate delineation of the area of influence of the Elwha (E), Quinault (Q), and Hoh (H) river basins.

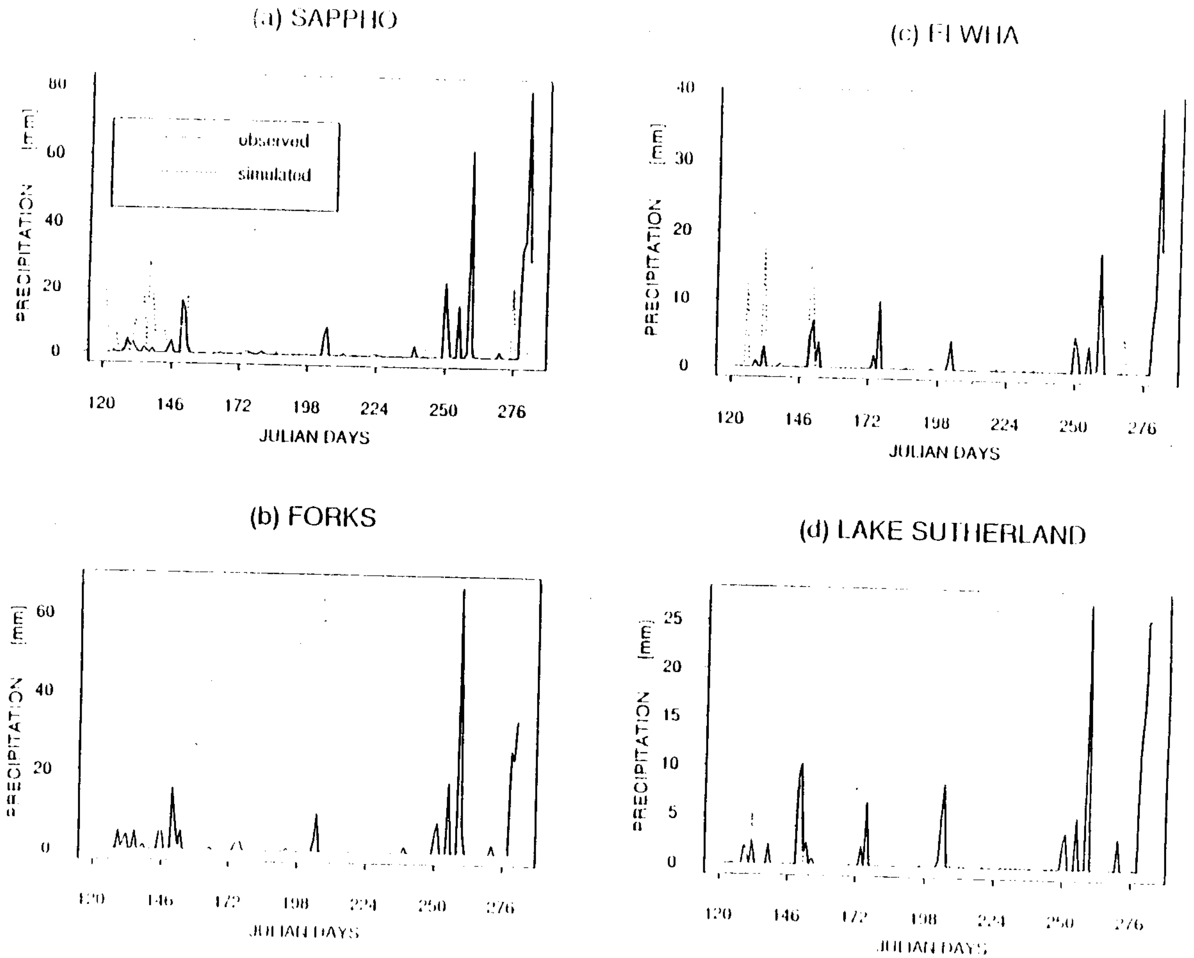

Figure 3.7 Time-series of summertime observed and simulated precipitation at a) Sappho; b) Forks; c) Elwha; d) Lake Sutherland. (_ observed : _ _ _ simulated)

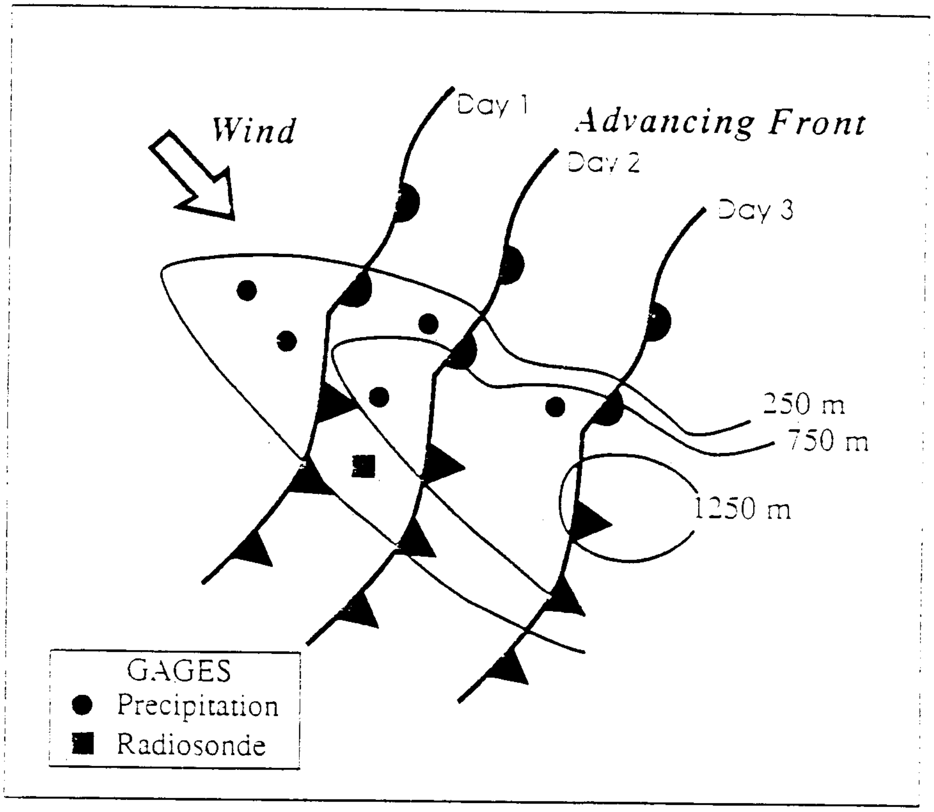

Figure 3.8 Conceptual tracking of the progress of a northerly front as it approaches, crosses and leaves the Olympic Peninsula, based on synoptic charts for the 3rd week of January 1967.

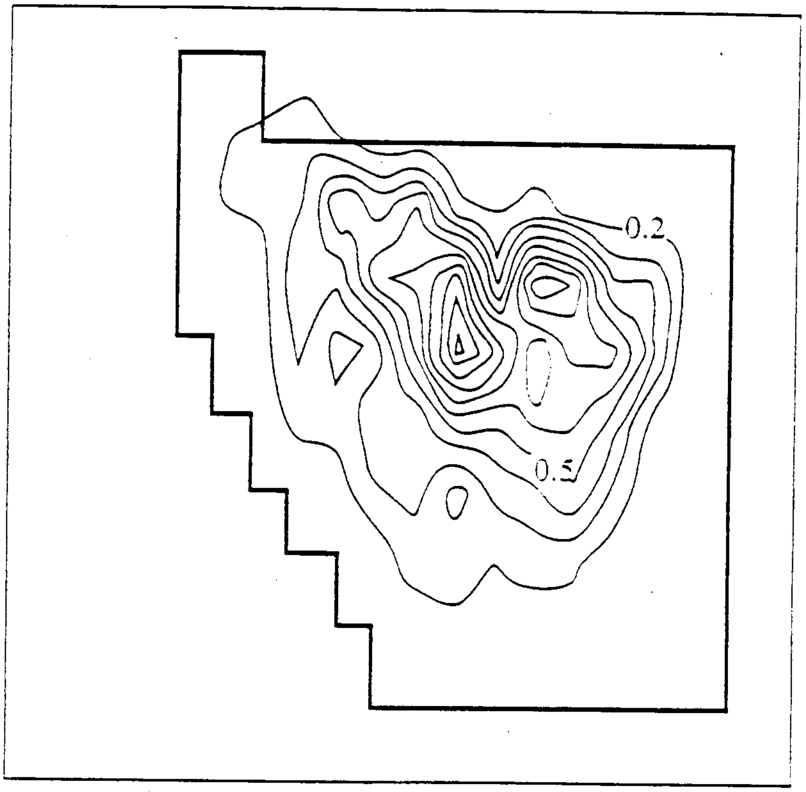

Figure 3.9 Normalized statistical distributions of orographic enhancement for winter conditions based on spatial objective analysis of rainfall data. (base line - 0.2; contour interval - 0.2)

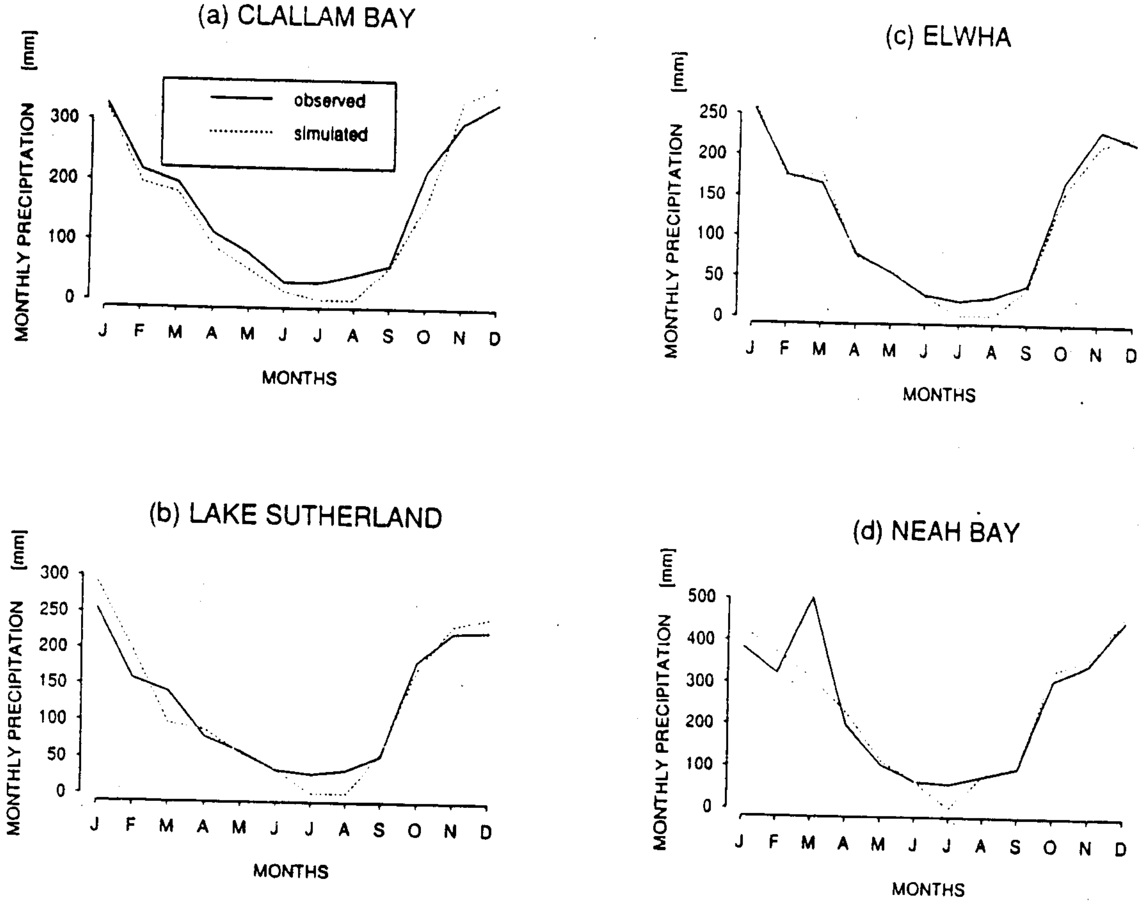

Figure 3.10 Comparison of observed and simulated monthly mean precipitation at the location of the eight precipitation gages shown in Fig. (4) for the study period (1967-1974): a) Clallam Bay; b) Lake Sutherland; c) Elwha; d) Neah Bay.

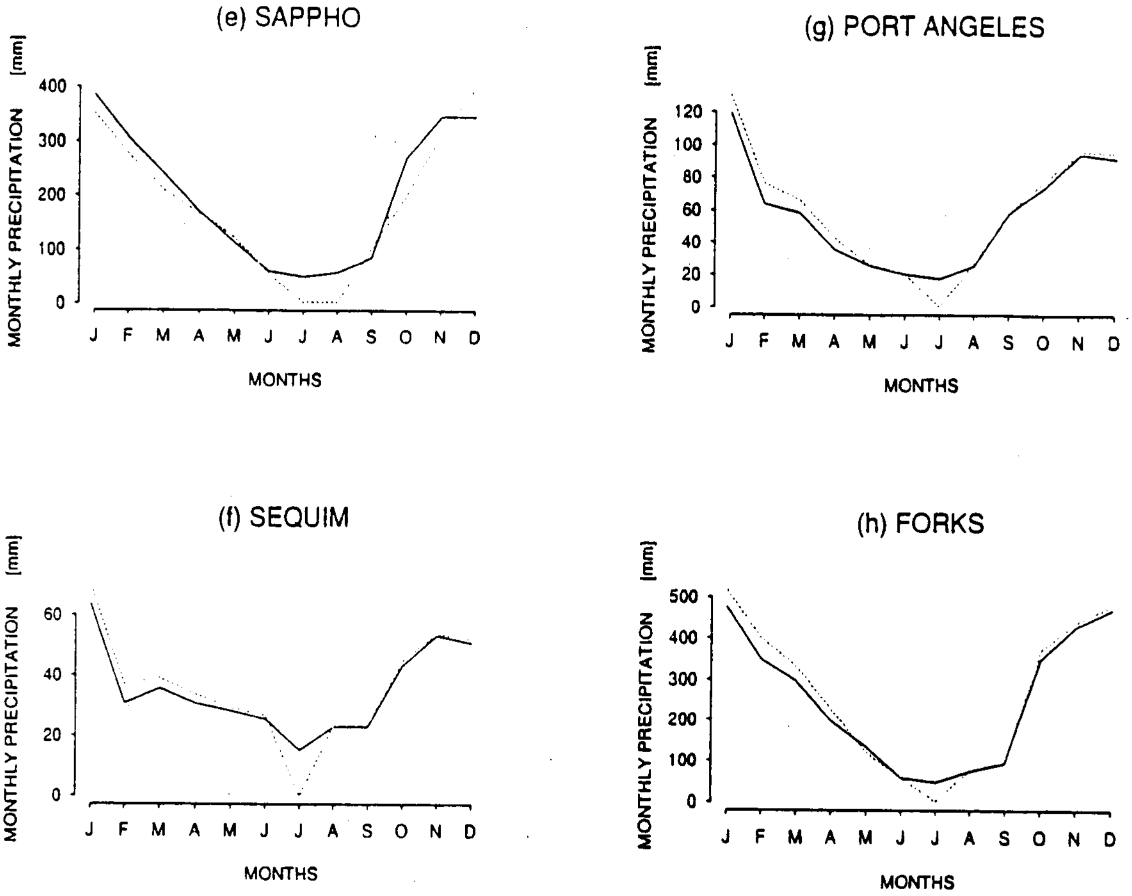

Figure 3.10 (continued) Comparison of observed and simulated monthly mean precipitation at the location of the eight precipitation gages shown in Fig. (4) for the study period (1967-1974): e) Sappho; f) Port Angeles; g) Sequim; h) Forks.

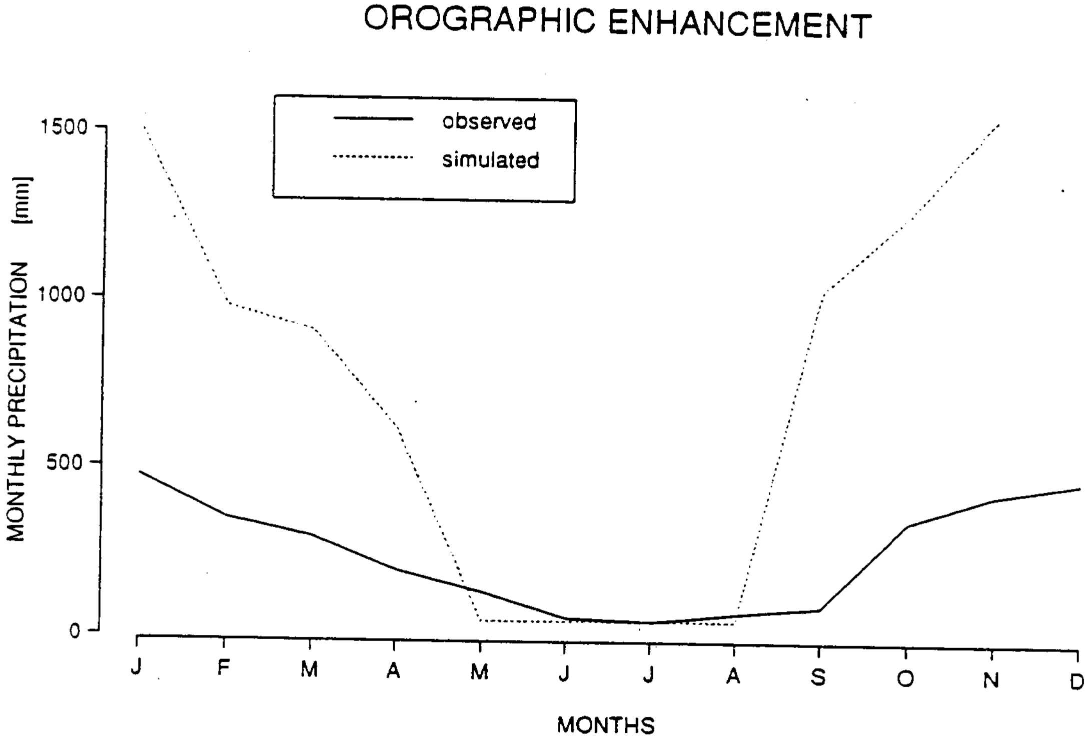

Figure 3.11 Mean monthly precipitation simulated by the model at the glacier locations as compared with the values observed in the coastal lowlands (Forks).

(a) FORKS

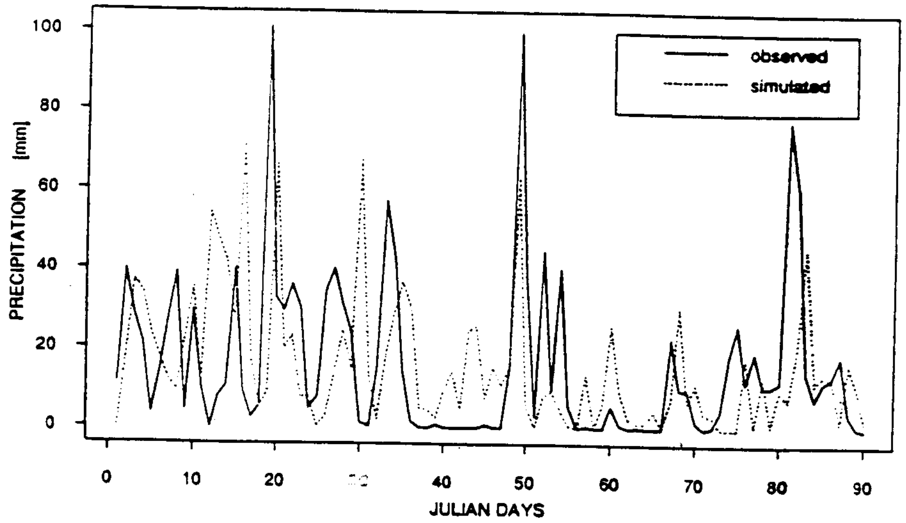

(b) SAPPHO

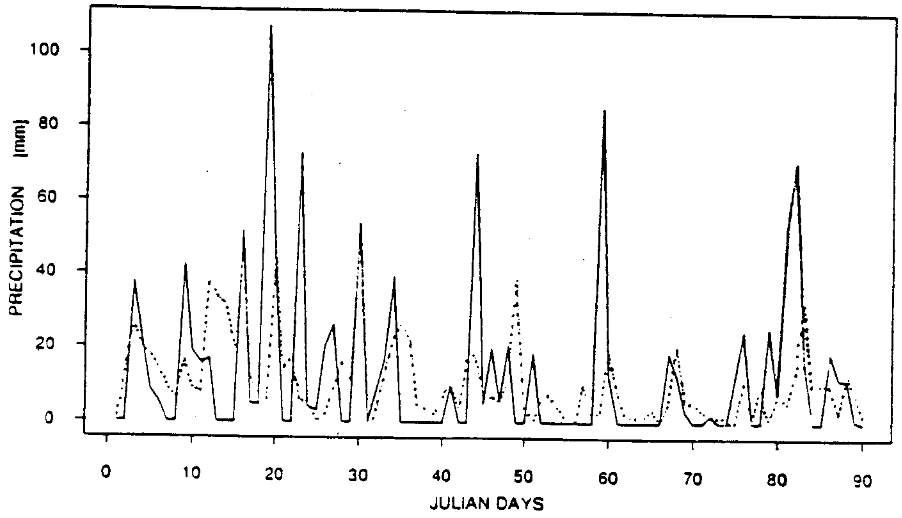

Figure 3.12 Comparison of simulated and observed daily precipitation at Forks (a) and Sappho (b) during winter of 1967.
(_ observed ; ___ simulated)

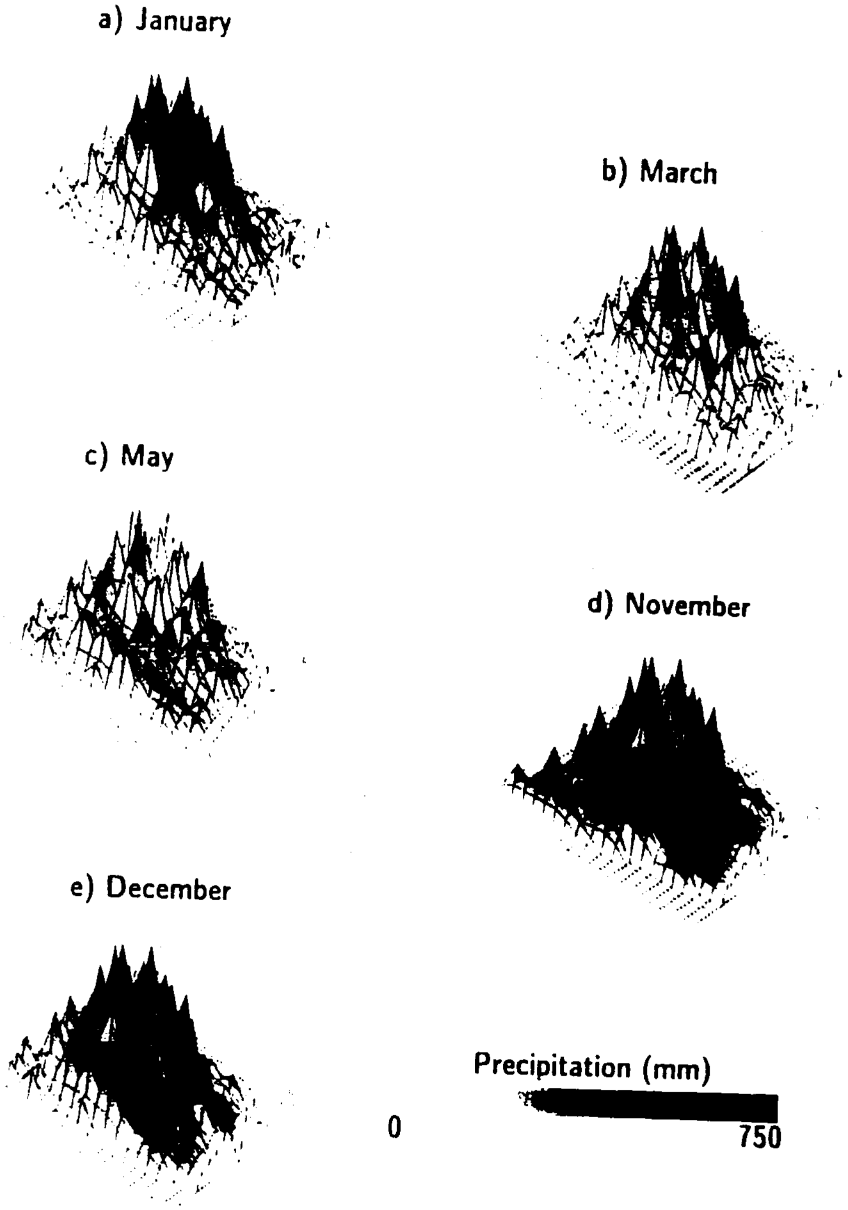

Figure 3.13 Monthly and annual spatial distributions of mean precipitation for the (1967-1974) simulation period: a) January; b) March; c) May; d) November; e) December.

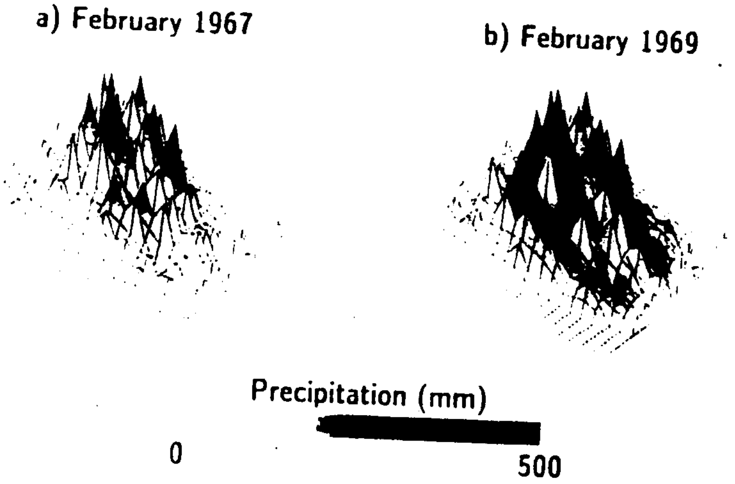
a) February 1967

b) February 1969

Figure 3.14 Monthly precipitation for selected simulation periods: a) February 1967;b) February 1969.

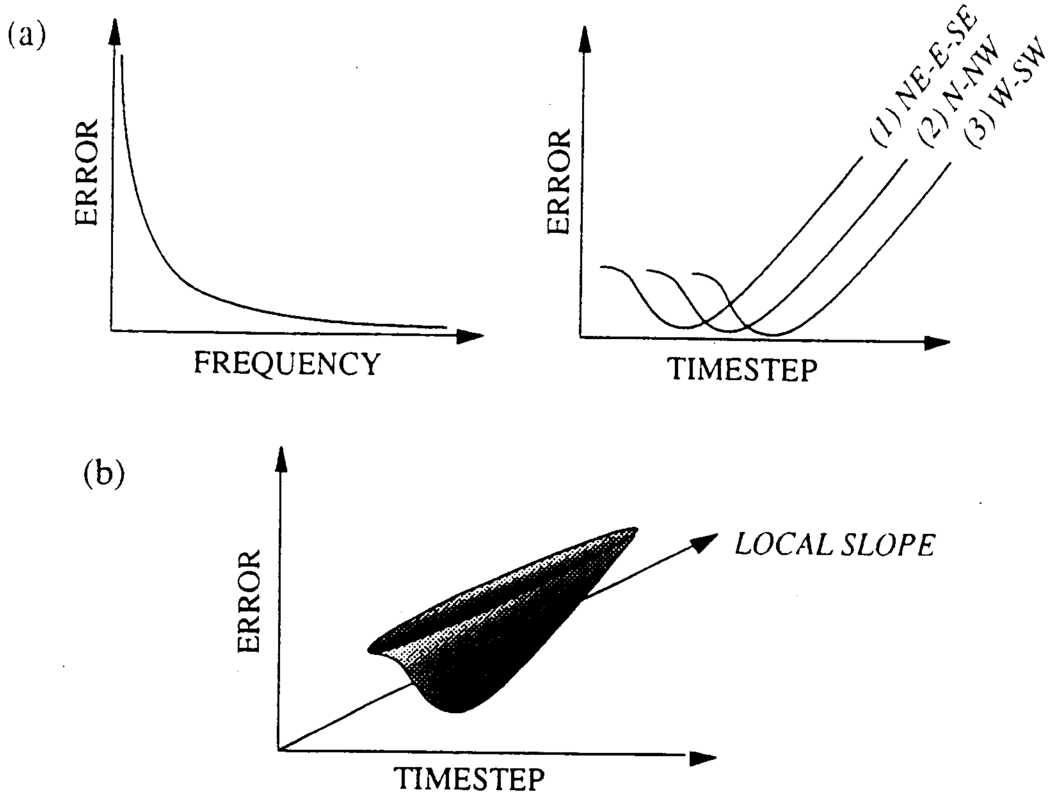

Figure 3.15 Qualitative analysis of spatial and temporal variability of error associated with the time integration process: a) as a function of frequency of storm arrival and time-step; b) as a function of local slope and time-step.

CHAPTER IV - AN EVAPORATIVE COOLING SCHEME FOR OROGRAPHIC PRECIPITATION MODELING

"Whatever I say will happen or not: truly the great Apollo grants me the gift of forecasting."

Horace, 30 BC (after Fortescue 1980)

4.1 Background

In Chapter III, a regional 3D Lagrangian model for the simulation of precipitation in remote mountainous areas was presented. Model variables are moist static energy h_M and total water Q, which are conservative under adiabatic conditions (Eqs. 3.1-3.4). Precipitation rates p(x,y,z,t) are computed as a fraction of total cloud water q_p, which is composed of liquid q_l and ice phases q_i. The partitioning between cloud water and precipitating water p is determined through the calibration of a spatially varying precipitation efficiency parameter K (Eq. 3.6). The total precipitation P at the ground is obtained by integrating the vertical distribution of precipitation rates along the atmospheric column between the surface and 250 hPa (Eq. 3.7).

The model was used successfully to simulate the spatial distribution of precipitation in the Olympic Mountains for a period of eight years. The Olympic Mountains are located in the northwestern US (approximately 47.5°N), in an area of humid mesothermal marine climate with cool summers. The model was subsequently applied to the Central Sierra Nevada Mountains, a region located approximately 10° of latitude south of the Olympic Mountains and characterized by humid mild winters and dry hot summers. Macroscale properties of precipitation common to both regions include: 1) a strong annual cycle due to the arrival of almost all major storms during late fall and winter; 2) most precipitation is associated with moist southwesterly flow forced by cyclonic anomalies aloft (700 hPa) in the North and Northeast Pacific Ocean; and 3) a clear display of orographic effects on the spatial distribution of precipitation (Walsh et al. 1982; Weare and Hoeschele 1983; Cayan and Roads 1984; Klein and Bloom 1987).

While incoming air masses have their low-level moisture removed along the Pacific coastal range before they reach the western slopes of the Sierras, the Olympics are the only orographic barrier met by weather systems crossing the Olympic Peninsula. In addition, the climatological mean temperatures between the surface and the 700 hPa level are significantly higher in the case of the Sierras than for the Olympics. Since the moisture holding capacity of the atmosphere increases with temperature, variations of the latter can also affect the efficiency of precipitation processes due to intensification of the depletion of settling hydrometeors by evaporative cooling. In this context, neglecting cooling due to the evaporation of precipitating water parcels, an approximation that worked well in the cool climate of the Pacific Northwest, led to substantial overestimation of precipitation amounts at high elevations on the western slopes of the Sierra Nevada Mountains as will be shown in Section 4.3.

To remedy this problem, three options could be considered: a) develop a more complex form for the precipitation efficiency parameter K; b) abandon the model in favor of a more complex description of cloud and precipitation dynamics, or; c) modify the model in a manner consistent with its relatively simple representation of governing physical processes. We rejected the first option because highly non-linear interactions among cloud processes could reduce calibration to a physically meaningless exercise. We rejected the second option because it would sacrifice the ability to perform routine multi-year simulations, and it was not clear that it would improve the quality of precipitation predictions (Barros and Lettenmaier 1993a). The third option was pursued because it is consistent with our goals of representing the hydroclimatology of mountainous areas as well as representing the dynamics of orographic precipitation at the time scales of individual storms (Barros and Lettenmaier 1993b). The crude representation of the thermodynamics in the original model was modified by the introduction of a simple evaporative cooling scheme (ECS). We will show that this modification produced dramatic improvements especially with regard to the model's ability to replicate wet and warm episodes.

4.2. Evaporative Cooling Scheme

The ECS adopted here consists of a simple interpretation of latent heat exchange between a descending plume of hydrometeors and the surrounding environment. First, the depth distributions of temperature, water, and precipitation in the atmosphere are discretized and assigned to each of the six reference heights coinciding with the 250, 500, 850, 900, 950, and 1000 hPa pressure levels pr in the model (Fig. 4.1a). For each atmospheric level i, precipitating water $p_i(x,y,t)$ is computed and its route to the ground subsequently tracked:

$$p_i(x,y,t) = \int_{z_{i,l}}^{z_{i,u}} p(x,y,z,t)\, dz \tag{4.1}$$

where $z_{i,u}$ and $z_{i,l}$ refer respectively to the upper and lower heights which bound the atmospheric layer i. All six layers act alternatively as "donors" (the layers where p originates) and as "sinks" (the layers where exchange of heat ϕ_T and moisture ϕ_Q are established between the transiting moisture p_d and the resident heat and moisture reservoirs T_b and Q_b, respectively (Fig. 4.1b)). Subscripts b and d refer respectively to the sink and donor layers. The tracking process is initiated for the top layer, and repeated separately for each layer underneath. For each repetition, the donor is the uppermost layer yet to contribute, while the layers underneath behave as sinks (Fig. 4.1a). Hence, the effective contribution $p_{i,g}$ of the i^{th} layer for the total precipitation P at the ground can be expressed as the difference between its maximum value p_i in the absence of any interaction between settling moisture parcels and the surrounding environment and the accumulated losses to each of the sink reservoirs ϕ_Q^{ij}:

$$p_{i,g}(x,y,t) = p_i(x,y,t) - \sum_{j=1}^{i-1} \phi_Q^{ij} \tag{4.2a}$$

and

$$P(x,y,t) = \sum_{i=1}^{6} p_{i,g}\,(x,y,t) \tag{4.2b}$$

Let us now consider the variation of temperature dT associated with the removal of a fraction α of incoming precipitating water:

$$\alpha = \frac{c_p\, dT}{L\, q_d^o} \tag{4.3a}$$

$$q_d^o = \frac{p_d^o}{M_d} \tag{4.3b}$$

where the superscript o refers to values prior to any donor/sink interaction, L is the latent heat of vaporization, q_d is the specific humidity of the donor at the level of the sink, and M_d is the mass of moist air associated with the donor. For each time-step, mass and energy transfers are regulated by the following: a) hydrostatic approximation; b) uniform settling velocity; c) conservation of the moist static energy of the sink, and; d) the interaction between donor and sink is ignited only if the sink is not saturated and if it is warmer than the donor (see Fig. 4.2). The latter implies that heat conduction between two saturated media is neglected, and condensation is inhibited (e.g. falling raindrops are not allowed to grow).

The maximum amount of cooling in the sink can be computed by assuming its saturation for a specific humidity qs_b as a consequence of the exchange of mass and energy with the itinerant donor:

$$qs_b = \alpha\, q_d^o + q_{v,b}^o \tag{4.4}$$

Using Bolton's empirical formula to describe the variation of the saturation vapor pressures with temperature for -30°C $\leq T \leq$ 30°C (Rogers and Yau 1989):

$$qs_b = pr_b{}^* \exp(\psi) \tag{4.5}$$

with

$$pr_b{}^* = 0.622 \left(\frac{611.2}{pr_b}\right)$$

and

$$\psi = \frac{17.67\,(T_b - 273.15)}{243.5 + (T_b - 273.15)}$$

Taking α and qs_b as defined by Eqs. (4.3) and (4.5) respectively, Eq. (4.4) can be modified to yield:

$$dT = \frac{L\, pr_b{}^*}{c_p}\, e^{\psi} - \frac{L\, q_{v,b}}{c_p} \tag{4.6}$$

When the value of α associated with dT given by Eq.(4.6) is greater than or equal to one, α is set equal to unity and dT can be estimated directly from Eq.(4.3).

The donor plume of hydrometeors leaves the reference height of the sink with readjusted properties (Fig. 4.1b):

$$T_d = T_d^o + dT \tag{4.7a}$$

$$p_d=(1-\alpha)\, p_d^o - M_b\, (qs_d - qs_d^o) \tag{4.7b}$$

where the absence of superscript is indicative of current values, and M_b is the mass of moist air of the sink. The properties of the sink are also consistently modified in a consistent manner:

$$T_b = T_b^o - dT \tag{4.8a}$$

$$Q_b = Q_b^o + \alpha\, p_b^o \tag{4.8b}$$

Consistent with the assumptions upon which the ECS was developed, the following conditions are observed at the end of each pair of interactions (Fig. 4.2):

$$T_b \le T_b^o \text{ and } T_d \ge T_b^o \tag{4.9a}$$

$$p_d \le p_d^o \text{ and } Q_b \ge Q_d^o \tag{4.9b}$$

4.3. Case Study

Three representative precipitation stations are the focus of this application (see Fig. 4.3): Grass Valley [U1] (39°:13N, 121°:04W) and Sierraville [U2] (39:35°W, 120:22°W) are located on the western slopes of the Sierra Nevada Mountains at two distinct elevations, yet both within the area where orographic effects upon precipitation are expect to be relevant; Bridgeport [L1] (38:15°W, 119:14°) is located in the "rainshadow" region in the lee of the mountains. The first semesters of 1985 and 1986 were the periods chosen for data analysis to allow adequate testing of model simulations for a variety of weather conditions including winter and spring storms. In addition, winter temperatures were on average three degrees warmer in 1986 than in 1985, and 1986 was a significantly wetter hydrological year. Table 4.1 provides data regarding the topographic elevation of the stations and the total precipitation amounts registered at the gauges during the time periods in study.

The methodology used in this application followed closely that described by Barros and Lettenmaier (1993a) for the Olympic Mountains. Radiosonde data collected at Oakland (37:27°W, 122:08°W) were used to infer initial and boundary conditions. The study domain is shown in Fig. 4.3. A spatial resolution of 40 km was used in the 3D finite-element representation of the terrain and adjacent atmosphere. Two versions of the model corresponding respectively to the original model formulation (MV0) and to the formulation modified by the incorporation of the ECS (MV1) were used in this study. From the 12 months of simulation which illustrate model performance in this Chapter, only one month, January of 1986, and only one model version (MV0) were utilized in the calibration of the precipitation efficiency parameter K. The post-processing methodology adopted by Barros and Lettenmaier (1993a) to account for low intensity wet episodes such as drizzle, which are insignificant in the Sierra Nevada, was not incorporated in this application.

To evaluate the change in the model's forecast ability, a threat score coefficient similar to that used by Giorgi et al. (1993) was adopted. For a precipitation threshold P_o, the threat score coefficient F_c is defined as a function of N_o and N_m, respectively the number of observations and model forecasts that exceed P_o, and the number of storms N_s for which predicted and measured amounts are simultaneously above the same threshold ($0 \leq N_s \leq N_o$):

$$F_c = \frac{N_s}{N_o+N_m-N_s} \tag{4.10}$$

Forecast accuracy increases with F_c from zero (missed forecast) up to unity (perfect forecast). To cover most of the important types of storms observed in the region, four distinct threshold precipitation values were used in this application: P_o = 1 mm day-1 (forecast of wet versus dry episodes); P_o = 13 mm day-1 (forecast of small storms); P_o = 26 mm day-1 (forecast of medium storms); P_o = 65 mm day-1 (forecast of large storms). Precipitation below 1 mm day-1 is not considered since this is the order of magnitude of precipitation gauge measurement error (Linsley et al., 1982). In addition, a second threat score F_t was defined to evaluate the forecast accuracy of the time of storm arrival at a given location:

$$F_t = \frac{N_{sd}}{N_{od}+N_{md}-N_{sd}} \tag{4.11}$$

where N_{od} is the number of observed storm arrivals, N_{md} is the number of simulated storm arrivals, and N_{sd} is the number of concurring storm arrivals between observed and simulated time-series of precipitation (in the absence of phase errors $N_{sd}=N_{od}$). Only storms during which precipitation rates reached or exceeded 13 mm day-1 were used to compute F_t.

Table 4.2 summarizes the threat score coefficients obtained for 1985 and 1986 and for simulations obtained with model versions MV0 and MV1 respectively. Figures 4.4 and 4.5 allow one-on-one comparisons between observed and simulated daily precipitation values, while Tables 4.3 and 4.4 summarize forecast accuracy with respect to the time of storm arrival and total winter precipitation. Simulations carried out with the modified version of the model MV1 show an overall improvement of all accuracy measures when compared with those obtained by running the original version. The most noticeable effects can be found in the forecast of storm properties for the 1986 simulations and at the two stations located at higher elevation (U2 and L1), for which the accuracy increments are always above 20 percent for the case of intense storms. These results are especially valuable in that such episodes are responsible for a major component of runoff response and snow accumulation in this region. The largest errors reported in Table 4.4 are associated with the simulation of the dry and cold winter of 1985. This is not unexpected in that the analysis of the performance of the original version of the model in the previous application to the Olympic Mountains showed that larger errors tended to occur for the dry and cold weather conditions, especially in the lee of mountains (Barros and

Lettenmaier 1993a). In addition, the evaporative cooling scheme is only activated in the presence of significant amounts of atmospheric moisture at relatively warm temperatures. Therefore, the scheme was not activated for many of the storms of 1985, but was activated for most of the storms of 1986. This is confirmed by the synchronism between the occurrence of heavy storms and strong short-term increases of the mean air temperature between the surface and 850 hPa extracted from the radiosonde data. Comparison of Fig. 4.4b with Fig. 4.6a for the period of ten days between Julian days 30 and 40 and of Fig. 4.5b with Fig. 4.6b for the period of ten days between Julian days 40 and 50 gives a clear indication of the dependence of the ECS efficiency on the temporal gradients of low level atmospheric temperatures.

4.4. Summary

An orographic precipitation model based on the simulation of Lagrangian transport of atmospheric moisture and moist static energy with parameterized microphysics showed poor forecast ability in the replication of intense winter storms associated with warm weather conditions. In particular, short, intense storms were depicted frequently by the model as longer episodes with appreciably lower daily precipitation amounts. As a corrective measure, a simple evaporative cooling scheme aimed at the regulation of the interaction between settling hydrometeors and the lower troposphere was developed. Comparison of model results before and after the modification of the model due to the introduction of the ECS show improvement greater than 20 percent in the accuracy of model forecasts at high elevations and for intense storms.

The influence of orography on the establishment of local climates is not restricted to precipitation, but extends to other components of the hydrological cycle in mountainous regions such as the production of runoff and the spatial variability of latent and sensible heat fluxes. Long-term concerted interactions between land-surface and atmospheric processes set the stage for the establishment of local patterns of the hydrological cycle. Next, we propose a methodology to facilitate adaptive multilevel coupling of hydrological and atmospheric models, and we investigate its applicability to the study of orographic influences on regional hydroclimatology.

Table 4.1 Elevation at the location of the reference stations and observed precipitation totals for the first semesters of 1985 and 1986. Total winter precipitation at the stations corresponds to 95% the semester values.

Stations	Elevation (m)	P_{1985} (mm)	P_{1986} (mm)
U1	732	461	1256
U2	1518	230	513
L1	1972	108	310

Table 4.2 Forecast accuracy of model simulations prior to the incorporation of the ECS scheme and incremental change due to inclusion of the ECS scheme (in parenthesis), as quantified by the threat score coefficient F_C (Eq. 4.10), for different values of threshold precipitation: (1) P_O= 1 mm day^{-1}; (2) P_O = 13 mm day^{-1}; (3) P_O = 26 mm day^{-1}; (4) P_O = 65 mm day^{-1}.

Stations		U1	U2	L1
(1)	1985	0.79 (-0.26)	0.43 (+0.29)	0.46 (-0.11)
	1986	0.71 (-0.07)	0.41 (+0.12)	0.38 (+0.29)
(2)	1985	0.45 (0.00)	0.50 (-0.12)	0.00 (+0.50)
	1986	0.73 (+0.16)	0.67 (+0.04)	0.10 (+0.19)
(3)	1985	0.29 (+0.31)	0.20 (+0.30)	----
	1986	1.00 (-0.14)	0.50 (+0.50)	0.20 (+0.47)
(4)	1985	0.00 (+0.67)	----	----
	1986	1.00 (-0.25)	0.75 (+0.25)	0.33 (+0.67)

---- storms of this magnitude were neither observed or simulated

Table 4.3 Forecast accuracy of the time of storm arrival, as quantified by the threat score coefficient F_t (Eq. 4.11) for storms with precipitation rates $\geq$ 13 mm day^{-1}: (a) prior to the incorporation of evaporative cooling; (b) after incorporation of evaporative cooling.

Stations		U1	U2	L1
(a)	1985	0.74	0.57	0.43
	1986	0.67	0.80	0.59
(b)	1985	0.95	0.50	0.60
	1986	1.00	0.78	0.70

Table 4.4 Percentage errors in total winter precipitation amounts: (a) prior to the incorporation of evaporative cooling; (b) after the incorporation of evaporative cooling. [expressed as (observed - simulated)/ observed]

Stations		U1	U2	L1
(a)	1985	+2%	-36%	-98%
	1986	+4%	+43%	-10%
(b)	1985	-10%	-13%	-61%
	1986	-9%	-8%	+8%

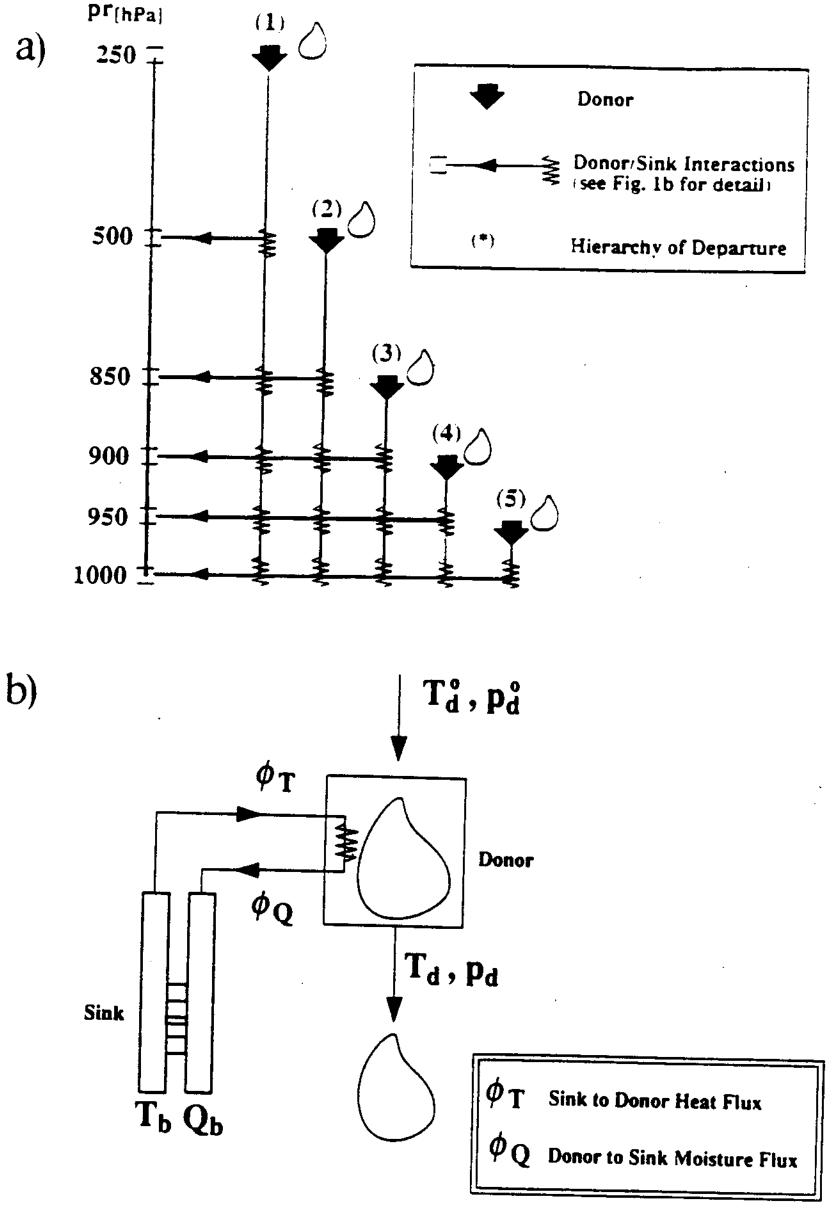

Figure 4.1 Conceptual interpretation of the implementation of the evaporative cooling scheme: a) ECS implementation (1D, vertical) for an atmospheric column at nodal position in a finite-element grid; b) Donor/Sink interactions.

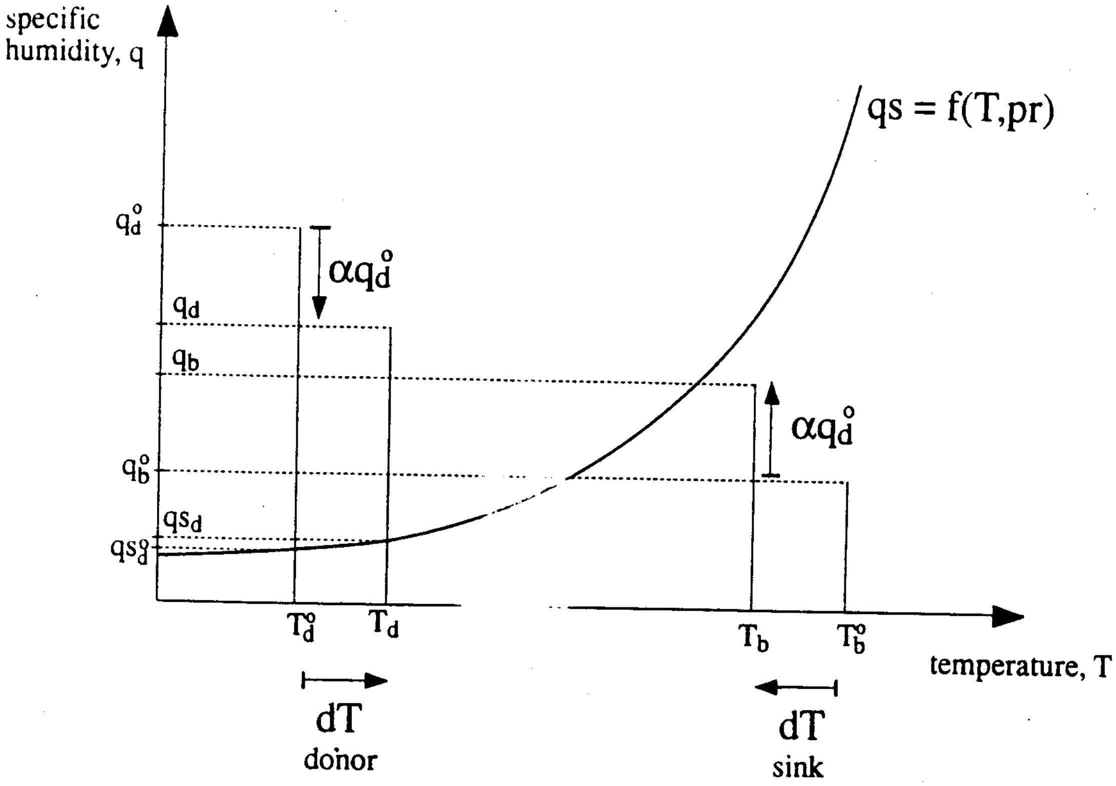

Figure 4.2 Variations of specific humidity q and temperature T allowed during the interaction between the traveling donor and the fixed sinks.

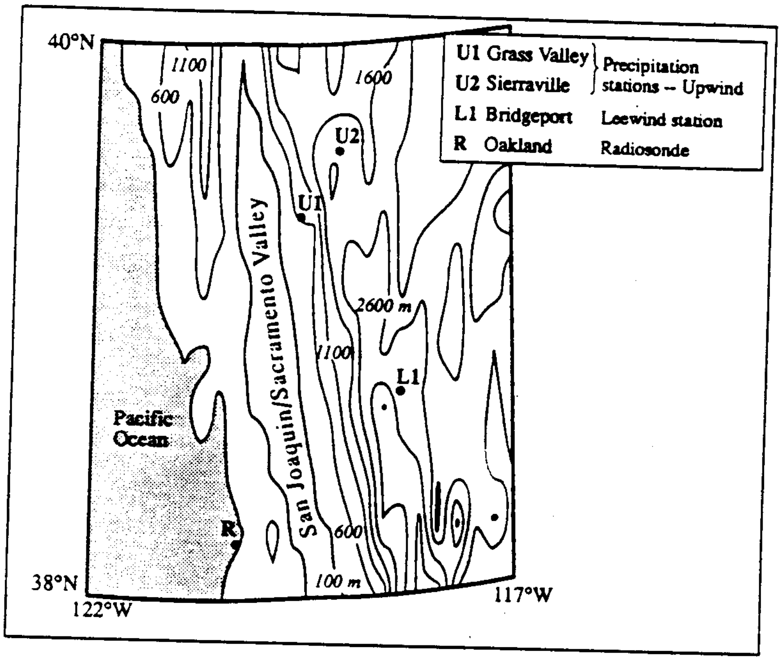

Figure 4.3 Map with the locations of the reference precipitation and radiosonde stations. (Upwind precipitation stations - U1, U2;
Leewind precipitation station- L1;
Radiosonde station at Oakland - R)

(a) 1985 - MV0 Simulations

Grass Valley

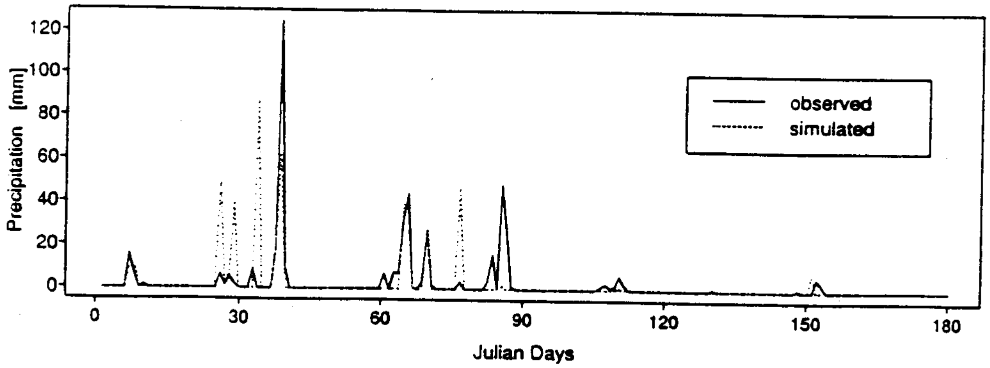

Sierraville

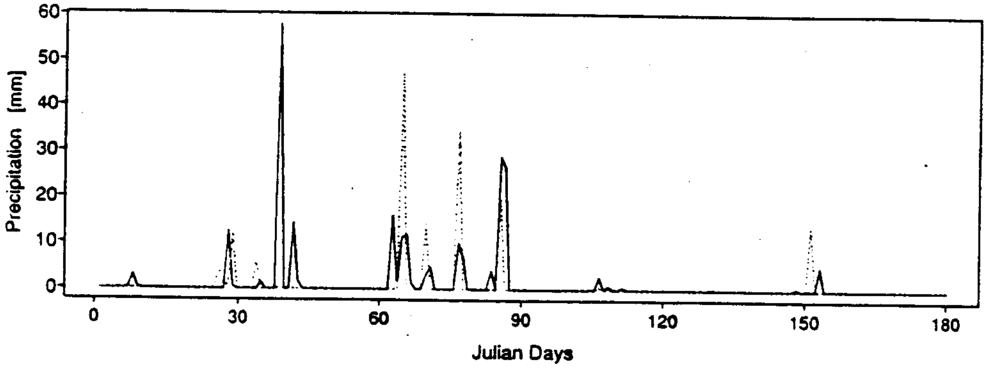

Bridgeport

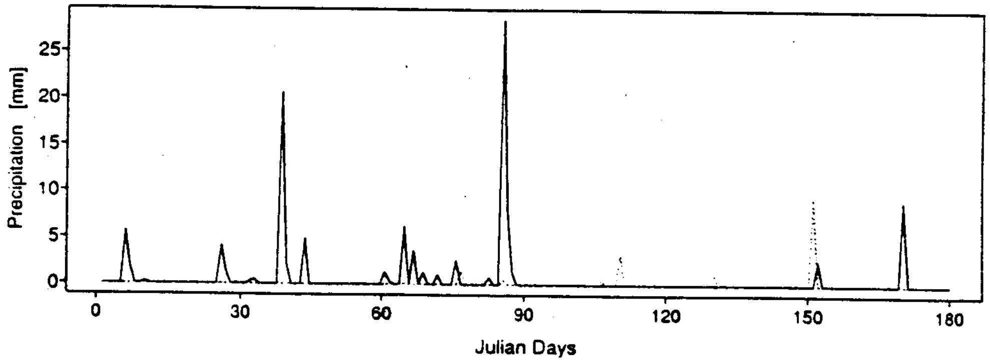

Figure 4.4 Comparison between observed and simulated daily precipitation at the location of the precipitation gauges shown in Fig. (4.3) for the first semester of 1985: a) MV0 simulations.

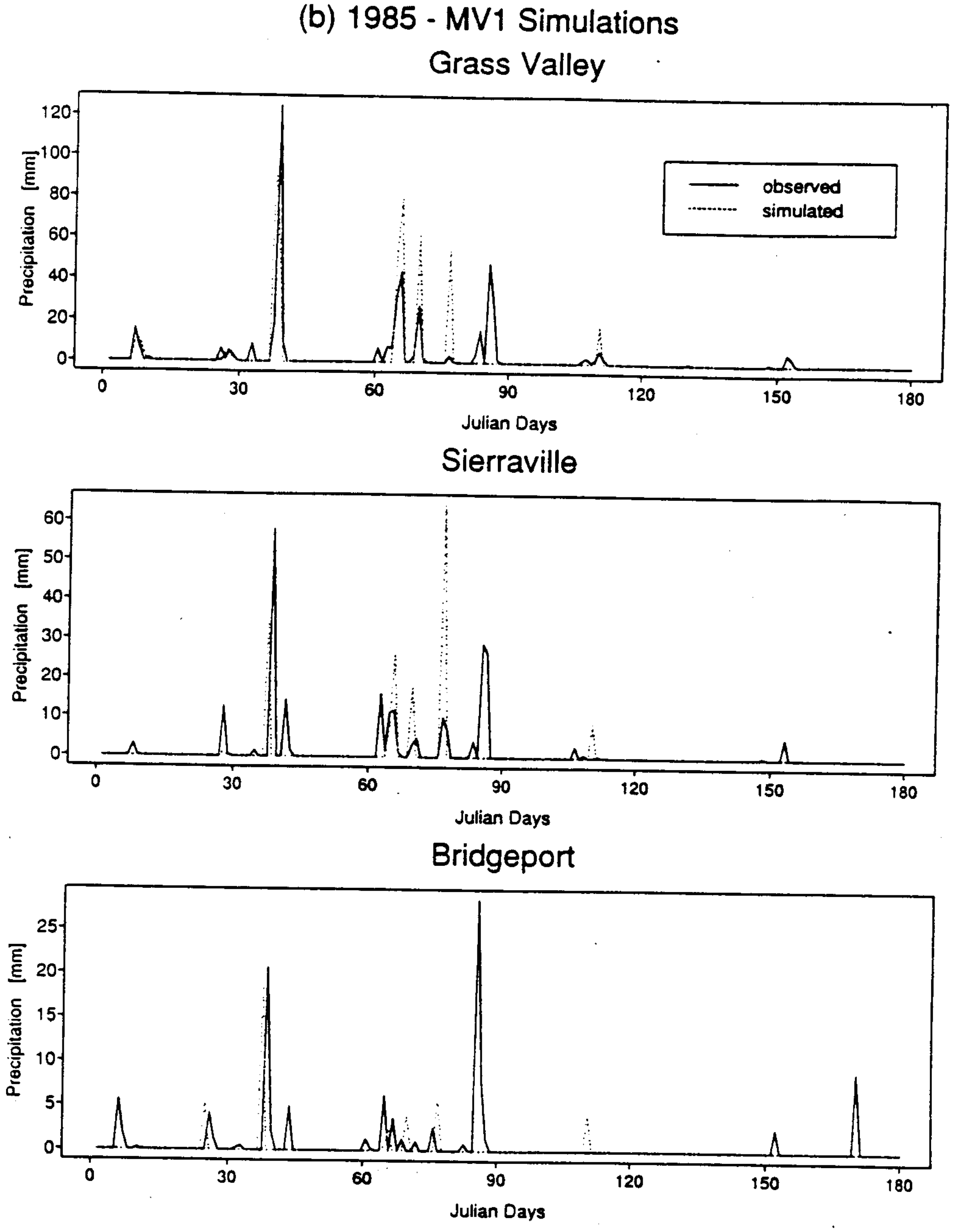
(b) 1985 - MV1 Simulations

Grass Valley

Sierraville

Bridgeport

Figure 4.4 (continued) Comparison between observed and simulated daily precipitation at the location of the precipitation gauges shown in Fig. (4.3) for the first semester of 1985: b) MV1 simulations.

(a) 1986 - MV0 Simulations

Grass Valley

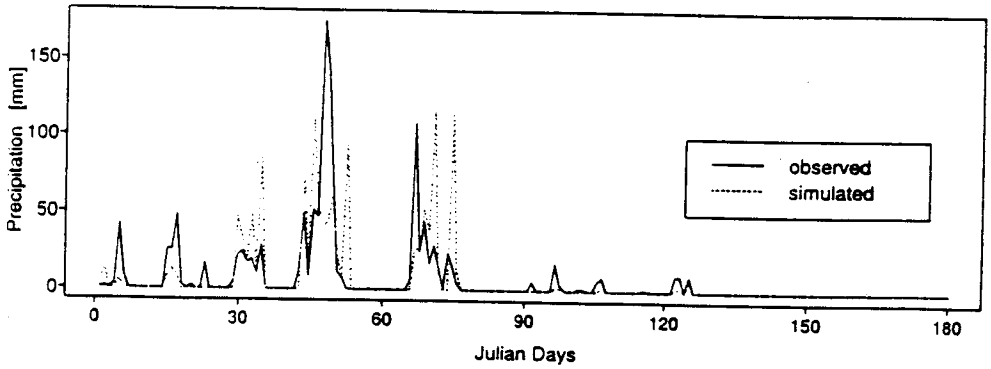

Sierraville

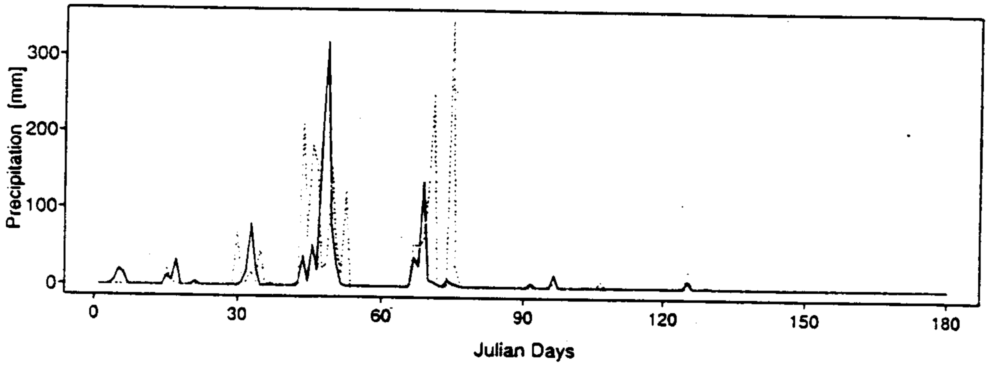

Bridgeport

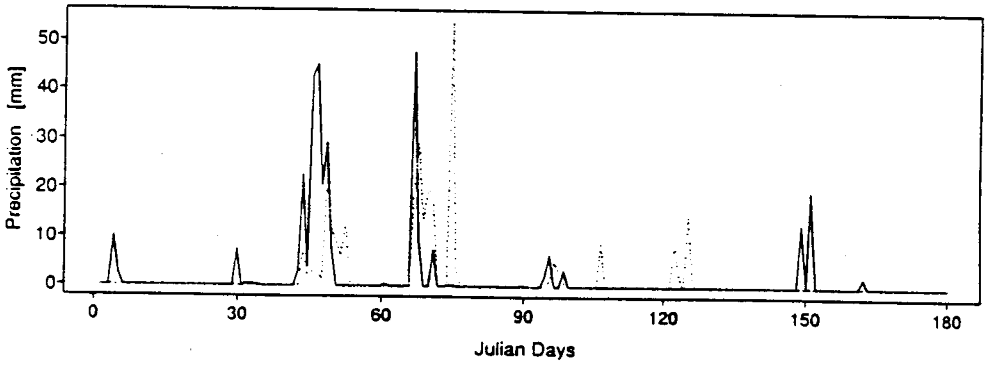

Figure 4.5 Comparison between observed and simulated daily precipitation at the location of the precipitation gauges shown in Fig. (4.3) for the first semester of 1986: a) MV0 simulations.

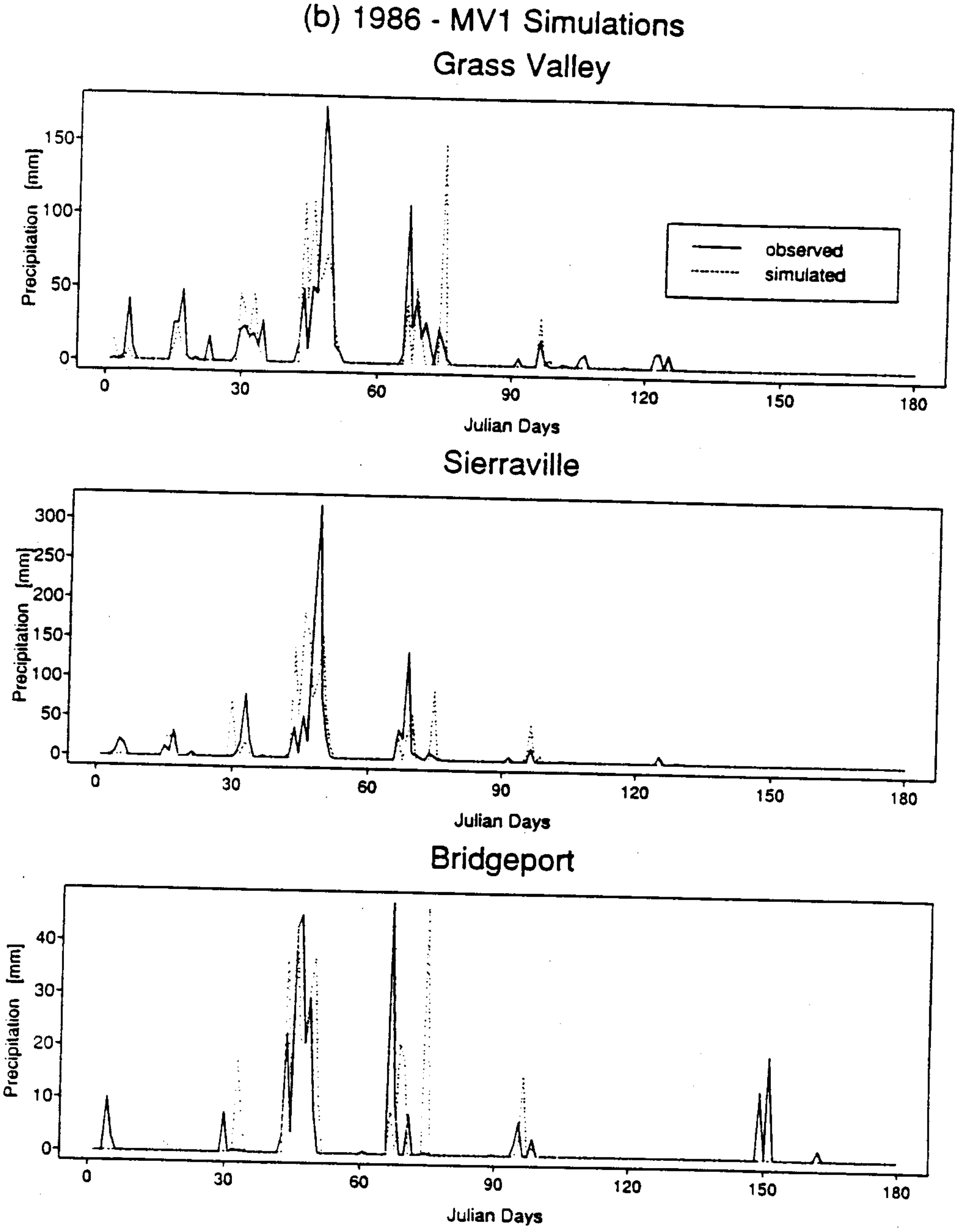
(b) 1986 - MV1 Simulations

Grass Valley

Sierraville

Bridgeport

Figure 4.5 (continued) Comparison between observed and simulated daily precipitation at the location of the precipitation gauges shown in Fig. (4.3) for the first semester of 1986: b) MV1 simulations.

(a) Mean Air Temperature - Oakland, 1985

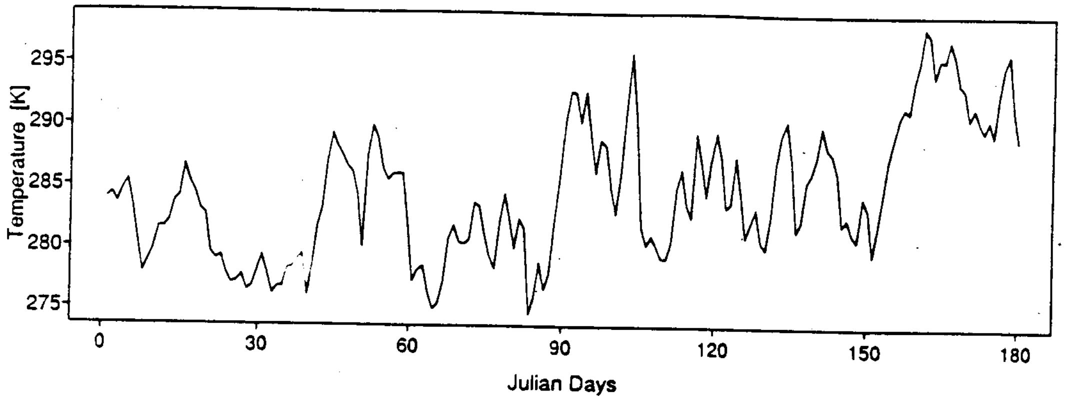

(b) Mean Air Temperature - Oakland, 1986

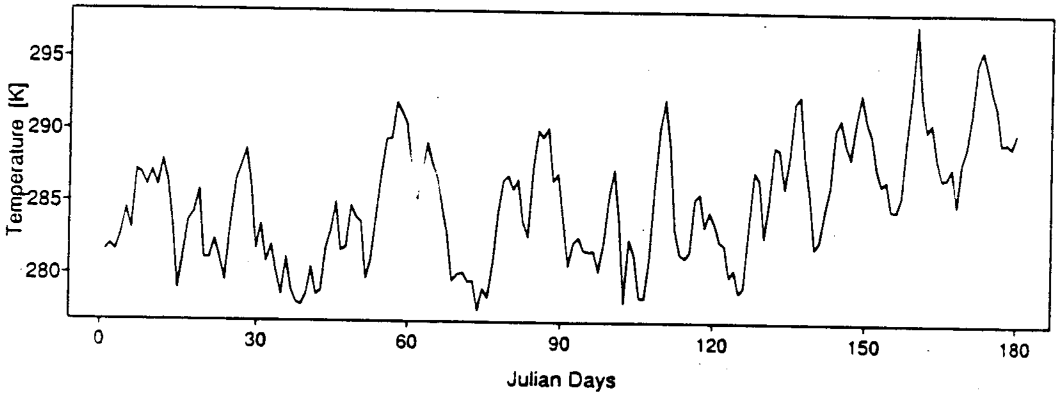

Figure 4.6 Mean air temperature in the lower troposphere between the surface and 850 hPa as extracted from the radiosonde data at Oakland: a) 1985; b) 1986.

CHAPTER V - ADAPTIVE MULTILEVEL COUPLING FOR HYDROCLIMATOLOGICAL MODELS

"The way up and the way down are one and the same."
Heraclitus, 500 B.C.

5.1 Introduction

Geophysical phenomena are normally expressed as conservation laws of mass, energy, etc, which can be described by nonlinear partial differential equations (NL-PDEs) of the form:

$$\frac{\partial E}{\partial t} + G(E)\ \nabla .\ F(E) = Q(x,y,z) \tag{5.1}$$

where the conserved variable $E = E(x,y,z,t)$ is some real variable, and G, F and Q are arbitrary functions (Glimm 1991). PDEs can be classified as parabolic (e.g. the diffusion equation), hyperbolic (e.g. the wave equation), and elliptic (e.g. the Laplace equation). Equation (5.1) behaves in a way similar to that of the wave equation. Hyperbolic equations, for which the eigenvalues of the Jacobian matrix are real and distinct, are characterized by unique and stable solutions (Morse and Feshbach 1953). Frequently, potential terms of the type ($\nabla^2 E$) are also part of geophysical PDEs, thus introducing ellipticity in the equations. In the case of elliptic equations, the eigenvalues of the Jacobian matrix are complex, and the solutions exhibit non-uniqueness and instability. Systems of NL-PDEs can only be solved numerically.

Because numerical solutions are necessarily discretized in both time and space, parabolic terms of the form ($\nabla \vartheta \nabla E$) are introduced artificially in the algebraic equations to assure mathematical consistency with regard to truncation errors (Roache 1972). Mathematically, ϑ, which can be interpreted as a friction or diffusion parameter, is a measure of the interaction between sub-grid scales and those resolved by the discretization. The result is that even strictly hyperbolic PDEs become elliptic. Physically, this implies that phase displacements are imposed upon the propagation of the solution modes, therefore inducing nonlinear multiscale interactions (e.g. resonance), and both temporal and spatial non-stationarity (Perrier 1989, Elsner and Tsonis 1992).

Although mathematicians continue the search for algorithms that may overcome the limitations imposed by discretization (Glimm 1991), at present the resolution of the multiscale interaction problem for geophysical studies (e.g. climate change, weather prediction, hydrology) can only be achieved by refinement of spatial and temporal discretizations, or else parameterization of the unresolved processes. This concern is clear from the current proliferation of publications on one-way nested modeling, and on the parameterization of land-atmosphere interactions in GCMs (Entekhabi and Eagleson 1989, Giorgi and Mearns 1991, Avissar and Verstraete 1991, Thomas and Henderson-Sellers 1991). The combination of mesoscale and limited area models (LAM) is a typical example of one-way nested modeling where the boundary conditions for the finer resolution model are obtained by running an independent macroscale model (e.g. a GCM).

Both one-way nested modeling, and conceptual parameterization strategies have critical shortcomings for the simulation of the space-time variability of precipitation. The lack of dynamic feedback between nested and parent solutions is equivalent to neglecting the dynamics of land-atmosphere interactions except within a limited mesoscale region, and for the current time-step. The parameterization of sub-grid scale processes, such as infiltration and evapotranspiration, as fractional fluxes without reference to spatial location precludes the observation of physical forcing-response similarity laws, or consistency across scales (Thomas and Henderson-Sellers 1991). Other approaches, such as fractal and self-similar representations, and spatial statistics in general can be useful for short-term, localized dynamical state-space modeling. Because of the lack of physical determinism, medium and long-term diagnosis or prognosis are beyond the scope of these latter methods (Namias 1980).

We address here the need to develop a methodology to facilitate multiscale coupling of hydrologic and atmospheric models, and hence to provide a means to perform long-term dynamical, physically-based disaggregation of precipitation from the macroscale to the field scale. The macroscale, for our purposes, is the spatial resolution of GCMs (typically on the order of hundreds of kilometers), and the field scale is that for which a specific regional phenomenon is resolved with adequate accuracy (e.g. the estimation of the distribution of orographic precipitation for hydroclimatological studies). The methodology must be robust enough to accommodate feedback mechanisms, implying mutual reversal between aggregation and disaggregation. Adaptive multigrid methods (AMMs), which formalize a strategy to couple discretization and solution processes, satisfy these requirements (McCormick 1989 and 1992).

5.2 Adaptive Multigrid Methods

AMMs are adaptive in the sense that they treat spatial non-stationarity resulting from multiscale interaction of state variables as an anomaly to be described as the concatenation of quasi-stationary contributions (Flandrain 1989). This is achieved by resolving the equations in a multilevel space, which results from discretizing the study domain at various spatial lengths. The objectives are to limit the range of interaction among variables and to isolate the contribution of particular scales to the overall solution. In practical terms, quasi-stationarity is maintained across scales by refining the discretization up to the point at which multiscale interaction among state variables can be expressed as a linear combination of state variables at different scales.

Multigrid schemes allow great flexibility by compounding discretization refinement with solution accuracy. A local grid network can be implemented to mimic a telescope covering a cascade of decreasing scales, from the GCM to the field scale. The base solution (e.e. the coarsest scale) is corrected successively with the quasi-stationary contribution of land-atmosphere interactions at each intermediate scale. In practice, this results in patching several levels of increasingly finer regional grids to a host grid (GCM), and having the regional grids function as a system of magnifying lenses aimed at capturing land surface singularities (see Fig. 5.1). This is equivalent to imposing a local signal on the low-pass filtered GCM solutions as illustrated by Fig. 5.2.

Adaptive multigrid methods originated from the need to discretize admissible Hilbert spaces of PDEs (e.g. the generation of the algebraic approximations to the PDEs) compatible with the numerical methods used to solve those systems of equations (Brandt, 1977). For the most part, these methods have been explored with the motivation of improving computational efficiency, and most of the research effort was carried out through numerical experimentation rather than through a formalized mathematical approach (McCormick and Thomas 1986, Brandt 1977 and 1989). With the development of parallel processing computers, there are renewed and promising applications for AMMs (Douglas and Miranker 1989, McCormick 1992).

The implementation of AMMs consists of solving first a system of algebraic equations on a coarse grid extending across the entire study domain. That solution is used as a first "guess", and the system is solved iteratively for a nested sequence of finer zonal grids until the desired accuracy is reached. For the modeling of physical processes, the decision to use multigrid methodology normally is based on an assessment of the effect of the complexity of local phenomena upon the convergence rate of iterative methods. Our interest in these methods is associated with the potential for modeling intergrid transfers of scale interactions, such as moisture and heat fluxes for example, and not computational efficiency per se.

What we seek is a strategy to approximate recursiveness between finer and coarser grids in the case of highly nonlinear PDEs. This does not constitute an obstacle for disaggregation (e.g. one-way nested modeling); a potential exists, however, to propagate spurious oscillations from finer to coarser scales when aggregating, in a manner similar to that observed in signal decimation (Crochiere and Rabiner 1987). For this reason, we will focus hereafter on the full approximation scheme (FAS), an AMM which provides a mathematical framework for consistent transfer of corrections across adjacent grid levels in the case of non-linear equations (see for example Brandt 1988, McCormick 1989 and McCormick 1992).

We review next the theoretical basis of AMMs. Detailed aspects of the effective implementation of the methods are discussed in Appendixes A, B, and C, which aim at complementing and clarifying the practical implications of the theoretical arguments. Appendix A illustrates the generation of a composite multilevel 1D grid, while an example of how to transform a PDE from its form in Eq. (5.1) to its approximated form in a discretized space Eq. (5.2) is described in Appendix B. The properties of intergrid projection operators are discussed in Appendix C.

First, let us consider a generalized PDE described as follows (Appendix B):

$$\mathrm{L\,v = f} \tag{5.2}$$

where $\mathrm{v} \in \mathrm{H}_1$ is a state variable, $\mathrm{f} \in \mathrm{H}_2$ is a known forcing, and L is some operator such that $\mathrm{L} : \mathrm{H}_1 \text{->} \mathrm{H}_2$, and H_1 and H_2 are admissible Hilbert function spaces.

Let S_h and $\mathrm{S}_{\alpha h}$ be non trivial finite-dimensional subspaces of the PDE space H_1, which are obtained through the discretization of H_1 into uniform grids of resolution h and αh respectively (Appendix A). Hereafter, $\mathrm{S}_{\alpha h}$ will refer to the local sequence of successively finer grids used to realize local grid adaptation, with α increasing from some fractional value at the field scale up to unity at the macroscale (e.g. α is a resolution ratio measure). The discretized PDE operators L_h and $L_{\alpha h}$ are related through the Galerkin condition,

$$\mathrm{L}_h = \mathrm{I}_{\alpha h}^{h}\,\mathrm{L}_{\alpha h}\,\mathrm{I}_h^{\alpha h} \tag{5.3}$$

where $\mathrm{I}_h^{\alpha h}$ and $\mathrm{I}_{\alpha h}^{h}$ are respectively the prolongation (disaggregation) and restriction (aggregation) intergrid transfer functions between the coarse scale h and the fine scale αh space.

In geophysical problems the discretized function spaces of the state variable and the forcing are identical, and therefore S_h and $\mathrm{S}_{\alpha h}$ are reciprocal to the corresponding finite-dimensional subspaces of H_2. Furthermore, the subspaces attached to the several levels of local grid adaptation are conformal in the sense that $\mathrm{S}_h \subset \mathrm{S}_{\alpha h}$ (the fine grid contains the coarse grid).

Now, let us define a composite subspace resulting from the union of all local subspaces (Appendix A):

$$\mathrm{S}_h^C = \mathrm{S}_h \sqcup \mathrm{S}_{\alpha h} \tag{5.4}$$

The conforming property implies that outside of the telescoping region $S_h^C = S_h$ holds, and hence the consistency of the global solution is preserved.

Intergrid transfers are defined by projection operators consistent with the numerical interpolation. These operators are adjoint, and thus the relationship between S_h and $S_{\alpha h}$ is given by (Appendix C):

$$I_h^{\alpha h} = (I_{\alpha h}^h)^T \tag{5.5}$$

Equations (5.3) and (5.5) constitute the variational conditions (McCormick 1989) which impose monotonicity to the transfers of energy across scales. This property assures convergence for AMMs, and is important to meet our objectives because it limits propagation of spurious oscillations.

Consider two adjacent levels of the local grid sequence, one of resolution h and another of finer resolution αh. In our notation, subscripts h and αh refer to the resolution interval of the grids, while the notation (˜) indicates a numerical approximation of the state variable. In the finite-dimensional spaces S_h and $S_{\alpha h}$, Eq. (5.2) takes the form:

$$L_h \, \tilde{v}_h = f_h \tag{5.6a}$$

$$L_{\alpha h} \, \tilde{v}_{\alpha h} = f_{\alpha h} \tag{5.6b}$$

We can rewrite Eq. (5.6a) as a function of the composite solution v^C by incorporating a correction resulting from interaction between h and αh :

$$L_h \, v_h^C = F_h + \tau_{\alpha h}^h \tag{5.7}$$

where

$$\tilde{v}_h = I_{\alpha h}^h \, \tilde{v}_{\alpha h} \tag{5.8a}$$

$$F_{\alpha h} = L_{\alpha h} \, \tilde{v}_{\alpha h} \tag{5.8b}$$

and therefore

$$\tau_{\alpha h}^h = L_h \, I_{\alpha h}^h \, \tilde{v}_{\alpha h} - I_{\alpha h}^h \, L_{\alpha h} \, \tilde{v}_{\alpha h} \tag{5.8c}$$

Finally,

$$\mathrm{v}_h^C = \tilde{\mathrm{v}}_h + \mathrm{I}_{\alpha h}^h \, \tilde{\mathrm{v}}_{\alpha h} \tag{5.9}$$

Equation (5.8c) tells us that the coarse grid solution can be corrected by incorporating the effect of processes operating at lower scales (aggregation), by projecting the higher order solution to the larger scale domain. Similarly, for disaggregation, we may write:

$$\mathrm{v}_{\alpha h}^C = \tilde{\mathrm{v}}_{\alpha h} + \mathrm{I}_h^{\alpha h} \, \tilde{\mathrm{v}}_h \tag{5.10}$$

5.3 Aggregation and Disaggregation

Within the area covered by a multigrid network or, going back to the telescope analogy, within the "field-of-view" of the regional window centered at the field scale αh, a few (typically one or two) main variables determine both the atmospheric and surface hydrology dynamics. What we hope to achieve by adopting an adaptive multigrid formalism is to overcome coarse scale resolution limitations by improving the estimation of those variables (e.g. the focal points of the geophysical landscape imaged with pixel size αh).

Two types of errors are encountered in large-scale simulations: fundamental errors linked to inadequate representation of physical processes for which first principles are yet to be understood; and implementation errors which link both the numerical approximation schemes of continuous partial differential equations and their spatial and temporal discretization. Fundamental errors are inherent to the model form; they can be eliminated only by improved understanding of the underlying processes. Due to the wide variety of numerical solution techniques and the range of discretization possibilities, implementation errors can be minimized. We refer to implementation errors for a particular numerical approximation (e.g. central versus upwind finite-differences) as algebraic or truncation errors of the first kind (TEK1), while implementation errors associated with the spatially varying coefficients of partial differential equations are termed truncation errors of the second kind (TEK2). The latter are responsible for spatial non-stationarity, also referred to as forced chaos

(Glimm 1991).

Regardless of the extent to which a geophysical phenomenon is understood, implementation errors are always present as long as discretization is necessary. Algebraic errors result from discretizing the PDE operators, and they vary with the numerical scheme selected. Numerical modelers argue over the best numerical approach to solve specific problems. Such discussions have been going on since the late 1970's generally without resolution, although there are often good reasons to justify the choice of one or another technique (Smolarkiewicz and Rasch 1991). We avoid such arguments and use Eulerian-Lagrangian techniques for reasons of convenience, and because we can rely on our previous development of the orographic precipitation model described in Chapters III and IV. Hence, we strive to manage and control TEK2 errors rather than examine different numerical solution techniques.

In principle, TEK2 errors result from interaction among scales smaller than the lowest scale resolvable at a given discretization spacing. A large number of unresolved scales exists between the upper limit set by the coarse resolution and the lower limit set by dissipative phenomena. For the purposes of our investigations this lower limit length scale is set at 10 km. In addition, for orographic singularities, we assume that long-term effects of nonlinear interactions such as the mesoscale phenomena triggered by air movement over and around a mountain are likely to occur predominantly within well-separated intervals in the spatial-frequency domain. Following Glimm (1991), we consider three major length scale intervals: (a) a dissipative interval located in the short scale domain ($\lesssim$ 10 km); (b) a synoptic forcing interval containing the length scales of the dominant flow field features ($\gtrsim$ 100 km, centered at $1/h$ in the spatial frequency axis in Fig. 5.2); and (c) an intermediate mesoscale inertial interval for which orographically induced dynamics prevail (centered at $1/\alpha h$ in the spatial frequency axis in Fig. 5.2). Our study domain is this inertial scale interval, within which we will attempt to mitigate the effect of TEK2, errors of second kind.

This line of thought can be formalized by considering a state variable v and a forcing variable F related by a generalized operator L, and their respective

GCM equivalents v_g, F_g and L_g:

$$R = L\, v - L_g\, v_g = F - F_g \tag{5.11}$$

where R is the total residual between the true value of variables and operators, and those implied by coarse discretization of the differential operators and the state variables. The residual is the summation of fundamental and implementation errors, respectively Υ_f and Υ_i:

$$R = \Upsilon_f + \Upsilon_i \tag{5.12}$$

and according to our previous distinction between TEK1 and TEK2

$$\Upsilon_i = \Upsilon_i^n + \Upsilon_i^{\alpha h} \tag{5.13}$$

where Υ_i^n are the algebraic errors linked to the numerical formulation, and $\Upsilon_i^{\alpha h}$ are the implementation errors resulting from aliasing (redistribution of energy from the smaller scales to the larger scales) of multiscale interaction within the inertial window located at the spatial frequency associated with the field scale αh.

Our objective is to reduce the implementation errors at the field scale (e.g. 10 km) to the magnitude of TEK2 errors compatible with solving the coarser model equations at this finer scale. There are many ways for transferring successive corrections between grid levels. The characteristics of the methods of interest for aggregation and disaggregation processes are: (1) full versus partial approximation; and (2) type of feedback implementation: coupling versus no coupling. Figure 5.3 illustrates the optional paths one may take in the implementation and coupling of the adaptive multigrid modeling concept.

Full coupling consists of completing as many intergrid correction transfers as necessary up to the point at which solutions do not change, or quantitative differences between successive solutions at a grid level are similar to TEK1 errors; full coupling of multivariable nonlinear problems is necessarily asynchronous. In multivariable nonlinear problems, the implementation of a numerical scheme implies some hierarchy in the solution process according to the level of interdependence among variables. This generally results in solving first for those variables which depend less on others. Those new updated solutions are used to compute the remaining variables. Hence, different variables are computed at different fractional time-steps in an asynchronous manner.

Partial coupling is carried out in similar manner to full coupling, but only across the grid levels within the "field-of-view" of the local window. Also, partial coupling may be synchronous or asynchronous depending on the nonlinearity of the original PDEs. Often, when faced with large numbers of mutually dependent nonlinear variables, asynchronism in the solution process is dealt with by shortening time-steps, and assuming that multivariable interactions within the time interval are stationary and independent, and can be linearized. This type of linearization falls within the category of TEK1 implementation errors, which are not addressed here.

The type of approximation, full or partial, is of great importance in the application of adaptive multigrid concepts to hydroclimatological modeling. Full approximation requires solving for the complete set of dynamical equations representative of all atmospheric phenomena. Partial approximation is used here to develop simplified models of processes relevant within a limited region of study. Such simplified models result from eliminating from the fundamental equations all terms which govern the physics relevant to a particular problem (e.g. orographically induced updrafts in the case of orographic precipitation). Thus, the underlying assumption is that locally, within the area controlled by the spatial scale αh, the terms dropped are negligible, or have negligible influence upon the principal variables. The validity and efficacy of this approach as an alternative way to current practice will be demonstrated through application to realistic situations and verified against field-data.

Uni-directional nested modeling approaches such as classical mesoscale models and limited area models (Anthes 1989, Giorgi and Mearns 1991) fall within the class of full approximation, no coupling. Because such models solve a set of equations similar to those of large-scale models, though generally using more sophisticated descriptions of land-atmosphere interactions at the mesoscale level (e.g BATS, SIBS), the creation of an iterative recursion link between GCMs and such models would be similar to a full approximation, full coupling scheme. It could be implemented as follows: 1) a GCM solution would be computed; 2) the mesoscale model would be operated and forced by the GCM output at the boundaries of the study domain; 3) the GCM would be rerun for the new set of land-surface and planetary boundary layer conditions; and 4) the solution is compared with the previous iteration and the process repeated until successive GCM solutions for the same time-step differ quantitatively by values of the order of magnitude of TEK1. The burden of building, or even running, a model to simulate full atmospheric dynamics is well beyond the scope of this work. Furthermore, the implementation of such a scheme is infeasible at present due to the same computational limitations which affect GCMs operationally.

The implementation of a partial approximation, partial coupling scheme consists of the following: 1) identify relevant mesoscale phenomenon and develop a simplified descriptive model to operate at the regional scale; 2) generate a regional multilevel grid network encompassing the scales at which the mesoscale phenomenon can be best described; 3) use large-scale data to force the regional model at the upper grid level; and 4) follow the steps described above for the full approximation, full coupling scheme but now restricted to the regional multilevel network. We will focus on the implementation of partial approximation and partial coupling schemes which fulfill requirements of internal consistency between aggregation and disaggregation mechanisms that can be especially useful for hydrological applications.

5.4 Partial Approximation - No Coupling Scheme (PA-NC)

PA-NC schemes are appropriate for adaptating global solutions to local conditions by updating the large-scale representation of physical processes with regional corrections forced upon those variables for which explicit feedbacks are assumed negligible. This is achieved by modeling separately the local and global independent components of a state variable (e.g. potential and rotational components of the flow field in our application), and combining the partial contributions to derive a complete solution within a limited study area.

5.4.1 Case Study: Description of the Spatial Distribution of Orographic Updrafts

The estimation of spatial distributions of precipitation, and therefore the detection of the vertical wind field patterns which trigger atmospheric thermodynamic activity in areas of strong topographic relief are a major objective of this investigation. The advantage of this approach for hydrological problems is that interactive feedbacks occur only between the governing state variables of a given phenomena and not the entire hydrological cycle.

There are two major ways in which topography affects regional circulation: to the upper and middle troposphere, mountainous areas act as rough lower boundary conditions; and to the lower atmosphere, mountainous areas are obstacles which impose aerodynamic lifting, flow blocking and separation. In addition, high mountainous areas behave as elevated sources of diabatic heating through radiative forcing. Flow fields in the vicinity of mountains are extremely complex due to the interaction of large-scale circulation features, gravity wave generation, and mountain-valley winds. We will concentrate only on the direct effect of a mountain's presence on momentum conservation. We will restrict our studies to daytime, quasi-potential, adiabatic flow deformation, while neglecting important phenomena such as, for example, convective activity and night time blocking. These assumptions are likely to be valid for the temperate regions of the Western U.S. where the methodology is tested, because of the strong annual cycle of precipitation in those regions (the contribution of convective activity during late spring and summer is marginal), and because more than 70 percent of annual orographic precipitation amounts in such regions occurs during the day (Table 5.1).

In Section 5.4.1.1 we describe the procedure used for computing orographic updrafts. This requires determining the potential flow field resulting from streamline deformation of synoptic circulation, which is affected by topographic relief and includes the effects of preservation of flow continuity. This purely kinematic depiction of the flow field has fundamental implications for the calibration and validation of the model for the Olympic Mountains

(Chapter III) where the rain-shadow effect on the lee-side of the mountains was excessive. The seasonality of precipitation modeled for the northern portion of the Olympic Peninsula was transposed: springtime precipitation contributed more to the annual totals than wintertime precipitation, the reverse of the observed climatology.

At first, the problem was approached by passing the outputs from the orographic model through a filter, which helped to overcome the model's failure to account for the effects of sea-breezes on coastal precipitation (Barros and Lettenmaier 1993a). Subsequent investigation of the model's performance upwind and downwind of mountain slopes suggested that although coastal breeze effects are important at the red noise level of spring and summer precipitation, the major problem with the model was that the flow field description failed to include relevant dynamic processes.

For the purpose of estimating spatial distributions of precipitation on an annual and monthly basis, the filtering approach previously used was satisfactory. From the standpoint of extending the models' range of applicability to the simulation of individual precipitation events on the lee sides of mountains, though, the filtering approach is inappropriate. The filtering approach also precludes sensitivity studies and use of the model in prognostic or diagnostic mode for a timeframe of less than a month.

The primary interference of a mountain with the synoptic flow field can be represented by conserving potential vorticity within the regional domain of study.The relationship between precipitation and the spatial phase of vorticity has been used in weather forecasting (Weare and Hoeschele 1983, Cayan and Roads 1984). We show below the nature of the differences between wind fields with and without introduction of potential vorticity dynamics in the calculations and their influence upon the estimation of the temporal and spatial distributions of precipitation. The differences are especially significant on the lee sides of the mountains where the greatest discrepancies were encountered with the earlier, simpler, approach.

5.4.1.1 Model Formulation

Consider an air column which is advected by frictionless, adiabatic flow over a mountain barrier. The conservation of potential vorticity implies that for the reduction of the depth of the air column a compensating flow adaptation must occur, the form of which can be obtained from first principles. The concept of potential vorticity is associated with the relationship between the strength and vertical extent of atmospheric vortices (Holton 1979). A complete overview of the physics and mathematics of vorticity is presented in Holton (1979) and Panton (1984); we reference here only those equations that are relevant to the formulation of the model. Mathematically the conservation law for the absolute vorticity η of a homogeneous incompressible fluid can be expressed as:

$$\frac{\mathrm{d}}{\mathrm{dt}}\left(\frac{\eta}{H}\right) = 0 \tag{5.14}$$

with

$$\eta = \zeta + \mathrm{f} = \frac{\partial v}{\partial x} - \frac{\partial u}{\partial y} + 2\Omega\ \sin\phi \tag{5.15}$$

where u and v are the x and y velocity components of the wind, Ω is the speed of the earth's rotation, and ϕ is the latitude, ζ is the vertical component of the vorticity (relative vorticity), and f is the contribution of the earth's rotation to the absolute vorticity. H=H(x,y,t) is the depth of the air column as it crosses over the mountain. From an Eulerian perspective the dependence of H on time can be eliminated, because for the time scales of our simulations no significant change of regional orography is expected:

$$\frac{\mathrm{d}}{\mathrm{dt}}\left(\frac{\eta}{H}\right) = \frac{1}{\mathrm{H}}\frac{\mathrm{d}\eta}{\mathrm{dt}} - \frac{\eta}{\mathrm{H}^2}\frac{\mathrm{dH}}{\mathrm{dt}} = \frac{1}{\mathrm{H}}\frac{\mathrm{d}\eta}{\mathrm{dt}} - \frac{\eta}{\mathrm{H}^2}\left[u\frac{\partial \mathrm{H}}{\partial \mathrm{x}} + v\frac{\partial \mathrm{H}}{\partial \mathrm{y}}\right] \tag{5.16}$$

Continuity of an homogeneous and incompressible air column requires that

$$\frac{1}{\mathrm{H}}\frac{\mathrm{d}\eta}{\mathrm{dt}} = \frac{\eta}{\mathrm{H}}\frac{\partial \mathrm{w}}{\partial \mathrm{z}} \tag{5.17}$$

where w is the vertical velocity. Combining Eqs. (5.16) and (5.17) yields

$$\frac{\partial \mathrm{w}}{\partial \mathrm{z}} = \frac{1}{\mathrm{H}}\left[u\frac{\partial \mathrm{H}}{\partial \mathrm{x}} + v\frac{\partial \mathrm{H}}{\partial \mathrm{y}}\right] \tag{5.18}$$

which is the equation solved in the model. In our formulation, the top of the atmosphere is set at the 250 hPa pressure level, and the finite-element mesh is similar to that of the orographic precipitation model (Barros and Lettenmaier 1993a).

The PA-NC approach offered in this Section is applied by recognizing that the vertical wind field calculated under the assumptions of potential flow must be corrected to account for rotational effects. The corrected vertical wind field w_c results from

$$w_c = w_p + w_r \tag{5.19}$$

where w_p is the vertical wind field obtained from estimating vertical velocities under potential flow conditions (see Section 3.3.2), and w_r is the corrective field due to flow rotationality.

In summary, the methodology is:

(a) disaggregate large-scale wind fields to a finer scale through the potential flow equations and obtain w_p;

(b) compute the contribution w_r of local effects to the wind field in the projection space of (a); and

(c) combine the contributions of (a) and (b) to obtain w_c.

For the implementation of the PA-NC scheme we followed pathway (2) in Fig. 5.3, and used radiosonde data as a surrogate for GCM forcing. In the context of a PA-NC type of scheme, friction, variation of Coriolis effect, and isentropic instability were ignored in a $2\frac{1}{2}$D finite-element model to compute the vertical wind field resulting from forcing conservation of potential vorticity.

5.4.1.2 Results

We applied the PA-NC approach to the Olympic mountains (see Fig. 3.2) to investigate seasonal precipitation patterns on the lee-side of the mountains. The simulation was conducted for the winter/spring period of 1967, during which precipitation depths for significant storms were underestimated substantially by the previous model at the locations of lee-side precipitation stations. No additional calibration was carried out for the second application; the only change was in the distribution of vertical winds.

Figures 5.4a and 5.4b show the horizontal distribution of orographic updrafts, respectively, before and after imposing the rotationality correction for the wind field associated with a southwesterly storm in the second week of January, 1967. Figures 5.5a and 5.5b show the distribution of the vertical wind field along the West-East transverse profile marked in Fig. 5.4a. The most striking differences between Figs. 5.4a and 5.4b, and 5.5a and 5.5b, are the extension and spatial distribution of the areas corresponding to strong updrafts resulting from incorporation of the vorticity correction. The impact of these differences upon the results obtained can be viewed from two perspectives. On the one hand, the extension of convergence areas decreases for the corrected case; less moisture is lost to precipitation on the upwind side of the mountains, and therefore more moisture is available to be released on the lee side. On the other hand, stronger convergence located in the general area of influence of the "problem" stations acts as a catalyst for cloud formation, and ultimately precipitation on the lee side. A quantitative summary of these changes is resented in Fig. 5.6.

On the upwind slopes no significant differences were found in the predicted precipitation for the two simulations. Although positive and negative changes occurred for individual storms, they were not significant with respect to the annual and monthly precipitation amounts (stations 1, 4, 5 and 8 in Fig. 5.6). The results improved greatly at the problem stations (stations 2, 3, 6 and 7 in Fig. 5.6) for which the seasonality shift from wintertime to springtime was eliminated.

This demonstrates how it is possible to modify disaggregated large-scale solutions by introducing mesoscale corrections which bear on regional hydroclimatological patterns. The corrections consisted of modifying the vertical wind field by the dynamics of the conservation of potential vorticity in a mountainous region, which cannot be resolved by a GCM (Fig. 5.1). The problem with this application is that while the correction improves the model predictions in the region studied, there is no feedback to the global solution, and hence no means for studying the impact of land-atmosphere interactions on climate.

5.5 Partial Approximation - Partial Coupling Scheme (PA-PC)

From the point of view of continental hydrology, and particularly for macroscale studies of large continental areas, the ability to carry out high-resolution studies without having to compromise fundamental feedbacks to the general circulation of the atmosphere is essential. We have implemented a partial approximation - partial coupling (PA-PC) aggregation/disaggregation scheme to achieve this goal.

To attain full advantage of testing the PA-PC scheme, one should have interactive access to an established atmospheric circulation model. Running such models is a major project in itself, so we use instead the orographic precipitation model (OPM) described in Chapter III as the reference atmospheric model to develop and implement the methodology. The Sierra Nevada Mountains were the region selected to support our research studies (Fig. 5.7). This choice is justified by the relative abundance of data from a large number of precipitation and streamflow gages which facilitate calibration and validation, and by the topography of the region which is consistent with the assumptions upon which circulation is treated in the OPM. In particular, as described in Section 3.3.2, the length and meridional orientation of the orographic barrier, is assumed to cause traveling air masses to ascend without spilling laterally.

Separate numerical experiments were designed for testing and validating two PA-PC modeling strategies. In the first, a three level finite-element grid with resolution 40, 60 and 80 km was used to simulate precipitation fields. In the second, the orographic precipitation model, operating at 40 km resolution, was coupled to a 1D land-surface energy balance model (LSEBM) operating at 10 km resolution to incorporate the contribution of surface latent heat fluxes into the regional budget of atmospheric moisture. The first experiment was designed to investigate the accuracy of the solutions obtained through AMMs (MS -

multilevel solution) compared to independent unilevel simulations at different spatial resolution frequencies (SS - standard solution), and the computational costs and accuracy tradeoffs between the MSs and SSs of different resolutions. The coupled atmospheric-hydrological experiment was aimed at detecting the contribution of surface latent heat fluxes to the production of orographic precipitation, and the effects of localized recycling of moisture between the land-surface and the atmosphere in mountainous regions, at high elevations.

5.5.1 Case Study I: Disaggregation of the Spatial Distribution of Orographic Precipitation

5.5.1.1 Implementation

In this case study, the implementation strategy consisted of splitting the Eulerian and Lagrangian components of the OPM into two distinct operating modes. The coarse grid resolution level (80 km) was used to solve for transport (Lagrangian mode), while thermodynamics and the physics of precipitation (Eulerian mode) were restricted to the grid level of finest resolution (40 km). Hence, at some reference time t, moist static energy h_M and total water Q were first computed in the 80 km resolution grid and projected onto the 60 km resolution grid; the same process was subsequently repeated between the 60 km and the 40 km grids (Fig. 5.8). According to Eq.(5.8a):

$$h_M \big|_{40}^{\varsigma} = I \big|_{60}^{40} \left(I \big|_{80}^{60} \, h_M \big|_{80}^{\varsigma} \right) \tag{5.20a}$$

$$Q \big|_{40}^{\varsigma} = I \big|_{60}^{40} \left(I \big|_{80}^{60} \, Q \big|_{80}^{\varsigma} \right) \tag{5.20b}$$

where $I \big|_{60}^{40}$ and $I \big|_{80}^{60}$ are disaggregation (prolongation) projection bilinear operators between the 60 km and 40 km, and the 80 km and 60 km grid levels, respectively. The superscript ς refers to the values of h_M and Q being submitted to or resulting from disaggregation. At the finest grid level (40 km), only surface precipitation P was computed, and the values of h_M and Q were updated accordingly. The amount of precipitable water $q_p\big|_{40}$ can be obtained from Eqs. 3.1 through 3.5. $P\big|_{40}$ is then obtained as follows:

$$p\,|_{40}\,(x,y,z,t) = K\,q_p|_{40}(x,y,z,t) \qquad (5.21a)$$

$$P\,|_{40}\,(x,y,t) = \int_H p\,|_{40}(x,y,z,t)\,dz \qquad (5.21b)$$

Due to the modification of qv, q_l and q_i by removal of water through precipitation, new distributions of $h_M|_{40}$ and $Q|_{40}$ are computed by introducing the corrections Δh_M and ΔQ to the corresponding initially disaggregated values :

$$h_M\,|_{40} = h_M|_{40}^{\varsigma} - \Delta h_M \qquad (5.22a)$$

$$Q|_{40} = Q\,|_{40}^{\varsigma} - \Delta Q \qquad (5.22b)$$

The updated values of qv, h_M and Q are aggregated to the 80 km grid level to reinstate both initial and boundary conditions for the next time-step $(t+\Delta t)$:

$$h_M\,|_{80} = I\,|_{60}^{80}\,(I\,|_{40}^{60}\,h_M|_{40}) \qquad (5.23a)$$

$$Q\,|_{80} = I\,|_{60}^{80}\,(I\,|_{40}^{60}\,Q|_{40}) \qquad (5.23b)$$

$$qv\,|_{80} = I\,|_{60}^{80}\,(I\,|_{40}^{60}\,qv|_{40}) \qquad (5.23c)$$

where $I\,|_{60}^{80}$ and $I\,|_{40}^{60}$ are aggregation (restriction) projection operators between the 60 km and 80 km, and the 40 km and 60 km grid levels, respectively. Only two groups of variables are treated independently in this particular application, and therefore only two grid levels (the 40 km and 80 km resolution levels) are necessary for a strictly formal application of the AMM methodology. The intermediate 60 km grid level is used, however, in this case to increase the amount of information retained in the projection of h_M and Q between the 40 and 80 km grid levels. The intergrid transfers across grid levels can be repeated at each time-step, or at intervals consistent with the updating of boundary conditions.

5.5.1.2 Results

The study was carried out for a region comprising the Northern and Central Sierra Nevada Mountains between latitudes 38°N and 40°N. Boundary conditions were extrapolated from the four-hour radiosonde data collected at Oakland (Fig. 4.3). To verify and validate the scheme, both point values at the location of selected precipitation gauges (Fig. 5.9a), and the spatial distribution of precipitation in the American River Basin (Fig. 5.9b) were used. A summary of the names and locations of the precipitation stations is presented in Table 5.2. Model simulations were produced for the fall, winter and spring seasons (September 15th through May 15th) of the 1986-87 and 1987-88 water-years.

To facilitate the comparison among solutions with and without multilevel implementation, an accuracy measure to calculate the relative improvement in the accuracy of simulated monthly precipitation (RIAMP) at each location was established. The measure was defined as the ratio of the difference between the absolute values of the errors of the multilevel solution (MS) Υ_{m} and the standard solution (SS) Υ_{s}, divided by Υ_{s}:

$$\mathrm{RIAMP} = \frac{\Upsilon_{\mathrm{m}} - \Upsilon_{\mathrm{s}}}{\Upsilon_{\mathrm{s}}} \tag{5.24}$$

where Υ is the difference between observed and predicted precipitation rates.

Data analysis focused on evaluating: 1) the RIAMP when the MS at 80 km (MS80) is compared with the SS at the same resolution (SS80); 2) the similarities between the spatial patterns in the precipitation distributions produced by MS80 and those produced by SS40 and SS80. In addition, MS80 was compared with SS40 by computing the difference error $\Delta\Upsilon$ for storms with total precipitation amounts equal to, or larger than 26 mm day-1:

$$\Delta\Upsilon=\Upsilon_{\mathrm{m}} \,|^{80} - \Upsilon_{\mathrm{s}} \,|^{40} \tag{5.25}$$

Table 5.3 summarizes the RIAMP values computed at the location of the precipitation stations in Table 5.2. Overall, the solution improves as a result of the multilevel scheme. The greatest improvements were found although best results were found at low elevations (e.g. stations 13, 16, 18, 19) and at high elevations on steep slopes (e.g. stations 3 and 7) for which RIAMP values often exceed 20 percent. This can be explained by noting that where large-scale forced ascent is the leading mechanism in the formation of clouds and the generation of precipitation, spatial resolution appears to be a secondary factor in the forecast of rain or snowfall, as long as the regional orographic slope is preserved adequately at the spatial resolution of choice (this is the case for both the 40 and 80 km resolution grids). However, at low elevations, where the orographically induced production of precipitation weakens dramatically, and to leeward of orographic crests, where the lower troposphere is warmer and drier due to upwind depletion of atmospheric moisture, the model exhibits higher sensitivity to small scale topographic features (e.g. short hills and hidden valleys). Stations located on areas with weak orographic gradient display significantly less improvement (e.g. stations 20, 22, 25, 26). Also, as to reiterate the conclusions in Section 4.3 concerning the performance of the OPM for dry versus wet conditions, the results are better for the simulations of the 1987-88 water-year, which is much drier than 1986-87.

Spatial distributions of precipitation associated with MS80, SS80 and SS40 for the American River Basin are shown in Figs. 5.10a and 5.10b respectively for the 22nd and the 23rd of January, 1987. The contoured precipitation maps show clearly that MS80 patterns are qualitatively closer to the features of SS40 than those of SS80. This is detected with respect to both the prediction of the location of precipitation peaks and respective peak amounts, as well as to the general pattern of precipitation fields across the landscape.

The computational savings which result from using MS80 instead of SS40 amounted to 39 percent of CPU run-time units. On the other hand, the additional costs of MS80 as compared to SS80 were only 3 percent. Table 5.4 illustrates the decrease in forecasting accuracy of MS80 relative to the SS40 for storms characterized by daily precipitation rates equal to or exceeding 26 mm day^{-1}. For the most part, the losses of accuracy remain well below 30 percent, which is an acceptable value for long-term, macroscale hydroclimatological studies, and even for many mesoscale meteorological applications (Tolby Carlson, personal communication).

5.5.2 Case Study II: Incorporation of Surface Latent Heat Fluxes into the Regional Budget of Atmospheric Moisture

For this case study, we focus on three spatial scales: a synoptic scale, or more specifically the spatial length at which radiosonde data are representative of large-scale atmospheric fields (hundreds of kms); the mesoscale, understood as a characteristic length at which orographic effects upon precipitation initiation and duration prevail and at which the phenomena can be modeled adequately (40 km for the Sierra Nevada mountains); and, the field scale, an upper-bound length scale appropriate for describing land-surface processes (≤ 10 km).

In the context of AMMs, the PA-PC strategy incorporates the following assumptions. First, only those processes which play an important role in the intra-annual variability, orographic forcing and constraints on precipitation and energy balances, are included, while we neglect lower frequency phenomena such as groundwater flow. Second, for the time scales of interest, land-atmosphere interactions have a negligible influence on the fate of synoptic weather systems, and therefore these can be restricted to meso- and field scales. The interactive coupling is effected through precipitation and dew formation in the surface model (the land-surface act as a sink of atmospheric water), and through the introduction of evapotranspiration fluxes as a source term in the atmospheric equation of total water balance (the atmosphere acts as a sink with respect to evaporative fluxes from the land-surface). The mass balance is:

$$\frac{\mathrm{DQ}}{\mathrm{Dt}} = \mathrm{S(p)} + \frac{\phi_h}{\rho \mathrm{L}} \tag{5.26}$$

where Q is total water, S(p) describes the scavenging of precipitable water, ϕ_h is the latent heat flux at the land-atmosphere interface, and L is the latent heat of vaporization of water having density ρ.

The Land Surface Energy Balance Model (LSEBM) is a variation of the model used by the European Center for Medium Range Weather Forecasts (ECMWF) model as described by Blondin (1991), and consists of three major parts: an energy balance model; a mass balance model to solve for runoff, soil moisture and soil temperature; and a snowmelt model (Fig. 5.11). The differences between our LSEBM and the ECMWF surface module are in the formulation of the radiative forcing sub-model, in the description of the soil column (our scheme has only two layers while the ECMWF model has three layers, and we neglected diffusive terms in the equations of heat and mass conservation), and the inclusion of saturation overland flow and baseflow terms in the surface water budget. A column composed of an atmospheric boundary layer and two soil layers is attributed to each nodal position of the surface layer in a finite-element grid, and a 1D implementation of the model is applied to each column (Fig. 5.12). Two-dimensional spatial distributions are obtained by interpolation among the nodal values in the finite-element grid.

5.5.2.1 Implementation

Upper air initial and boundary conditions used to force the atmospheric model were extracted from the Oakland radiosonde data archive. ECMWF TOGA (Tropical Oceans Global Atmosphere) surface boundary layer data were used for the initialization of the land-surface and planetary boundary layer portions of the 3D study domain. Albedo and leaf area index (LAI) at each node of the 10 km grid were inferred from satellite infrared imagery. Roughness distributions were inferred based on topography, vegetation cover and status of vegetation growth, which can be indirectly established based on LAI distributions.

Because precipitation and latent heat exchange are mutually dependent non-linear variables, the simultaneous solution of the coupled equations in the land-surface and atmospheric models is not possible. We sidestep this difficulty by accepting asynchronism in the incorporation of the feedbacks, and by assuming that, for short time-steps ($\leq$ 1 hour), the processes involved are stationary, and their interdependences are linear. From a practical standpoint, this results in computing precipitation rates which are then used to drive the surface model and subsequently produce latent heat fluxes. The moisture associated with the latent heat fluxes is part of the atmospheric moisture supply for the next time-step.

At a given instant, the disaggregated values of precipitation P and specific humidity q_v used as surface boundary conditions in the LSEBM are obtained by projecting the solutions from the 40 km atmospheric grid level onto the 10 km surface grid as indicated by Eq.(5.8a):

$$\mathrm{q}_v\big|_{10}^{\varsigma} = I\,\big|_{40}^{10}\ \mathrm{q}_v\big|_{40}^{\varsigma} \tag{5.27a}$$

$$\mathrm{P}\big|_{10}^{\varsigma} = I\,\big|_{40}^{10}\ \mathrm{P}\big|_{40}^{\varsigma} \tag{5.27b}$$

where $I\big|_{40}^{10}$ is the disaggregation projection operator between the 40 km resolution atmospheric grid and the 10 km resolution surface grid.

From Eq.(5.10), aggregation to the atmospheric model of the 2D distributions of surface latent heat flux predicted by the LSEBM leads to the modification of the coupled solution for specific humidity $\mathrm{qv}\big|_{40}^{C}$ as follows:

$$\mathrm{qv}\big|_{40}^{C} = \mathrm{qv}\big|_{40} + I\,\big|_{10}^{40}\,\big(\frac{\phi_h}{\rho \mathrm{L}}\big)\big|_{10} \tag{5.28}$$

where $I\big|_{10}^{40}$ is the aggregation projection operator between the 10 km resolution surface grid and the 40 km resolution atmospheric grid. The distributions of $\mathrm{h_M}$ and Q are updated to reflect the new humidity field, and the OPM simulation proceeds for the next time-step.

5.5.2.1 Results

Following the approach of Chapter III, streamflow data were used to validate hydrologically the areally integrated values of precipitation for the American River basin. In addition, predicted snow cover extent was carried out by compared with satellite imagery indices of snow cover. Due to the limited time period for which satellite snow cover data were available, verification of model results was carried out for the winter and spring seasons of 1990 only. The winter and spring provided two periods of very different hydrological activity: one of heavy rain and snowfall (winter), and another of progressive snowmelt (spring). Table 5.5 shows the results of the validation with respect to estimated runoff, which indicate excessive snowmelt (24 percent error) during March, although the mass balance closes with a 3 percent error by the end of April. The performance of the coupled atmospheric-hydrological model is best illustrated in Figs. 5.13a and 5.13b, which allow comparison of the spatial distribution of snow cover predicted by the model and the corresponding satellite images, respectively for the 26th of February and the 1st of May .

Analysis of the spatial distribution of precipitation with and without the latent heat flux feedback showed no detectable differences between SS40 and MS80. This is due to the strong influence of the synoptic circulation, which smooths out what may be strong localized contributions of moisture from the land-surface. The exchange of latent heat flux was evident in the characteristics of low level (between 1000 and 850 hPa) specific humidity profiles, which in turn may affect the estimation of cloud depth and cloud cover extent in the lower troposphere. At high elevations, the persistence of the signature of latent heat exchange between the land-surface and the atmosphere is limited to the daily time-scale due to the strength and controlling role of solar radiation in the energy budget. By contrast, in the irrigated fields of the Sacramento/San Joaquin Valley, these effects are expected to be stronger, and may ignite and sustain mesoscale convective circulations (Avissar and Pielke 1989, Pielke et al. 1991, caramori et al. 1993).

The feedbacks of local mesoscale circulations associated with the spatial variability of latent and sensible heat fluxes as they affect the dynamics of the planetary boundary layer (PBL) have been neglected here. In contrast to previous mesoscale studies of land-atmosphere interactions (e.g. Pielke et al. 1991) which have concentrated only on short-term sensitivity studies of mesoscale forcing-response relationships, our approach represents an advance in that it allows the examination of long-term behavior of the land-atmosphere system.

Table 5.1 Mean annual properties of hourly precipitation in California for precipitation stations located above 1000 m MSL and with total annual precipitation $\geq$ 500 mm.

Number of rainy days (daily precipitation > 0.25 mm)	71
Number of rainy days during which daytime values exceed 70 percent of the daily total precipitation	50
Mean Annual Precipitation	1036
Mean Annual Precipitation [06:00 - 10:00]	135
Mean Annual Precipitation [10:00 - 16:00]	425
Mean Annual Precipitation [16:00 - 19:00]	186
Mean Annual Precipitation [19:00 - 06:00]	290

Table 5.2 Identification and geographical locations of the precipitation stations used to test and verify the AMM applications to the Northern and Central Sierra Nevada Mountains.

Station	Name	Latitude (°N)	Longitude (°W)	Elevation (m)
1	Blue Canyon	39:17	120:42	1609
2	Bowman Dam	39:27	120:39	1635
3	Bridgeport	38:15	119:14	1972
4	Calaveras Big Trees	38:17	120:19	1431
5	Calistoga	38:34	122:35	113
6	Challenge	39:29	121:13	783
7	Chico Univ. Farm	39:42	121:49	58
8	Colfax	39:06	120:57	735
9	Deer Creek Forebay	39:18	120:50	1359
10	Downieville	39:34	120:50	890
11	Echo Summit	38:47	120:02	2240
12	Electra	38:20	120:40	219
13	Gold Run	39:09	120:52	1012
14	Grass Valley	39:13	121:04	732
15	Graton	38:26	122:52	61
16	Lake Spaulding	39:19	120:38	1573
17	Lodi	38:07	121:17	12
18	Potter Valley	39:22	123:08	311
19	Sagehen Creek	39:26	120:14	1932
20	Sierra City	39:34	120:38	1289
21	Sierraville	39:35	120:22	1518
22	Strawberry Valley	39:34	121:06	1161
23	Truckee	39:20	120:11	1835
24	Woodfords	38:47	119:49	1728

Table 5.3 Summary of RIAMP values (Eq. 5.24) computed for the locations of the precipitation stations presented in Table 5.2 and for the fall, winter, and spring seasons corresponding to water-years 1986-87 and 1987-88.

Station	RIAMP-86/87 (%)	RIAMP-87/88 (%)
1	3.7	11.6
2	2.4	9.8
3	64.0	11.6
4	16.8	36.5
5	31.0	50.1
6	8.7	12.1
7	81.4	47.3
8	13.6	14.0
9	8.1	16.7
10	5.3	11.3
11	4.6	9.5
12	7.4	15.8
13	16.5	34.6
14	3.2	8.3
15	13.1	34.6
16	10.8	33.7
17	2.7	11.6
18	26.6	46.6
19	20.2	24.7
20	0.1	5.2
21	1.9	8.2
22	0.1	5.2
23	7.2	37.8
24	6.6	11.2
25	0.1	5.6
26	0.1	6.7

Table 5.4 Summary of the difference error $\Delta\Upsilon$ (Eq. 5.25) between the MS at 80 km resolution and the SS for storms with total precipitation amounts $\geq$ 26 mm day-1 for the stations of Table 5.2.

Station	$\Delta\Upsilon$ (%)
1	7.0
2	15.0
3	22.0
6	26.0
8	33.0
9	29.0
10	20.0
11	20.0
12	29.0
13	26.0
15	22.0
18	27.0
19	27.0
20	19.0
22	32.0
23	44.0
24	63.0

Table 5.5 Comparison between observed and simulated runoff values in the American River basin, during winter 1990.

Date	Observed (m^3)	Simulated (m^3)	Error (%)
1/1 - 3/1	$250.6\text{x}10^6$	$283.5\text{x}10^6$	13.0
3/1 - 4/1	$224.2\text{x}10^6$	$278.5\text{x}10^6$	24.0
4/1 - 5/1	$165.7\text{x}10^6$	$170.6\text{x}10^6$	3.0

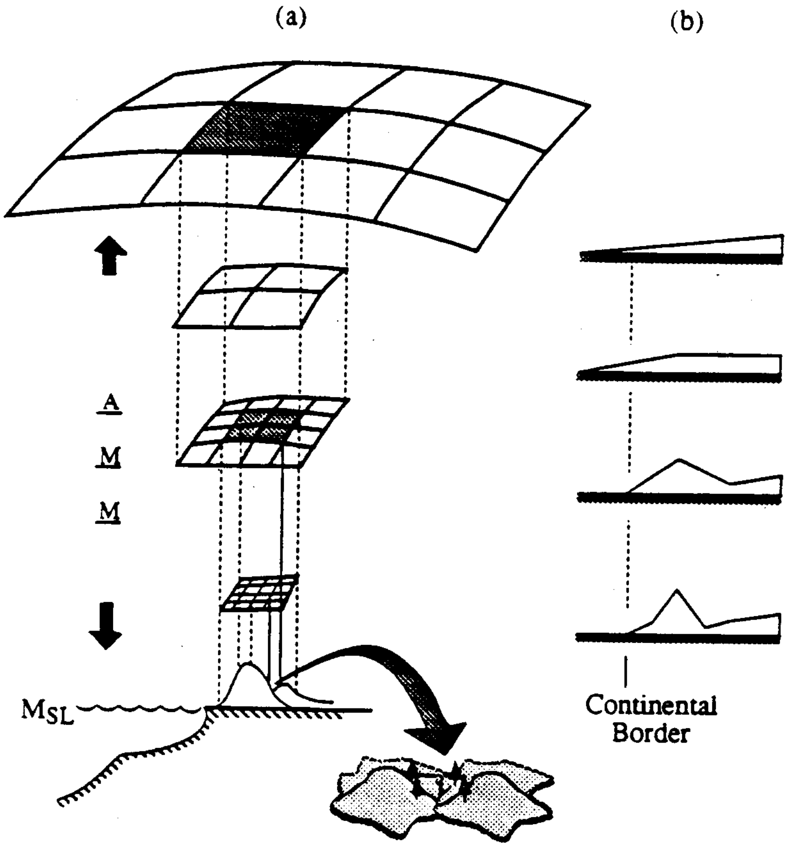

Figure 5.1 Adaptive multigrid implementation for a stylized representation of the Olympic Mountains: a) computational grid; b) West-East land profiles for each grid. [AMM - Adaptive Multilevel Method; GCM - General Circulation Model; RM - Regional Model; MSL - Mean Sea Level].

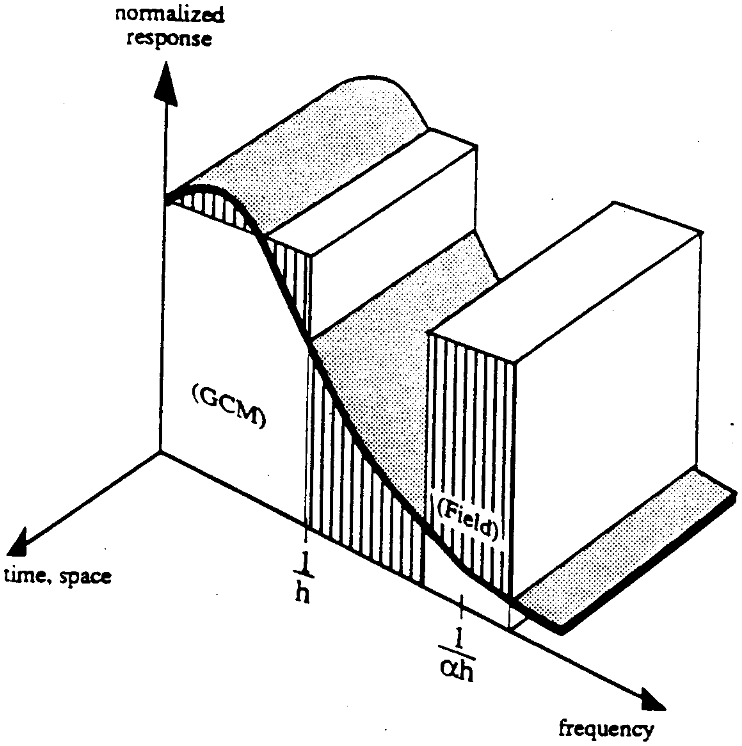

Figure 5.2 Filter analogy representation of GCMs. The areas shaded with vertical lines correspond to errors in the GCM solution. Our assumptions are: (a) the volume of the portion of the GCM solution between the windows located at frequencies 1/h and $1/\alpha$h is of the order of TEK1; (b) for scales smaller than αh, the errors can be ignored; (c) AMMs provide means to compute the error associated with the bandpass filter entered at $1/\alpha$h.

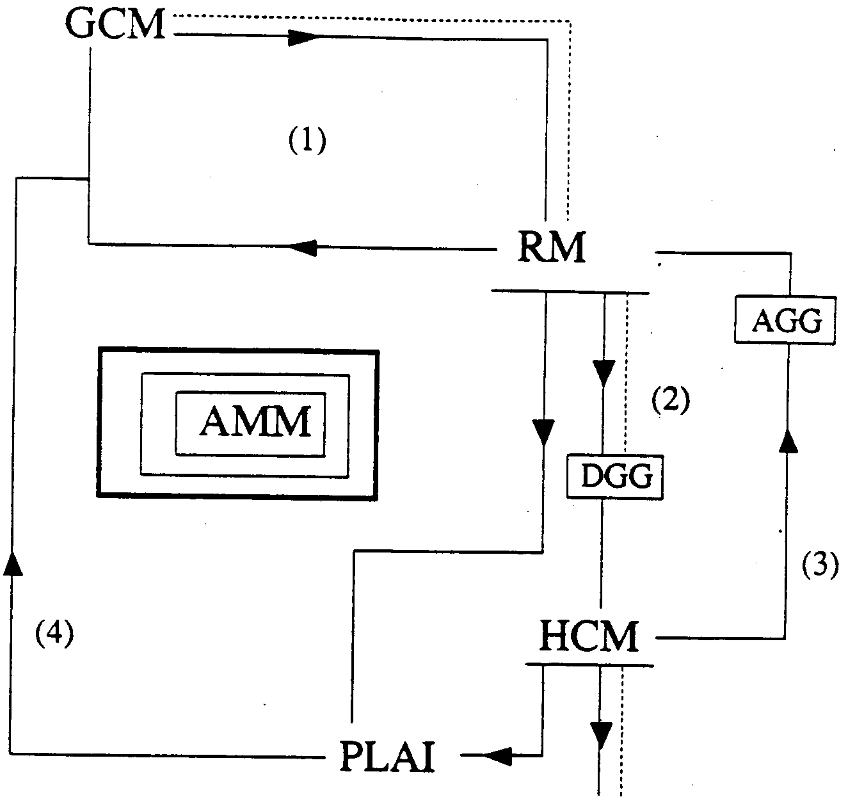

Figure 5.3 Schematic of Adaptive Multilevel Modeling strategies (AMMs) for coupling models at different scales. (RM - Regional Model; HCM - Hydroclimatological Model; PLAI - Parametrization of Land-Atmosphere Interactions; DGG - Disaggregation; AGG - Aggregation). The schemes are: (1) full approximation-full coupling (FA-FC); (2) partial approximation- no coupling (PA-NC); (2) & (3) partial approximation and partial coupling (PA-PC); and (4) full approximation - partial coupling through parameterization of land-surface processes.

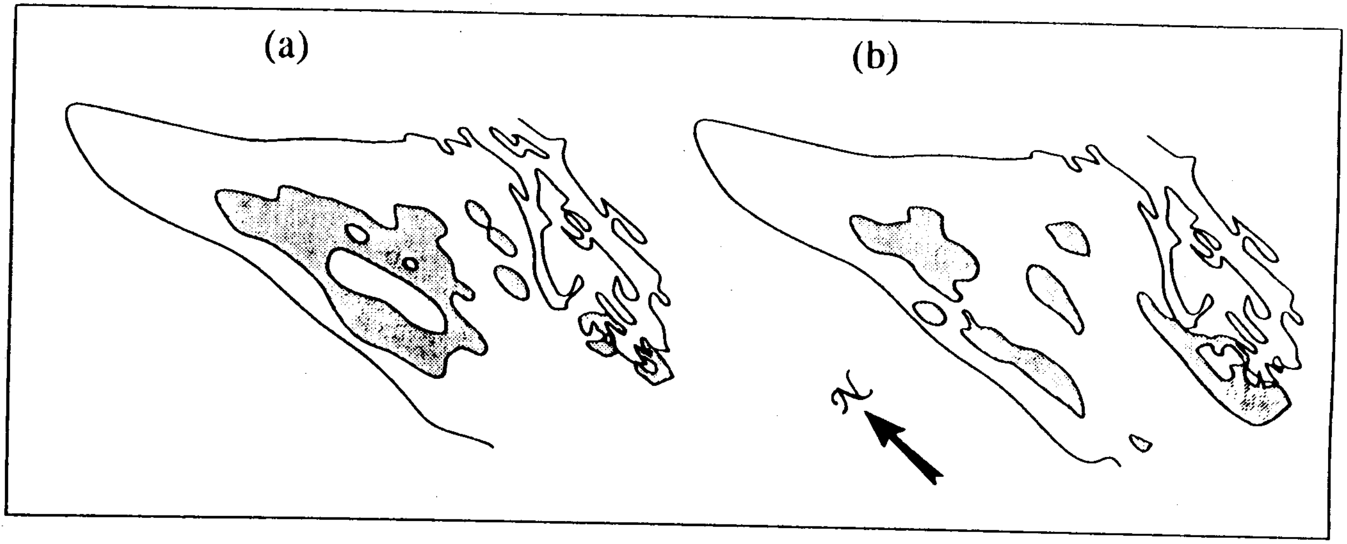

Figure 5.4 Spatial distribution of the updrafts associated with a southwesterly storm approaching the Olympic Mountains with velocity U:
a) before vorticity correction [case P]; b) after vorticity correction [case R].

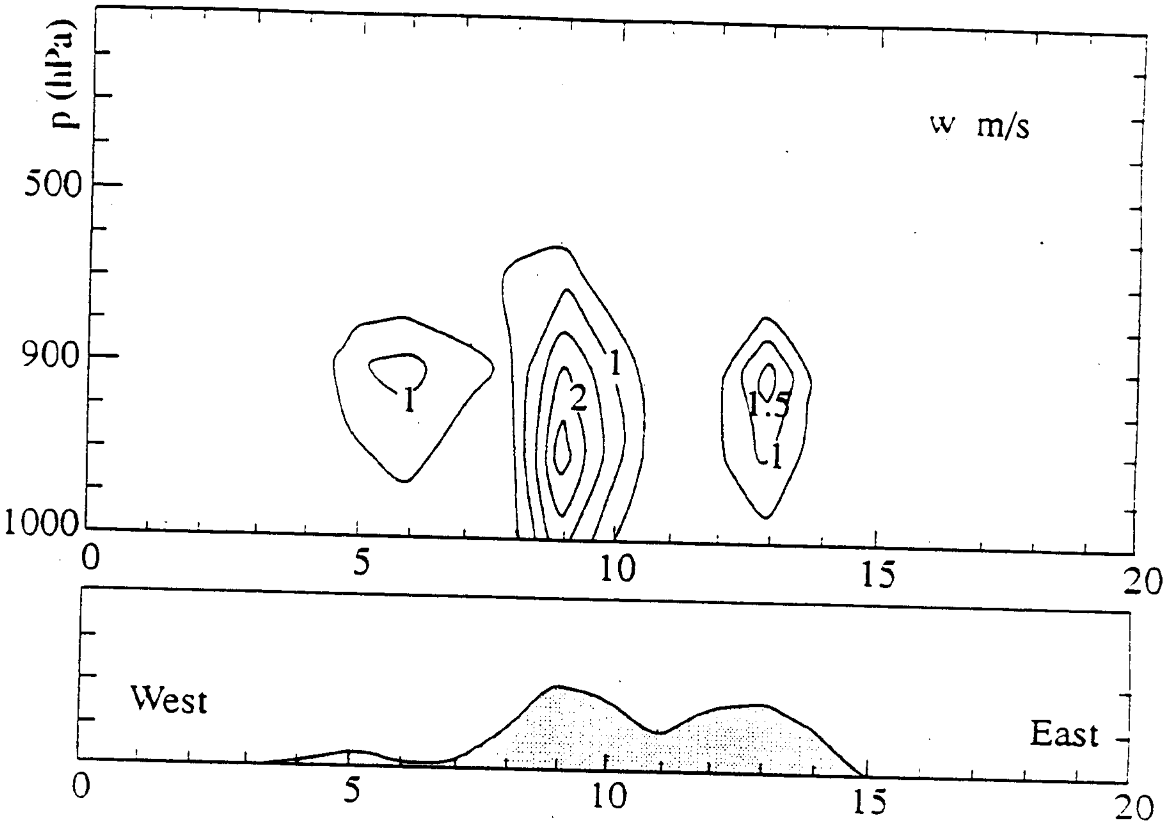

Figure 5.5 a)Vertical distribution of vertical velocities along the profile W-E and the storm marked in Fig. 5.5a before vorticity correction [case P]. The normalized transversal profile of the mountain along the cut W-E is displayed in the lower side of the plots.

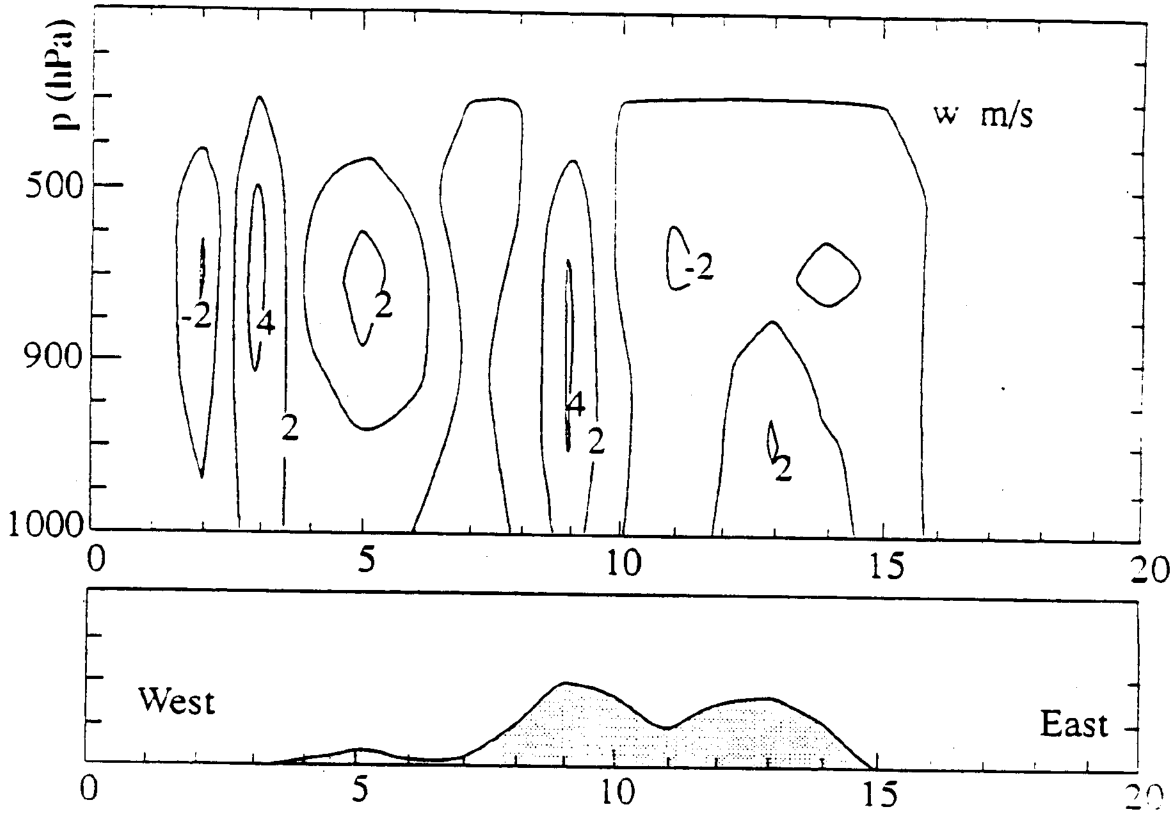

Figure 5.5 b)Vertical distribution of vertical velocities along the profile W-E and the storm marked in Fig. 5.5a after vorticity correction [case R]. The normalized transversal profile of the mountain along the cut W-E is displayed in the lower side of the plots.

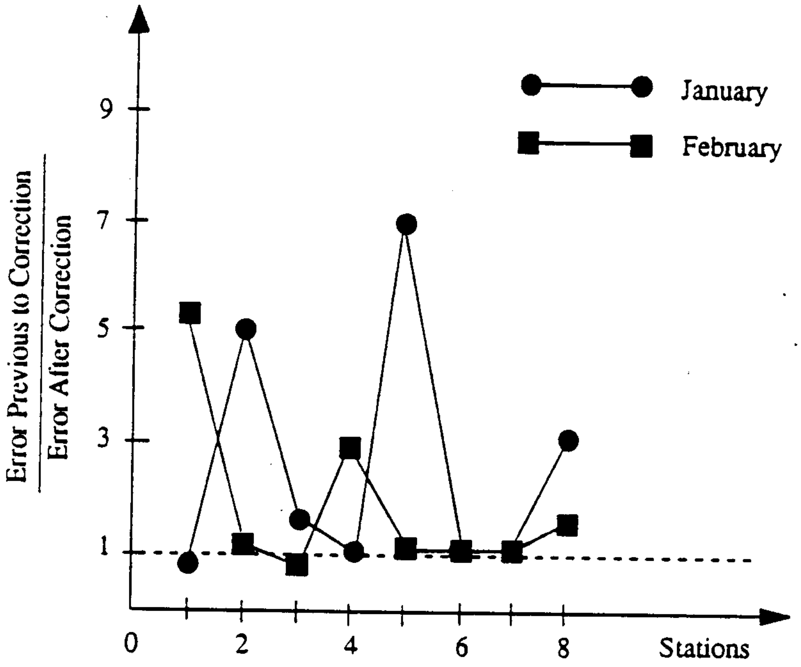

Figure 5.6 Relative change of the simulation errors at the precipitation gages with respect to monthly precipitation values in January and February of 1967. Values greater than one indicate improvement.

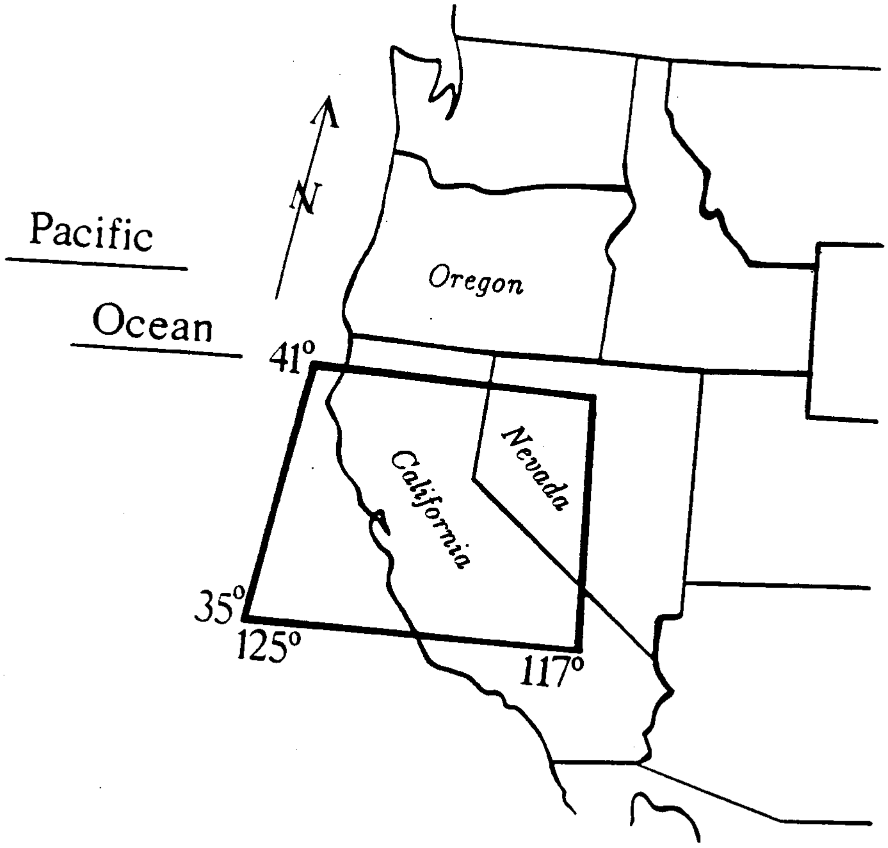

Figure 5.7 Map of the location of the study domain window for the Sierra Nevada Mountains.

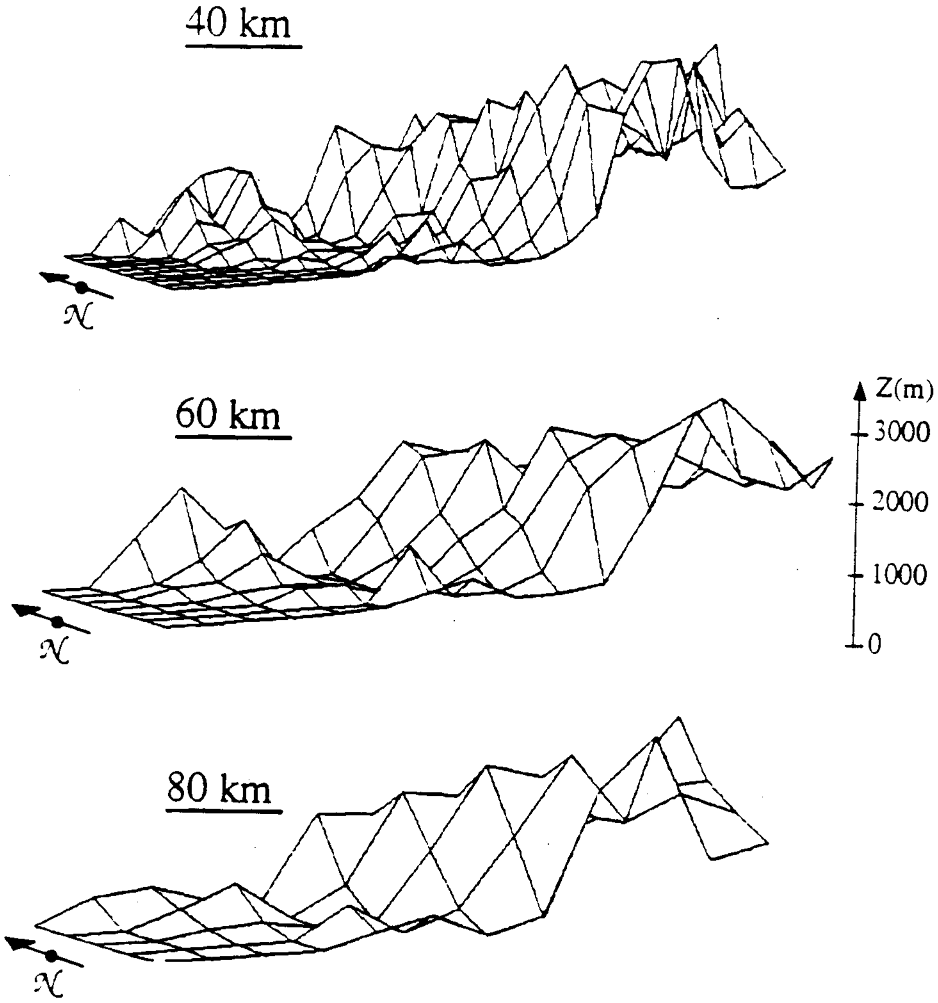

Figure 5.8 Three level finite-element grid (40, 60 and 80 km discretization spacing) for the application of the PA-PC scheme to portion of the Sierra Nevada Mountains corresponding to Fig. 5.7.

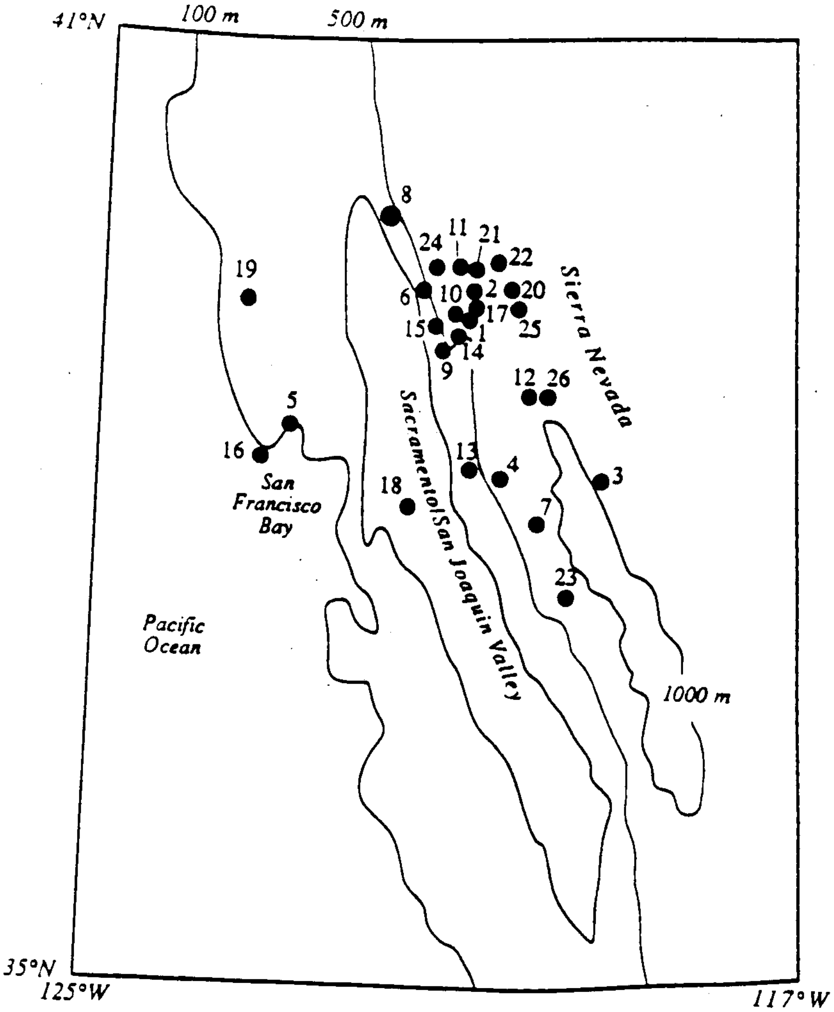

Figure 5.9 a) Topographic map showing the location of the precipitation gages listed in Table 5.2.

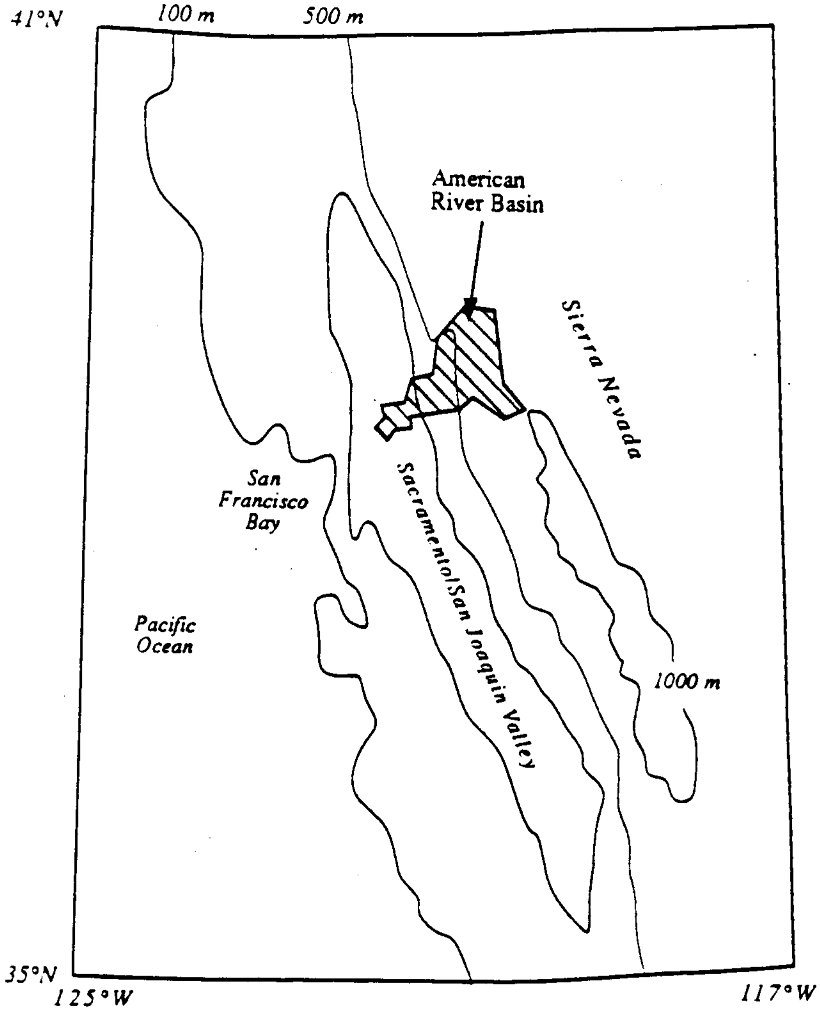

Figure 5.9 b) Topographic map showing the location of the American River basin.

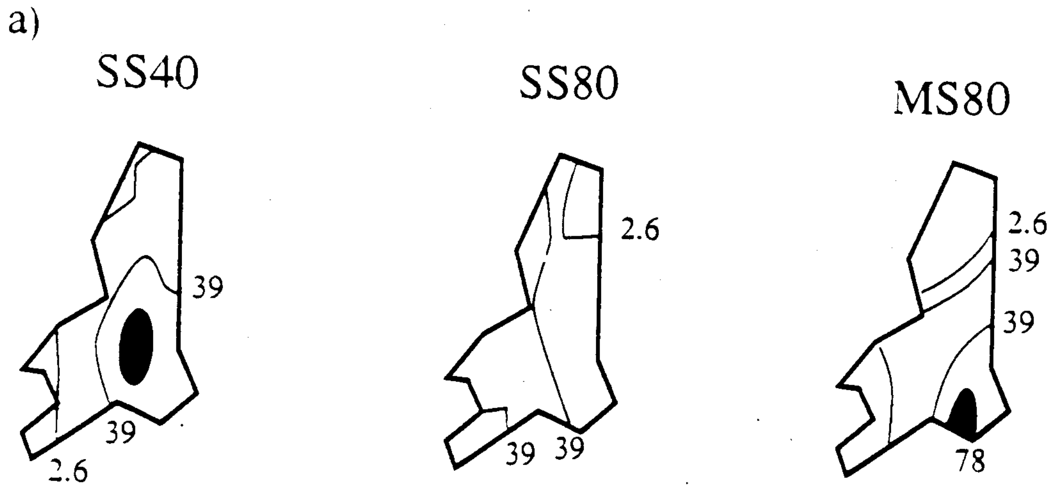

January 22, 1987

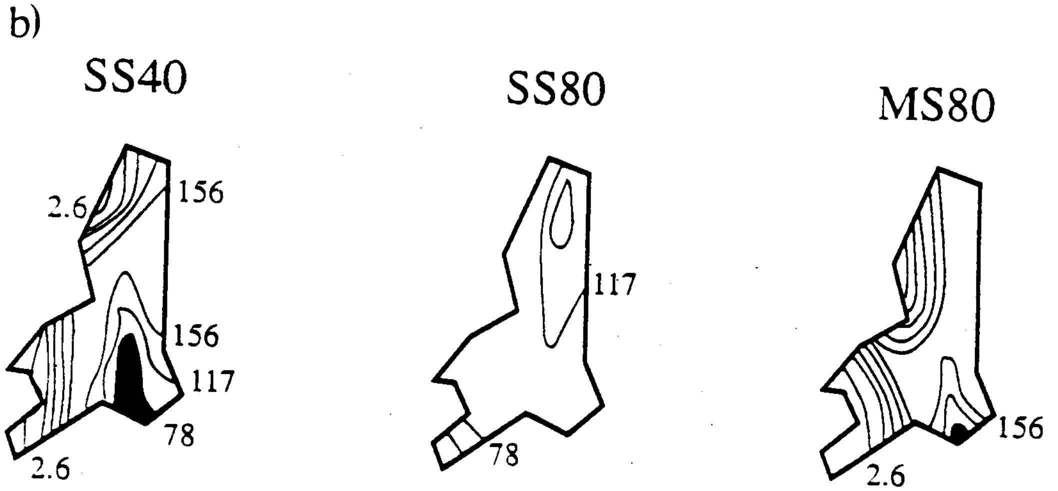

January 23, 1987

Precipitation (mm)

Figure 5.10 Spatial distribution of precipitation in the American River basin as obtained from SS40, SS80 and MS80 simulations: a) 22nd, January 1987; b) 23rd, January 1987.

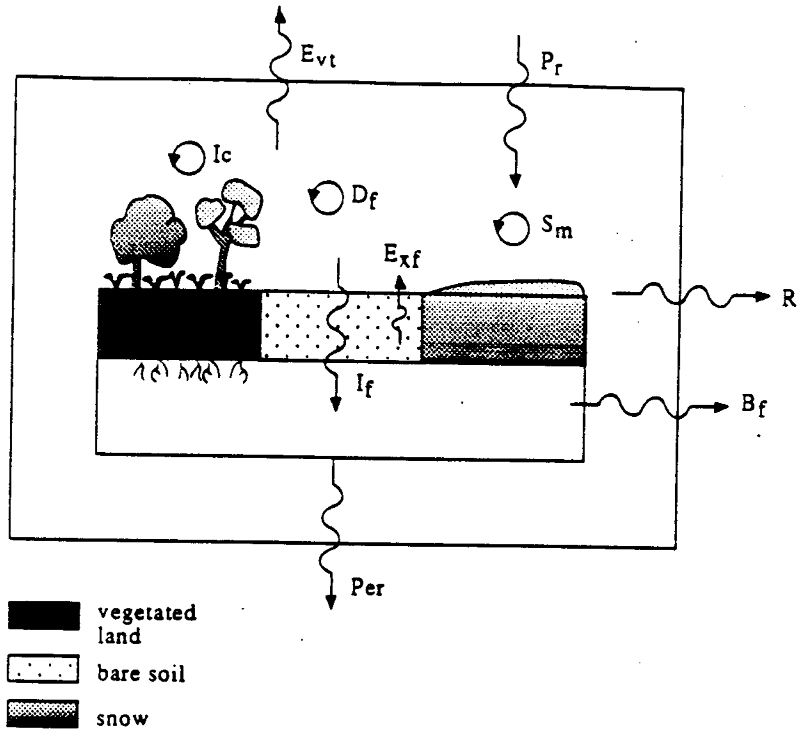

Figure 5.11 Conceptualization of the physical processes described by the surface energy model at a point. Nomenclature: E_{vt} - Evapotranspiration; P - Precipitation; I_c - Interception; D_f - Dew Formation; S_m - Snowmelt; E_{xf} - Exfiltration; R - Runoff; I_f - Infiltration; B_f - Baseflow; P_{er} - Deep Percolation.

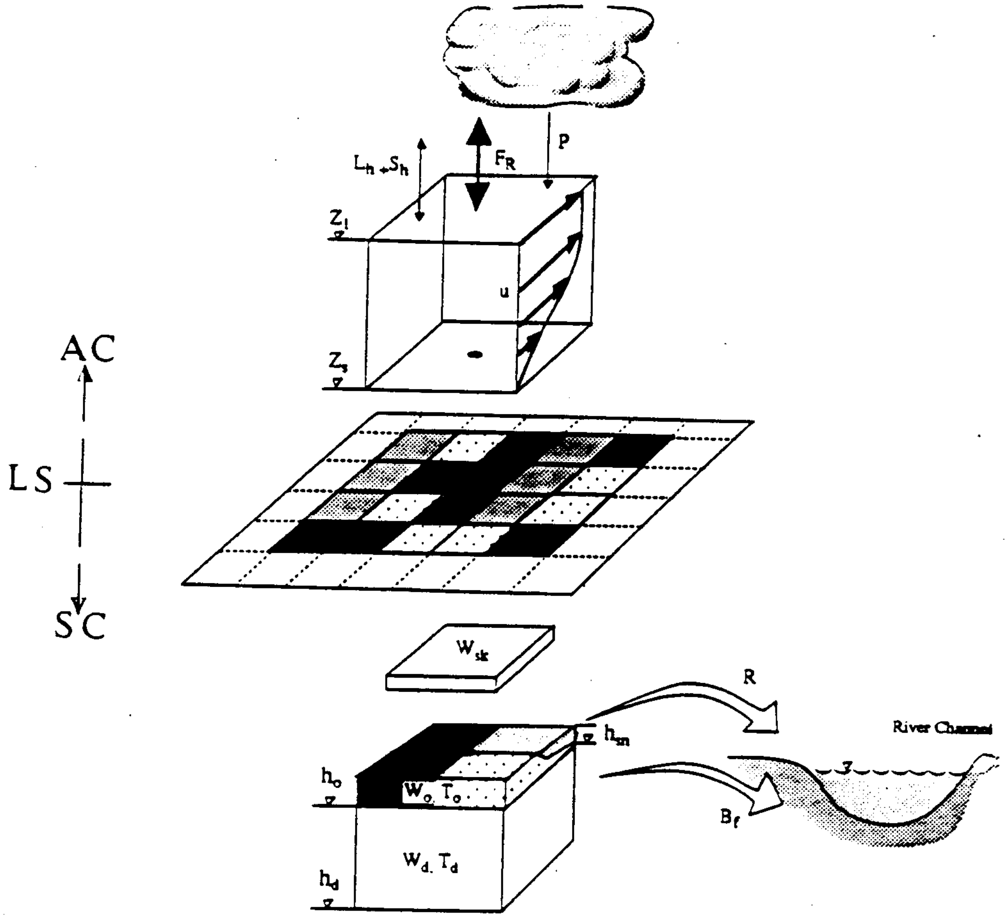

Figure 5.12 Conceptualization of the surface energy model: to each node of the finite-element grid which represents the land surface (LS), an atmospheric column (AC) and a soil/vegetation column (SC) are attributed. The exchange of mass and energy between the land surface and the atmosphere is carried out by the precipitation P, latent heat L_h, sensible heat S_h and net radiation F_R fluxes across the interface column AC. The heat and mass transfer model applied to the soil column SC allows the estimation of soil moisture, snow depth, and runoff among other hydrological variables. Runoff and baseflow are dumped to the outlet of the basin.

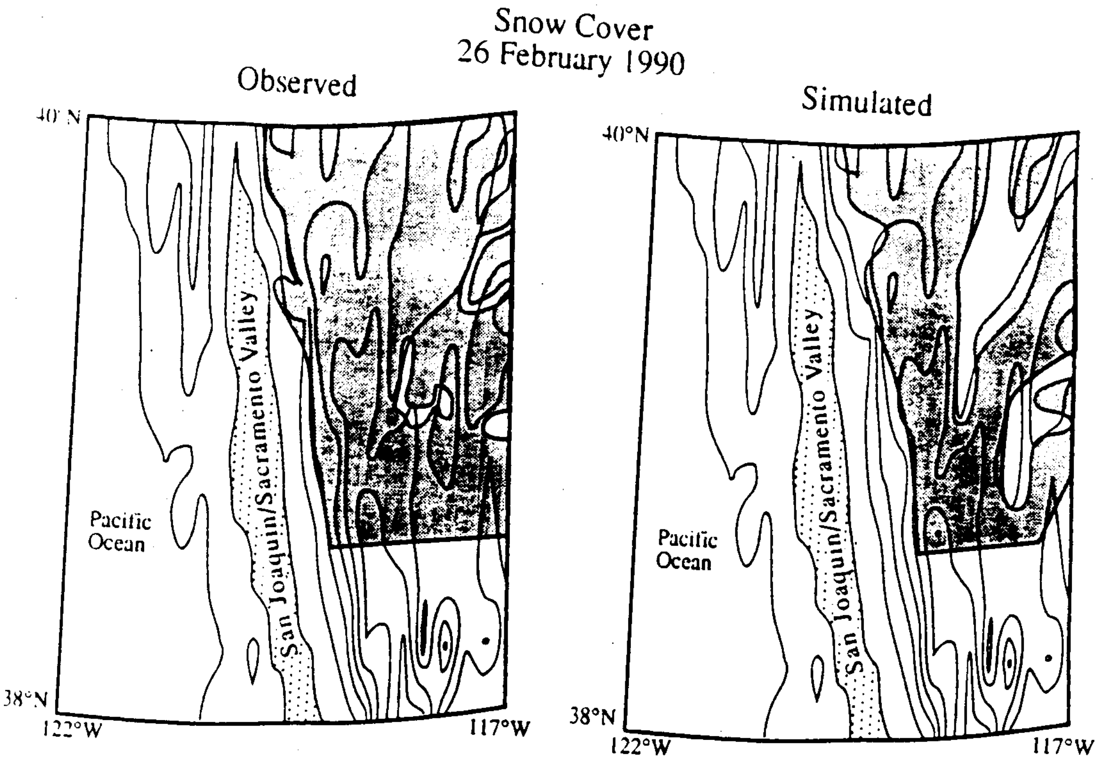

Figure 5.13 a) Snow cover distributions for February 26th, 1990: observed (satellite image, 10 km pixel size) and simulated (coupled atmospheric-hydrological models, two-level grid with 40 and 10 km resolutions).

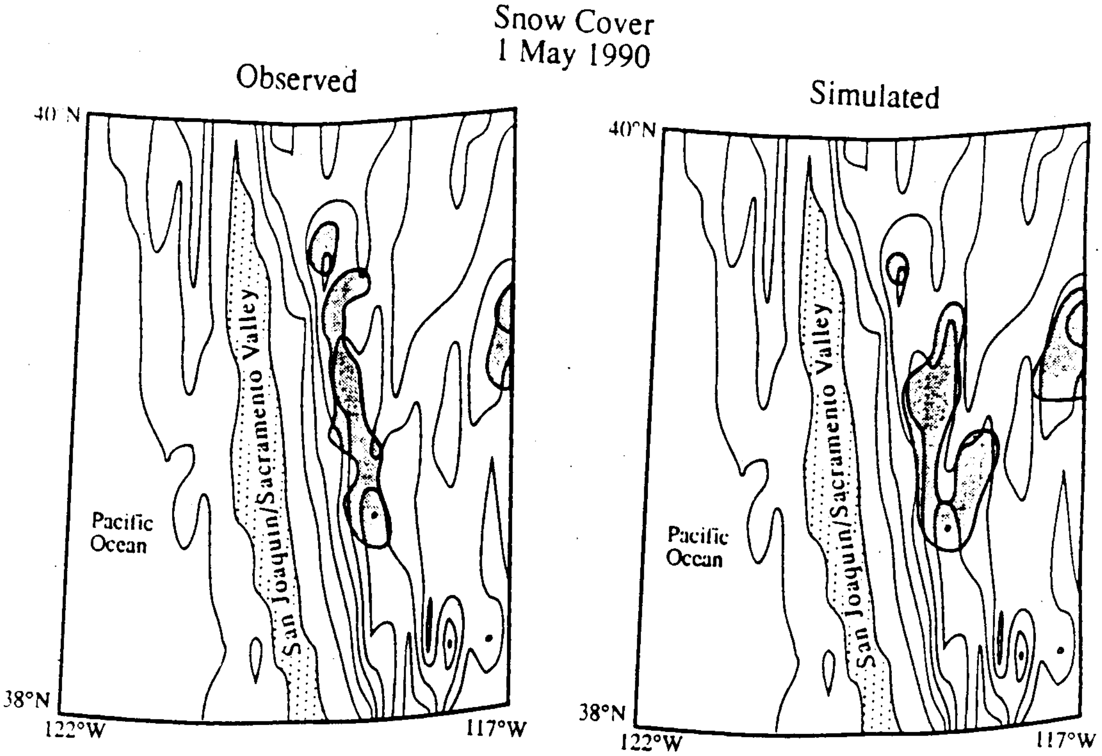

Figure 5.13 b) Snow cover distributions for May 1st, 1990: observed (satellite image, 10 km pixel size) and simulated (coupled atmospheric-hydrological experiment, two-level grid with 40 and 10 km resolutions).

CHAPTER VI - SUMMARY , CONTRIBUTIONS, AND RECOMMENDATIONS FOR FUTURE WORK

"Everything we see is something besides."

Fernando Pessoa, Notes for a Faust Play, 1932

6.1 Summary

Until recent years, hydrologic and climatologic modelers have worked independently. The need to address questions of climate change and the effects of climate variability on terrestrial and aquatic ecosystems is, however, bringing the two modeling communities together. Part of the comprehensive modeling activity involves representing the spatial variability of precipitation in regions of complex orography, and developing aggregation and disaggregation techniques to describe multiscale pathways of the hydrological cycle.

One approach to comprehensive modeling has been to combine separate descriptions of physical processes into holistic models that require the specification of a large number of empirical parameters. Many of these parameters are impossible or difficult to estimate adequately, and their interdependence for changing environmental conditions is not well understood. In the work reported here an alternative approach was pursued. For well defined orographic conditions, complex natural phenomena were expressed in terms of principal governing processes at the dominant spatial and temporal scales. The strategy was both to represent localized phenomena and to investigate the validity of process representation and the interactions among such processes. Information exchange among scales was achieved by implementing adaptive multilevel schemes.

In this context, a model to simulate regional distributions of orographic precipitation was developed. The model was implemented using a 3D finite-element grid with six vertical layers defined between the 1000 and 250 hPa pressure levels. The model has two parts: (1) an independent circulation module designed to be used as a dynamic interpolator of synoptic wind fields from the macroscale (100's of km) to the mesoscale (10's of km); and (2) a Lagrangian transport module that moves moisture across the study domain and tracks the formation and growth of clouds and the generation of precipitation. The transport module is based on the assumption of adiabatic rising and falling of individual air parcels, and treats total water and moist static energy as conservative substances. Mass and energy are depleted by precipitation alone. Rain and snowfall rates are proportional to the instantaneous amounts of liquid water and ice, respectively, in the atmospheric column. Precipitation rates are a function of a spatially varying precipitation efficiency parameter that requires calibration. An evaporative cooling scheme to account for phase and mass exchanges between settling hydrometeors and low-level atmospheric layers was developed and implemented. The model was used to simulate spatial precipitation patterns in the Olympic and the Sierra Nevada Mountains in the Western U.S..

In addition, a method for adaptive multilevel coupling of land-atmosphere interactions was developed. Adaptive multilevel methods allow full coupling of atmospheric and land-surface hydrological models by preserving consistency between the large-scale (atmospheric) and the regional (land) components. The approach is a numerical analog of a telescope. A macroscale host grid to cover the region of interest (analogous to the view at lowest telescope resolution) and patches of client grids (analogous to the view at increased resolution) nested within and contained by the host grid were created. Each client grid was used to solve subgrid scale processes whose contributions are relevant within a narrow range of spatial frequencies. Interscale transfers were carried out by bi-linear interpolation. The methodology was investigated for three case studies involving the coupling of models with different levels of complexity and different spatial resolutions.

The first case study consisted of coupling two simple models. One model provided the potential and the other the rotational components of atmospheric wind fields. The resulting wind fields were used to drive the orographic precipitation model. This methodology was applied to predict precipitation for the Olympic Mountains, in Washington State, with special attention given to stations leeward of the crest. The orographic precipitation model gave, in this case, better results than previous modeling efforts.

The model's ability to produce detailed spatial distributions of precipitation was tested by solving for advective transport at coarse spatial resolution and restricting precipitation processes to finer resolution. In this second case-study, intermittent coupling (every 4 hours) of three versions of the orographic precipitation model operating at 40, 60 and 80 km resolution, respectively, was established to replicate the precipitation patterns of specifically chosen storms as they evolved across the Central Sierra Nevada region.

The third case study consisted of coupling the orographic precipitation model to a 1D surface energy model to satisfy surface mass and energy balance conditions. The surface energy model simulated runoff, the spatial distributions of soil moisture and snow cover, and the recycling of moisture between the atmosphere and the land-surface through latent heat exchange. The precipitation model was operated for the Northern and Central Sierra Nevada Mountains at 40 km horizontal resolution, while the numerical coupling between the two models was implemented on a 2D land surface finite-element mesh with a 10 km spacing. The coupling variables, latent heat fluxes and precipitation rates, were projected between the two models during extended runs. This case study was carried out for two water-years (1986-87 and 1987-88). One major contribution of this study was the long-term simulation of the intra-annual dynamics of the hydrological cycle in a mountainous environment.

6.2 Contributions

6.2.1 - Modeling of Orographic Precipitation

The 3D atmospheric model which is based on simple descriptions of the basic physics of orographic precipitation performed well for two orographically distinct regions in the Western U.S.: an island-like obstacle in the case of the Olympic Mountains, and a barrier-like obstacle in the case of the Sierra Nevada Mountains.

The reproduction of first-order storm properties (number, interarrival times, duration, and magnitude), the spatial distribution of precipitation, and snow depth and snow cover extent were all within 20 percent error for a number of accuracy measures where the results of model simulations were compared with point observations, streamflow data, and snow course, and satellite snow cover images, respectively.

The model has three fundamental assumptions: (1) orographically forced ascent can be described as a purely adiabatic process; (2) the occurrence of orographically induced precipitation is associated predominantly with large wind field Froude numbers, i.e. wind fields that cross over a mountain's crest instead of diverging laterally; and (3) the effects of convective instability can be neglected during fall and winter precipitation at high elevations. Model results for the conditions under which these assumptions are valid displayed a substantial improvement when compared to the performance of more comprehensive weather prediction models. There was no deterioration of the model's forecasting ability with storm magnitude. This has been a problem with comprehensive limited area models (LAMs) such as the model reported by Giorgi et al. (1993).

For a 3D finite-element grid with a total number of nodes between 1500 and 2000, the average ratio between the time of computer simulation by a stand-alone Hewlett Packard HP9000-720 workstation and the corresponding real time is of the order of 1:10000. Because of this relatively high computational efficiency, the model is especially suited for long-term, high-resolution studies.

6.2.2 Multilevel Coupling of Land-Atmosphere Interactions

The use of the principles of Adaptive Multilevel Modeling to describe multiscale phenomena and to couple atmospheric and hydrological models were investigated. Two types of partial approximation were explored: partial approximation - no coupling schemes (PA-NC), and partial approximation - partial coupling schemes (PA-PC).

PA-NC schemes are disaggregation schemes aimed at the generation of compounded solutions at the large and regional scales where independent solutions from distinct models are added linearly. PA-PC schemes function either as aggregation or disaggregation tools, and can be applied to solve the same problem at different resolution levels and to use coupled models to solve mutually dependent problems where feedbacks are non-negligible.

Two major benefits of multilevel implementation of the orographic precipitation model were demonstrated. First, the computational costs of the multilevel solution (MS) were 40 percent lower than those of the standard solution (SS) at the finest resolution level, while the respective accuracy losses were below 20 percent in most cases, when modeled and measured precipitation were compared. Second, large accuracy gains, typically above fifty percent, were obtained when the MS solution was compared with the SS at the coarse resolution level, while computational costs were only 3 percent higher.

The ability to carry out coupled simulations of the intra-annual dynamics of the hydrological cycle at high elevations was tested by tracking the monthly evolution of two spatially variable hydrological quantities, runoff and snow cover extent. Land-atmosphere interactions, and particularly the exchange of latent heat between the land surface and the surface boundary layer, were investigated by coupling the orographic precipitation model to a land surface energy balance model. Previous modeling efforts have not explored these links. In the present work, we found that at high elevation the effects of the moisture exchange feedback upon the characteristics of orographic precipitation were not significant.

6.3 Recommendations for Future Work

There are many research topics related to the present work that warrant future exploration. The flavor of these is indicated next in four research areas.

6.3.1 Discretization

Orography was represented by information sampled from a digital elevation map (DEM). This method lacks the ability to preserve local orographic gradients, and consistency with respect to the amount and quality of the information retained when a DEM is sampled at multiple grid-spacing lengths. Correct local orographic gradients are needed for calibration. Consistency is fundamental to assure monotonic trends in the relationship between grid resolution and model performance. The discretization of orography for hydrological and meteorological modeling requires the preservation of 3D spatial structure within a fixed Eulerian grid. Refined techniques that use compression-decompression schemes could be used to map orographic information to the positions of finite-element grid nodes so gradients can be determined correctly (Perrier 1989).

6.3.2 Calibration

In this dissertation, calibration was aimed at the estimation of values of the precipitation efficiency parameter, K, leading to solutions which satisfied everywhere in the study domain pre-established comparison criteria against rainfall and streamflow data. The pitfall with such an approach to calibration is the lack of a systematic, and therefore consistent, methodology to carry out optimal parameter search for distinct applications. In this context, a parameter search scheme must be devised with the flexibility to accomodate solution requirements that may change from case-study to case-study according to geography, climate properties, and data availability.

Besides its dependence on local topographic gradients, the precipitation efficiency parameter was established to regulate precipitation events in the absence of convective instability. Because convective instability is often associated with large storms, and the precipitation from these storms influence the statistics of long-term simulations, it is important to study the dependence of K on the magnitude of the Brunt-Väisälä frequency for flows with low Froude number. This should provide increased capability for simulating the properties of individual storms rather than accumulated precipitation for several storms.

6.3.3 Further Validation of Adaptive Multilevel Methodologies

We have investigated the exchange of moisture between the atmosphere and the land-surface by concentrating on the non-linear interactions among variables such as precipitation, atmospheric water content, latent heat fluxes and soil moisture. Our verification and validation has been done using end-products of the hydrological cycle (e.g. runoff, snow cover extent). Further investigation of the propagation of anomalies of atmospheric water contents across the multilevel space, and the persistence of this propagation in time and space domains is needed to test the physical consistency of the internal dynamics of AMMs. This kind of study is consistent with the scientific goals of the proposed Coupled Multiscale Experiment (CME), especially with regard to the dynamics of the surface boundary layer and the estimation of soil moisture distributions compatible with complex mesoscale geomorphological scenarios (Koch 1993).

6.3.4 Applications

Mountainous zones influence regional climatology by affecting the characteristics of large-scale atmospheric circulation patterns, the spatial distribution of precipitation, and the variability of momentum, and latent and sensible heat exchanges between the land-surface and the atmosphere across the surface boundary layer. In continental regions where hydrology is influenced by mountains, the long-term management of water and ecological resources in response to climate change and anthropogenic activities requires understanding of the multiscale coupling of atmospheric, hydrological (surface and subsurface) and ecological processes. In this context, AMMs constitute a modeling option that should be explored because they allow for computationally inexpensive coupling of distinct models operating at distinct scales, and for long periods of time.

REFERENCES

Alpert, P., 1986: Mesoscale Indexing of the Distribution of Orographic Precipitation over High Mountains. *Journal of Climate and Applied Meteorology,* **25**, 532-545.

Alpert, P. and Shafir, H., 1989: A Physical Model to Complement Rainfall Normals over Complex Terrains. *Journal of Hydrology,* **110**, 51-62.

Anderson, B.R., 1975: *Weather in the West: From the Midcontinent to the Pacific.* American West Publishing Company (Pub.), 223pp.

Angström, A., 1935: Teleconnections of Climate Changes in Present Time. *Geografiska Annaler*, **17**, 242-58.

Anthes, R.A., Kuo, Y.-H., Hsie, E.-Y., Low-Nam, S., and Bettge, T.W., 1989: Estimation of Skill and Uncertainty in Regional Numerical Models. *Quarterly Journal of the Royal Meteorological Society,* **115**, 763-806.

Arya, S.P., 1988: *Introduction to Micrometeorology.* Academic Press (Pub.), 307pp.

Astling, E.G., 1984: On the Relationship Between Diurnal Mesoscale Circulations and Precipitation in a Mountain Valley. *Journal of Climate and Applied Meteorology,* **23**, 1635-1644.

Avissar, R. and Verstraete, M.M., 1990: The Representation of Continental Surface Processes in Atmospheric Models. *Reviews of Geophysics,* 35-52.

Avissar, R. and Pielke, R., 1989: A Parameterization of Heterogeneous Land Surface for Atmospheric Numerical Models and its Impact on Regional Meteorology. *Monthly Weather Review*, **117**, 2113-2136.

Bader, M.J. and Roach, W.T., 1977: Orographic Rainfall in Warm Sectors of Depressions. *Quarterly Journal of the Royal Meteorological Society*, **103**, 269-280.

Baker, M.B. and Charlson, R.J., 1990: Bistability of CCN Concentrations and Thermodynamics in the Cloud Topped Boundary Layer. *Nature*, **345**, 142-144.

Bagchi, A.K., 1982: Orographic Variation of Precipitation in a High-Rise Himalayan Basin", Hydrological Aspects of Alpine and High Mountain Areas. *IAHS Publication*, **138**, 3-9.

Banta, R.M., 1990: The Role of Mountain Flows in Making Clouds. *Meteorological Monographs*, **23**, 229-283.

Baptista, A.M., Adams, E.E., Stolzenbach, K.D., 1984: Eulerian-Lagrangian Analysis of Pollutant Transport in Shallow Waters. *R.M. Parsons Laboratory Report*, MIT (Pub.), **296**.

Barros, A.P., and Lettenmaier, D.P., 1993a: Dynamic Modeling of the Spatial Distribution of Precipitation in Remote Mountainous Areas. *Monthly Weather Review*, **121**, 1195-1214.

Barros, A.P., and Lettenmaier, D.P., 1993b: Multiscale Aggregation and Disaggregation of Precipitation for Regional Hydroclimatological Studies. *IAHS Publication*, **214**, 183-193.

Barros, A.P. and Lettenmaier, D.P., 1993c: The Role of Land-Atmosphere Interactions in the Regional Hydrology of Mountainous Regions. *Preprints of the Conference on Hydroclimatology*, AMS, Januray 17-22.

Barros, A.P. and Lettenmaier, D.P., 1993d: Dynamic Modeling of Orographically-Induced Precipitation. *Reviews of Geophysics*, in revision.

Barros, A.P. and Lettenmaier, D.P., 1993e: Incorporation of an Evaporative Cooling Scheme into a Dynamic Model of Orographic Precipitation. *Monthly Weather Review*, in review.

Barry, R.G., 1981: *Mountain Weather and Climate*. Methuen (Pub.), 313pp.

Bell, R.S., 1978: The Forecasting of Orographically Enhanced Rainfall Accumulations Using 10-Level Model Data. *Meteorological Magazine*, **107**, 113-124.

Bergeron, T., 1960a: Problems and Methods of Rainfall Investigation: Physics of Precipitation. *Geophysical Monographs*, **5**, 5-30.

Bergeron, T., 1960b: Operation and Results of 'Project Pluvius'. *Geophysical Monographs*, **5**, 152-157.

Beven, K.J., 1989: Changing Ideas in Hydrology - The Case of Physically-Based Models. *Journal of Hydrology*, **105**, 157-172.

Bonacina, L.C.W., 1945: Orographic Rainfall and its Place in the Hydrology of the Globe. *Quarterly Journal of the Royal Meteorological Society*, **71**, 41-55.

Bosch, J.M., and Hewlett, J.D., 1982: A Review of Catchment Experiments to Determine the Effect of Vegetation Changes on Water Yield and Evapotranspiration. *Journal of Hydrology*, **55**, 3-23.

Brandt, A., 1977: Multi-Level Adaptive Solutions to Boundary-Value Problems. *Mathematics of Computation*, **31**, 333-390.

Brandt, A., 1988: Multilevel Computations: Review and Recent Developments. *Multigrid Methods: Theory, Applications and Supercomputing*, S.F. McCormick (Ed.), 35-62.

Broccoli, A.J. and Manabe, S., 1992: The Effects of Orography on Midlatitude Northern Hemisphere Dry Climates. *Journal of Climate*, **5**, 1181-1201.

Browning, K.A., 1980: Structure, Mechanism and Prediction of Orographically-Enhanced Rain in Britain. *Orographic Effects in Planetary Flows*. GARP (Pub.), **23**, 88-108.

Browning, K.A., 1989: The Data Base and Physical Basis of Mesoscale Forecasting. *Forecasting and Its Applications*, WMO (Pub.), **712**, 1-20.

Browning, K.A., and Collier, C.G., 1989: Nowcasting of Precipitation Systems. *Reviews of Geophysics*, **27**, 345-370 (1989).

Burges, S.J, 1986: Trends and Directions in Hydrology. *Water Resources Research*, **22**, 1S-5S.

Burrows, D.A., 1992: Evaluation of a Two-Dimensional Kinematic Cloud Model Using Data from a Central Sierra Nevada Orographic Cloud System. *Journal of Applied Meteorology*, **31**, 51-63.

Cayan, D.R. and Peterson, D.H., 1989: The Influence of North Pacific Atmospheric Circulation on Streamflow in the West. *Geophysical Monographs*, **55**, 375-397.

Cayan, D.R. and Roads, J.O., 1984: Local Relationships Between United States West Coast Precipitation and Monthly Mean Circulation Parameters. *Monthly Weather Review*, **112**, 1276-1282.

Caramori, P., Schuepp, P., Desjardins, R. and MacPherson, I., 1993: Structural Analysis of Airborne Flux Estimates. *Journal of Climate*, in press.

Carruthers, D.J. and Choularton, T.W., 1983: A Model of the Feeder-seeder mechanism of orographic Rain Including Stratification and wind-drift Effects. *Quarterly Journal of the Royal Meteorological Society*, **109**, 575-588.

Carruthers, D.J. and Choularton, T.W., 1986: The Microstructure of Hill Cap Clouds. *Quarterly Journal of the Royal Meteorological Society*, **112**, 113-129.

Charney, J.G., 1975: Dynamics of Deserts and Droughts in the Sahel. *Quarterly Journal of the Royal Meteorological Society*, **101**, 193-202.

Choularton, T.W. and Perry, S.J., 1986: A Model of the Orographic Enhancement of Snowfall by the Seeder-Feeder Mechanism. *Quarterly Journal of The Royal Meteorological Society*, 335-345.

Collier, C.G., 1975: A Representation of the Effects of Topography on Surface Rainfall within Moving Baroclinic Disturbances. *Quarterly Journal of The Royal Meteorological Society*, **101**, 407-422.

Collier, C.G., 1977: The Effect of Model Grid Length and Orographic Rainfall Efficiency on Computed Surface Rainfall. *Quarterly Journal of the Royal Meteorological Society*, **103**, 247-253.

Colton, D.E., 1976: Numerical Simulation of the Orographically Induced Precipitation Distribution for Use in Hydrologic Analysis. *Journal of Applied Meteorology*, **15**, 1241-1251.

Cotton, W.R. and Anthes, R.A., 1989: *Storm and Cloud Dynamics*. Academic Press (Pub.), 883pp.

Cotton, W.R., Tripoli, G.J., Rauber, R.M., and Mulvihill, E.A., 1986: Numerical Simulation of the Effects of varying Ice Crystal Nucleation Rates and Aggregation Processes on Orographic Snowfall. *Journal of Climate and Applied Meteorology*, **25**, 1658-1680.

Corradini, C. and Melone, F., 1989: Spatial Structure of Rainfall in Mid-latitude Cold Front Systems. *Journal of Hydrology*, **105**, 297-316.

Crochiere R. and Rabiner L., 1987: Multirate Processing of Digital Signals. *Advanced Topics in Signal Processing*, J.S. Lim and A.V. Oppenheim (Eds.), 123-198.

Cunnington, W.M. and Mitchell, J.F.B., 1990: On the Dependence of Climate Sensitivity on Convective Parameterization. *Climate Dynamics*, **47**, 85-93.

Deardorff, J.W., 1978: Efficient Prediction of Ground Surface Temperature and Moisture, with Inclusion of a Layer of Vegetation. *Journal of Geophysical Research*, **83**, 1889-1903.

Delworth, T. and Manabe, S., 1989: The Influence of Soil Wetness on Near-Surface Atmospheric Variability. *Journal of Climate*, 1447-1462.

Dickinson, R., and Kennedy, P.J., 1991: Land Surface Hydrology in a General Circulation Model - Global and Regional Fields Needed for Validation. *Surveys in Geophysics*, **12**, 115-126.

Dickinson, R., Henderson-Sellers, A., Kennedy, P., and Wilson, M., 1986: Biosphere-Atmosphere Transfer Scheme (BATS) for the NCAR Community Climate Model. *NCAR Technical Note/TN-275+STR.*

Dooge, J.C., 1986: Looking for Hydrologic Laws. *Water Resources Research*, 46S-58S.

Douglas, C.C., and Miranker, W.J., 1988: Some Nontelescoping Parallel Algorithms Based on Serial Multigrid Aggregation/Disaggregation Techniques. *Multigrid Methods: Theory, Applications and Supercomputing*, S.F. McCormick (Ed.), 101-115.

Dunn, L.B., 1991: Evaluation of Vertical Motion: Past, Present, and Future. *Weather and Forecasting*, **6**, 65-75.

Durran, D.R., and Klemp, J.B., 1983: A Compressible Model for the Simulation of Moist Mountain Waves. *Monthly Weather Review*, **111**, 2341-2361.

Eagleson, P.S., 1986: The Emergence of Global-Scale Hydrology. *Water Resources Research*, 6S-14S.

Eagleson, P.S., 1991: Hydrologic Science: a Distinct Geoscience. *Reviews of Geophysics*, **29**, 237-248.

Ebbsmeyer, C.C., Coomes, C.A., Cannon, G.A., Bretschneider, D.E., 1989: Linkage of Ocean and Fjord Dynamics at Decadal Period. *Geophysical Monographs*, **55**, 399-418.

Elliott, R.D., 1977: *Final Report on Methods for Estimating Areal Precipitation in Mountainous Areas,* NOAA-NWS Report NO. 77-13, 144pp.

Elsner, J.B., and Tsonis, A.A., 1992: Nonlinear Prediction, Chaos and Noise. *Bulletin of The American Meteorological Society*, **73**, 49-60.

Entekhabi, D. and Eagleson, P.S., 1989: Land-Surface Hydrology Parameterization for Atmospheric General Circulation Models Including Subgrid Scale Spatial Variability. *Journal of Climate*, **2**, 816-831.

Flandrain, P., 1989: *Some Aspects of Non-Stationary Signal Processing with Emphasis on Time-Frequency and Time-Scale Methods.* Combes, J.M. and Grossman, A. (Eds.), 68-91.

Folland, C.K., and Owen, J.A., 1988: GCM Simulation and Prediction of Sahel Rainfall Using Global and Regional Sea Surface Temperatures. *WMO Publication*, **254**, 102-114.

Fortescue, J.A.C., 1980: *Environmental Geochemistry: A Holistic Approach*, Springer-Verlag (Pub.), 347pp.

Fraser, A.B, Easter, R.C. and Hobbs, P.V., 1973: A Theoretical Study of the Flow of Air and Fallout of Solid Precipitation Over Mountainous Terrain: Part I. Airflow Model. *Journal of The Atmospheric Sciences*, **30**, 801-812.

Giorgi, F., Bates, G.T. and Nieman, S.J., 1993: The Multiyear Surface Climatology of a Regional Atmospheric Model over the Western United States. *Journal of Climate*, **6**, 75-95.

Giorgi, F. and Mearns, L.O., 1991: Approaches to the Simulation of Regional Climate Change: a Review. *Reviews of Geophysics*, 191-217.

Giorgi, F. and Bates, G.T., 1989: The Climatological Skill of a Regional Model over Complex Terrain. *Monthly Weather Review*, **117**, 2325-2347.

Glantz, M.H., 1991: Introduction. *Teleconnections Linking Worldwide Climate Anomalies*, Glantz, M.H., Katz, R.W., and Nicholls, N. (Eds.), Cambridge University Press (Pub.), 2-12.

Gleick, J., 1988: *Chaos: Making a New Science*, Pergamon Books (Pub.), 352pp.

Glimm, J., 1991: Nonlinear and Stochastic Phenomena: the Grand Challenge for Partial Differential Equations. *SIAM Review*, **33**, 626-643.

Gocho, Y., 1978: Numerical experiment of Orographic Heavy Rainfall Due to a Stratiform Cloud. *Journal of the Meteorological Society of Japan*, **56**, 405-422.

Gollvick, S., 1984: Estimation of Orographic Precipitation by Dynamical Interpretation of Synoptic Model Data. *Swedish Meteorological and Hydrological Institute*, **142**, 20pp.

Gollvik, S. and Omstedt, G., 1988: An Air-Mass-Transformation Model for Short Range Weather Forecasting, a Bulk-Model Approach. *Swedish Meteorological and Hydrological Institute*, **8**, 30pp.

Grotch, S.L., 1988: Regional Intercomparisons of General Circulation Model Predictions and Historical Climate Data. *DOE/NBB-0084*.

Hendrick, R.L., DeAngelis, R.J. and Dingman, S.L., 1978: The Role of Elevation in Determining Spatial Distributions of Precipitation, snow, and Water Input at Mt. Mansfield, Vermont. *Modeling of Snow Cover Runoff*, Colbeck, S.C. and Ray M. (Eds.), 63-70.

Hobbs, P.V., Easter,E.C. and Fraser, A.B., 1973: A Theoretical Study of the Flow of Air and Fallout of Solid Precipitation Over Mountainous Terrain: Part II. Microphysics. *Journal of The Atmospheric Sciences*, **30**, 813-823.

Holton, J.R., 1979: *An Introduction to Dynamic Meteorology.* Academic Press (Pub.), 391pp.

Horel, J.D. and Wallace, J.M., 1981: Planetary-Scale Atmospheric Phenomena Associated with the Southern Oscillation. *Monthly Weather Review*, **109**, 813-829.

Hsu, C.P., and Wallace, J.M., 1976: The Global Distribution of the Annual and semi-Annual Cycles in Precipitation. *Monthly Weather Review*, **104**, 1093-1101.

Jarraud, M., Simmons, A.J. and Kanamitsu, M., 1987: The Concept, Implementation and Impact of an Envelope Orography. *Seminar/Workshop 1986 on Observation, Theory and Modeling of Orographic Effects*, ECMWF (Pub.), **2**, 81-127.

Kalinin, G.P., 1971: *Global Hydrology.* Keter Press (Pub.).

Kasahara, A., 1980: Influence of Orography on the Atmospheric General Circulation. *Orographic Effects in Planetary Flows*, GARP (Pub.), **23**, 3-49.

Kevorkian, J., 1990: *Partial Differential Equations Analytical Solution Techniques*. Wadsworth and Brooks-Cole (Pub.), 206-260.

Klein, W.H. and Bloom, H.J., 1987: Specification of Monthly Precipitation over the United States from the Surrounding 700 mb Height Field. *Monthly Weather Review*, **115**, 2118-2132.

Klemes, V., 1990: The Modeling of Mountain Hydrology: The Ultimate Challenge. *IAHS Publication*, **190**, 29-43.

Koch, S.E. (Ed.), 1993: Report of the Proceedings of the Colloquium and Workshop on Multiscale Coupled Modeling. *NASA Conference Publication*, **3217**. 112pp.

Lau, K.M., and Sheu, P.J., 1991: Teleconnections in Global Rainfall Anomalies, Seasonal to Interdecadal Time Scales. *Teleconnections Linking Worldwide Climate Anomalies*, Glantz, M.H., Katz, R.W., and Nicholls, N. (Eds.), Cambridge University Press (Pub.), 227-256.

Lau, K.M., and Sheu, P.J., 1988: Annual Cycle, Quasi-Biennial Oscillation and Southern Oscillation in Global Precipitation. *Journal of Geophysical Research*, **93**, 10975-10988.

Lettau, H., Lettau, K., and Molion, L.C.B., 1979: Amazonia Hydrologic Cycle and the Role of Atmosphere Recycling in Assessing Deforestation Effects. *Monthly Weather Review*, **107**, 227-238.

Lin, Y.-L., 1986: A Study of the Transient Dynamics of Orographic Rain. *Papers in Meteorological Research*, **9**, 20-44.

Linsley, R.K., Kohler, M.A., and Paulhus, J.L.H., 1982: *Hydrology for Engineers*. McGraw-Hill (Pub.), 508pp.

Lovelock, J.E., 1986: Geophysiology: A New Look at Earth Science. *The Geophysiology of Amazonia*, R.E. Dickinson (Ed.), John Wiley & Sons (Pub.), 11-23.

Mahouf, J.-F., Richard E., and Mascart, P., 1987: The Influence of Soil and Vegetation on the Development of Mesoscale Circulations. *Journal of Climate and Applied Meteorology*, **26**, 1483-1495.

Manabe, S., and Terpstra, T.B., 1974: The Effects of Mountains on the General Circulation of the Atmosphere as Identified by Numerical Experiments. *Journal of the Atmospheric Sciences*, **31**, 3-42.

Mass, C., 1981: Topographically Forced Convergence in Western Washington State. *Monthly Weather Review*, **109**, 1335-1347.

Matveev, L.T., 1984: *Cloud Dynamics*. D. Reidel (Pub.), 340 pp.

McCormick, S.F., and Thomas, J., 1986: The Fast Adaptive Composite Grid (FAC) Method for Elliptic Equations. *Mathematics of Computation*, **46**, 439-456.

McCormick, S.F., 1989: Multilevel Adaptive Methods for Partial Differential Equations. *Frontiers in Applied Mathematics*, SIAM (Pub.), **6**.

McCormick, S.F., 1992: Multilevel Projection Methods for Partial Differential Equations. *CBMS-NSF Regional Conference Series in Applied Mathematics*, SIAM (Pub.), **62**.

Mesinger, F. and Janjie, Z.I., 1985: Problems and Numerical methods of the Incorporation of Mountains in Atmospheric Models. *Lectures in Applied Mathematics*, **22**, 81-120.

Meyers, M.P. and Cotton, W.R., 1992: Evaluation of the Potential for Wintertime Quantitative Precipitation Forecasting over Mountainous Terrain with an Explicit Cloud Model. Part I: Two-Dimensional Sensitivity Experiments. *Journal of Applied Meteorology*, **31**, 26-50.

Miller, J.F., Frederick, R.H., and Tracey, A.B., 1973: *Precipitation-Frequency Atlas of the Western United States.* NOAA Atlas, **2**, 43pp .

Morse, P.M., and Feshbach, H., 1953: *Methods of Theoretical Physics.* McGraw-Hill Book Company (Pub.), 692-708.

Murray, R., 1952: Rain and Snow in Relation to the 1000-700 mb and 1000-500 mb Thicknesses and the Freezing Level. *The Meteorological Magazine*, **81**, 5-8.

Murtagh, F. and Heck, A., 1987: *Multivariate Data Analysis.* D. Reidel (Pub.), 210pp.

Namias, J. 1960: Synoptic and Planetary Scale Phenomena Leading to the Formation and Recurrence of Precipitation. *Geophysical Monographs*, **5**, 32-44.

Namias, J., 1980: The Art and Science of Long-Range Forecasting. *EOS*, **61**, 449-450.

Nickerson, E.C., Richard, E., Rosset, R. and Smith, D.R., 1985: The Numerical Simulation of Clouds, Rain, and Airflow over the Vosges and Black Forest Mountains: a Meso-(beta) Model with Parameterized Microphysics. *Monthly Weather Review*, **114**, 398-414.

Oke, T.R., 1978: *Boundary Layer Climates.* Halsted Press (Pub.), 135-159.

Oki, T. and Koike, T., 1989: Spatial Rainfall Distribution Estimation at a Storm Event in Mountainous Regions Estimated by Orography and Wind Direction. *Water Resources Research*, **27**, 359-369.

O'Laughlin, E.M., 1990: Perspectives on Hillslope Research. *Process Studies in Hillslope Hydrology*, M.G. Anderson and T.P. Burt (Eds.), John Wiley & Sons (Pub.), 501-516.

Ookouchi, Y., Segal, M., Kessler, R.C., and Pielke, R.A., 1984: Evaluation of Soil Moisture Effects on the Generation and Modification of Mesoscale Circulations. *Monthly Weather Review*, 2281-2291.

Paegal, J., Pielke, R.A., Dalu, G.A., Miller, W., Garratt, J.R., Vukicevic, T., Berri, G. and Nicolini, M., 1990: Predictibility of Flows over Complex Terrains. *Meteorological Monographs*, **23**, 285-301.

Panton, R.L., 1984: *Incompressible Flow.* John Wiley &Sons (Pub.), 780pp.

Parsons, D.B. and Hobbs, P.V., 1983: The Mesoscale and microscale Structure and organization of Clouds and Precipitation in Midlatitude Cyclones. IX: Some Effects of Orography on Rainbands. *Journal of the Atmospheric Sciences*, **40**, 1930-1949.

Puvaneswaran, K.Y., and Smithson, P.A., 1991: Precipitation-Elevation Relationships over Sir Lanka. *Theoretical and Applied Climatology*, **43**, 113-122.

Peck, E.L. and Schaake, J.C., 1990: Network Design for Water Supply Forecasting in the West. *Water Resources Bulletin*, **26**, 87-99.

Perrier, V., 1989: Towards a Method for Solving Partial Differential Equations Using Wavelet Basis. *Wavelets Time-Frequency Methods and Phase Space.* Combes, J.M. and Grossman, A. (Eds.), 269-283.

Pielke, R.A., 1984: *Mesoscale Meteorological Modeling.* Academic Press (Pub.), 612pp.

Pielke, R.A., Dalu, G.A., Snook, J.S., Lee, T.J., and Kittel, T.G.F., Nonlinear Influence of Mesoscale Land Use on Weather and Climate. *Journal of Climate*, 1053-1069, 1991.

PierreHumbert, R.T., 1984: Linear Results on the Barrier Effects of mesoscale Mountains. *Journal of the Atmospheric Sciences*, **41**, 1356-1367.

Rauber, R.M., 1992: Microphysical Structure and Evolution of a Central Sierra Nevada Orographic Cloud System. *Journal of Applied Meteorology,* **31**, 3-24.

Rhea, J.O., 1978: Orographic Precipitation Model for Hydrometeorological Use. *Colorado State University Atmospheric Paper,* **287**, 198pp.

Richard, E., Chaumerliac, N. and Mahfouf, J.F., 1987: Numerical Simulation of Orographic Enhancement of Rain with a Mesoscale Model. *Journal of Climate and Applied Meteorology,* **26**, 661-669.

Roache, P. J., 1972: On Artificial Viscosity. *Computational Fluid Dynamics*, Hermosa (Pub.), 351-374.

Roads, J.O., and Maisel, T.N., 1991: Evaluation of the National Meteorological Center's Medium Range Forecast Model Precipitation Forecasts. *Weather and Forecasting*, **6**, 123-130.

Robichaud, A.J. and Austin, G.L., 1988: On the Modeling of Warm Orographic Rain by the Seeder-Feeder Mechanism. *Quarterly Journal of the Meteorological Society,* **114**, 967-988.

Rogers, R.R., and Yau, M.K., 1988: *A Short Course in Cloud Physics*. Pergamon Press (Pub.), 12-27.

Rotunno, R., 1983: On the Linear Theory of the Land and Seabreeze. *Journal of the Atmospheric Sciences*, **40**, 1999-2009.

Rutledge, S.A., and Hobbs, P.V., 1983: The Mesoscale and Microscale Structure and Organization of Clouds and Precipitation in Midlatitude Cyclones. VIII: A Model for the "Seeder-Feeder" process in Warm-Frontal Rainbands. *Journal of the Atmospheric Sciences*, **40**, 1185-1206.

Salati, E., and Vose, P.B., 1984: Amazon Basin: A System In Equilibrium. *Science*, **225**, 129-138.

Sarker, R.P., 1966: A dynamical Model of orographic Rainfall. *Monthly Weather Review*, **94**, 555-572.

Sarker, R.P., 1967: Some Modifications in a Dynamic Model of Orographic Rainfall. *Monthly Weather Review*, **95**, 673-684.

Sassen, K., Huggins, A.W., Long, A.B., snider, J.B., and Meitin, R.J., 1990: Investigations of a Winter Mountain Storm in Utah. Part II: Mesoscale Structure, Supercooled Liquid Water Development, and Precipitation Processes. *Journal of the Atmospheric Sciences*, **47**, 1323-1350.

Sellers, P. J., 1991: Modeling and observing Land-Surface-Atmosphere Interactions on Large Scales. *Surveys in Geophysics*, **12**, 85-114.

Sellers, P.J., and Lockwood, J.G., 1981: A Numerical Simulation of the Effects of Changing Vegetation Type on Surface Hydroclimatology. *Climate Change*, **3**, 121-136.

Shukla, J. and Mintz, Y., 1982: Influence of Land-Surface Evapotranspiration on the Earth's Climate. *Science*, **215**, 1498-1501.

Shuttleworth, W.J., 1991a: Insight from Large-Scale Observational Studies of Land/Atmosphere Interactions. *Surveys in Geophysics*, **12**, 3-30.

Shuttleworth, W.J., 1991b: The Role of Hydrology in Global Science. *IAHS Publication*, **204**, 361-375.

Smith, R.B., 1979: The Influence of Mountains on the Atmosphere. *Advances in Geophysics*, **21**, 87-233.

Smith, R.B., 1982: A Differential Advection Model of Orographic Rain. *Monthly Weather Review*, **110**, 306-310.

Smith, R.B., 1987: The Role of Moist Processes in Mountain Effects. *Seminar/Workshop 1986 on Observation, Theory and Modelling of orographic Effects*, ECMWF (Pub.), 1, 77-111.

Smolarkiewicz, P.K., and Rotunno, R., 1989: Low Froude Number Past Three Dimensional Obstacles. Part I: Baroclinicity Generated Lee Vortices. *Journal of the Atmospheric Sciences*, **46**, 1154-1164.

Smolarkiewicz, P.K., and Rotunno, R., 1990: Low Froude Number Past Three Dimensional Obstacles. Part II: Upwind Flow Reversal Zone. *Journal of the Atmospheric Sciences*, **47**, 1498-1511.

Smolarkiewicz, P.K., and Rasch, P.J., 1991: Monotone Advection on the Sphere: an Eulerian versus Semi-Lagrangian Approach. *Journal of the Atmospheric Sciences*, **48**, 793-810.

Sommerfeld, A., 1949: *Partial Differential Equations in Physics*. Ernst G. Strauss (Transl.), Academic Press (Pub.), 36-43.

Speers, P., 1986: *Precipitation Analysis and Modeling in Western Washington*. MSc. Thesis, Department of Atmospheric Sciences, University of Washington, Seattle, 163pp.

Speranza, A., 1987: Theory of Lee Cyclogenesis. *Seminar/Workshop 1986 on Observation, Theory and Modelling of Orographic Effects*, ECMWF (Pub.), **2**, 253-273.

Storebo, P.B., 1975: Small Scale Topographical Influences on Precipitation. *Tellus*, **28**, 45-59.

Sumner, G., 1988: *Precipitation Process and Analysis*. John Wiley & Sons (Pub.), 455pp.

Takeya, K., Nakatsugawa, M., Yamada, T., 1989: Investigation of Rainfall by Field Observations and a Physically Based Model. *Pacific Seminar on Water Resources Systems*, 385-403.

Thiebaux, H.J. and Pedder, A.M., 1987: *Spatial Objective Analysis with Applications in Atmospheric Science*. Academic Press (Pub.), 299pp.

Thomas, G. and Henderson-Sellers, A., 1991: An Evaluation of Proposed Representations of Subgrid Hydrologic Processes in Climate Models. *Journal of Climate*, **4**, 898-910.

Tripoli, G.J. and Cotton, W.R., 1989: Numerical Study of an Observed orogenic Convective System. Part I: Simulated Genesis and Comparison with Observations. *Monthly Weather Review*, **117**, 273-304.

U.S. Weather Bureau, 1967: Storm Data and Unusual Weather Phenomena. *Storm Data*, **9**, 1-3.

Wallace, J.M. and Hobbs, P.V., 1977: *Atmospheric Science: An Introductory Survey*. Academic Press (Pub.), 467pp.

Wallace, J.M., 1987: Observations of Orographic Influences upon Large-Scale Atmospheric Motions. *Seminar/Workshop 1986 on Observation, Theory and Modelling of Orographic Effects*, ECMWF (Pub.), **1**, 23-49.

Walsh, J.E., Richman, M.B., and Allen, D.W., 1982: Spatial Coherence of Monthly Precipitation in the United States. *Monthly Weather Review*, **110**, 272-286.

Weare, B.C., and Hoeshele, M.A., 1983: Specification of Monthly Precipitation in the Western United States from Monthly Mean Circulation. *Journal of Climate and Applied Meteorology*, **22**, 1000-1007.

Wood, E.F., 1991: Global Scale Hydrology: Advances in Land Surface Modeling. *Reviews of Geophysics*, 193-201.

WCRP, 1992: *Scientific Plan for the GEWEX Continental-Scale International Project.* WMO (Pub.), WCRP-67 WMO/TD-No. 461, 65 pp.

Xue, Y., Liou, K.-N., and Kasahara, A., 1990: Investigation of Biogeophysical Feedback on the African Climate Using a Two-Dimensional Model. *Journal of Climate*, **3**, 337-352.

APPENDIX A - 1D EXAMPLE OF MULTIGRID GENERATION

Consider the discretization of the 1D space S $(0 < x < L)$ at resolution h

```
|-----> x
*-------h------*
*--------------- *--------------- *---------------*--------------- *-----------------*      S_h
1                2                3               4                5                 6
```

The refinement of the three inner segments defined by $x \in [x_2\ ,\ x_5]$ at a resolution ratio $\alpha=0.5$ yields the subspace $S^1_{\alpha h}$

```
                 *-------*-------*-------*-------*-------*-------*                   S_αh
                 2       7       3       8       4       9       5
```

and

$S_h^C = S_h \sqcup S_{\alpha h}$ is defined by

```
*----------------*-------*-------*-------*-------*-------*-------*----------------*      S_h^C
1                2       7       3       8       4       9       5                6
```

This process can be repeated for an unlimited number of successive refinements. Conformity between adjacent grid levels is determined by constraining the limits of $S^1_{\alpha h}$ to match discretized elements in S_h. The continuity of a variable U through the solution space implies that at $x=x_2$ and $x=x_5$ in S_h^C the solutions $U_{\alpha h}$ and U_h are equal, and therefore the consistency of the global solution is preserved.

APPENDIX B - 1D EXAMPLE OF THE REPRESENTATION OF A PDE IN A DISCRETE SPACE S_h

Let c(x) be a state variable described by

$$\gamma \frac{\partial c}{\partial x} + \theta \frac{\partial^2 c}{\partial x^2} = F \tag{B.1}$$

where

$$0 \leq x \leq L$$

and γ and θ are constants.

Designating by $\tilde{c}(x)$ the numerical solution approximation to c(x), then the error of the approximation can be estimated through the residual R(x), where

$$R(x) = \gamma \frac{\partial \tilde{c}}{\partial x} + \theta \frac{\partial^2 \tilde{c}}{\partial x^2} - F \tag{B.2}$$

The method of weighted residuals provides a framework to minimize R in the global sense within a domain of application Ω by forcing

$$\int_\Omega W\, R\, d\Omega = \int_o^L W\, R\, dx = 0 \tag{B.3}$$

where W(x) is a weighting function, which redistributes the residual.
Substituting eq. (B.2) in eq.(B.3),

$$\int_\Omega \gamma\, W \frac{\partial \tilde{c}}{\partial x}\, d\Omega + \int_\Omega \theta\, W \frac{\partial^2 \tilde{c}}{\partial x^2}\, d\Omega - \int_\Omega W\, F\, d\Omega = 0 \tag{B.4}$$

Integrating by parts the second term of eq.(B.4) yields

$$\int_\Omega \gamma\, W \frac{\partial \tilde{c}}{\partial x}\, d\Omega + \left[\theta\, W \frac{\partial \tilde{c}}{\partial x} \right]_\Gamma - \int_\Omega \theta \frac{\partial W}{\partial x} \frac{\partial \tilde{c}}{\partial x}\, d\Omega = \int_\Omega W\, F\, d\Omega \tag{B.5}$$

with Γ designating the boundary of domain Ω. For simplicity let us assume that the Newman type boundary conditions associated with the second term of eq.(B.5) are described by

$$\frac{\partial \tilde{c}}{\partial x} = 0 \mid_{x \in \Gamma} \tag{B.6}$$

After rearranging, eq.(B.5) takes the form

$$\int_\Omega L \, \tilde{c} \; d\Omega = \int_\Omega f \; d\Omega \tag{B.7}$$

which is similar to eq.(4.2) in Part 4. The operator L and the forcing f are defined as follows

$$L = (\gamma \, W - \theta \, \frac{\partial W}{\partial x}) \frac{\partial}{\partial x} \tag{B.8a}$$

$$f = W \, F \tag{B.8b}$$

To proceed further with this example we will rely on the application of the Galerkin finite-element method to the numerical solution of PDEs, because it is the method used in our models. In a finite-element context, the domain of application Ω in the space S_h is

$$\Omega = \sum_{i=1}^{n} \Omega_i \tag{B.10}$$

where n is the number of elements Ω_i of length h resulting from the discretization. For instance, in the case of S_h as presented in Appendix A, there are five finite elements of 2 nodes each, in a total of six discretization points. The main variable $\tilde{c}\,(x)$ and its derivatives can be expressed by

$$\tilde{c}\,(x) = \sum_{j=1}^{m} N_j\,(x)\,\tilde{c}_j \tag{B.11a}$$

$$\frac{\partial \tilde{c}}{\partial x} = \sum_{j=1}^{m} \frac{\partial N_j}{\partial x}\,\tilde{c}_j \tag{B.11b}$$

where m is the number of discretization points, and $\tilde{c}_j$ are the values of the numerical solution at the nodal points. The shape functions N_j are piecewise continuous functions within each finite-element, and satisfy the following conditions

$$N_j\,(x)=1.0 \quad \text{for } x=x_j \qquad (B.12)$$
$$N_j\,(x)=0.0 \quad \text{for } x=x_k \quad \text{and } k \neq j$$

In tensor notation

$$\underset{\sim}{\tilde{c}}^{T} = \{\, \tilde{c}_1 \, \tilde{c}_2 \, \ldots\ldots\ldots \, \tilde{c}_m \,\}$$

$$\underset{\sim}{N}^{T} = \{\, N_1 \, N_2 \, \ldots\ldots\ldots \, N_m \,\}$$

$$\underset{\sim}{N}_x = \{\, \frac{\partial N_1}{\partial x} \, \frac{\partial N_2}{\partial x} \, \ldots\ldots \, \frac{\partial N_m}{\partial x} \,\}$$

Finally, in the Galerkin formulation of the method of weighted residuals

$$W(x) = \sum_{j=1}^{m} N_j\,(x) \qquad (B.11)$$

and therefore

$$L = \gamma \, \underset{\sim}{N}^{T} \, \underset{\sim}{N}_x + \theta \, \underset{\sim}{N}_x{}^{T} \underset{\sim}{N}_x \qquad (B.12a)$$

$$f= \underset{\sim}{N}^{T} \, \underset{\sim}{F} \qquad (B.12b)$$

The intergrid transfer operators $I_h^{\alpha h}$ and $I_{\alpha h}^{h}$ between S_h and $S_{\alpha h}$ defined in Section 4.1 can be expressed in terms of N_j as follows

$$\tilde{c}_{\alpha h} = \sum_{j=1}^{m\alpha} N_j^h \, \tilde{c}_h \qquad (B.13a)$$

and

$$\tilde{c}_h = \sum_{j=1}^{m\alpha h} N_j^{\alpha h} \, \tilde{c}_{\alpha h} \qquad (B.13b)$$

where the superscripts h and αh refer to the definition of the number of nodes m and shape functions N_j respectively in S_h and $S_{\alpha h}$.

APPENDIX C - PROPERTIES OF INTERGRID OPERATIONS

Consider two operators L and M which are the prolongation or interpolation operator, and the restriction or coarsening operator respectively. U_h and $U_{\alpha h}$ are grid-locked variables describing the generalized variable v in grids of resolution h and αh respectively. If L and M are adjoint operators, then

$$U_{\alpha h} \; L\,(U_h) - U_h \; M(U_{\alpha h}) = Q_{\alpha h} + P_h \tag{C.1}$$

where Q and P are non-unique functions (Kevorkian 1989). The adjointness of the projection operators is a very instrumental property in the context of adaptive multigrid modeling, as it allows for linear transfer of information between adjacent levels in the multigrid network. For the case of conform intergrid projections without interaction between $U_{\alpha h}$ and U_h outside the domain defined $S_{\alpha h} \cap S_h$ (see Appendix B), the right-hand side of eq. (C.1) is determined by $Q_{\alpha h} = P_h = 0$.

From eq.(4.2) in Part 4 the projection operators can be expressed by

$$L(U_h) = I_h^{\alpha h} \, U_h \tag{C.2}$$

$$M(U_h) = I_{\alpha h}^{h} \, U_{\alpha h} \tag{C.3}$$

Substituting eqs. (C.2) and (C.3) in (C.1)

$$U_{\alpha h} \, I_h^{\alpha h} \, U_h = U_{\alpha h} \, (I_{\alpha h}^{h})^T U_h \tag{C.4}$$

and finally

$$I_h^{\alpha h} = (I_{\alpha h}^{h})^T \tag{C.5}$$